UNIVERSITÀ DELLA CALABRIA

UNIVERSITA' DELLA CALABRIA

Dipartimento di Fisica

Scuola di Dottorato

Archimede in Scienze, Comunicazione e Tecnologia

Indirizzo

Fisica e Tecnologie quantistiche

CICLO

XXVII

TITOLO TESI

"LASER ABLATION METHODS FOR CULTURAL HERITAGE: RESTORATION, CONSERVATION, CONSOLIDATION"
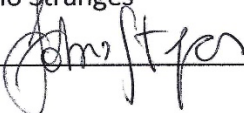
Settore Scientifico Disciplinare FIS/07

Direttore: Ch.mo Prof. Pietro S. Pantano

Firma _____

Supervisore: Ch.ma Prof.ssa Assunta Bonanno

Firma _____

Dottorando: Dott. Fabio Stranges

Firma _____

Contents

Abstract

This thesis, developed in the period between March 2012 and November 2014, focuses on the researches on new methods for cleaning, diagnostics and restoration of Cultural Heritage assets. These methods are based on the use of Laser Ablation in various media (air, water and vacuum) and on different materials, such as alloys, metals and artificial stone materials.

Furthermore, the thesis proposes different types of investigation, consolidation and restoration of archaeological artefacts, introducing new possible strategies of diagnostics and enhancements in the study of cultural heritage, through the contribution of nanotechnology and nanomaterials, still slightly used in the field of Cultural Heritage.

The main objective of the thesis is to verify the applicability of different techniques in different environments, also trying to make the employed methodologies less invasive and more effective.

In fact, a fundamental point is LA cleaning on various materials, directly in situ, using portable equipment and prototypes can be used in subaerial and underwater environments to selectively remove of crusts and deterioration patinas that often cover archaeological artifacts.

The prototype has been realized during PhD and it can be used for measurements of LA cleaning and for Raman and PL spectroscopy.

For testing the diagnostic methodology efficacy, the investigations were carried out by non-destructive methods on different types of materials (such as bronze, ceramics and precious metals) in different environments (subaerial and underwater), obtaining information comparable to laboratory measurements.

Morphological studies were carried out using optical microscopy, Scanning Electron Microscopy SEM and Atomic Force Microscopy AFM (rarely used in Cultural Heritage).

Chemical analysis were carried out with different spectroscopic techniques including X-Ray Fluorescence spectroscopy (XRF), X-ray Photoelectron Spectroscopy (XPS), PhotoLuminescence (PL), CathodoLuminescence (CL) and finally the Energy Dispersive X-ray (EDX).

Another aim concerns the study of particulate generated by LA cleaning for application in the consolidation of the artifact and high tech (photovoltaic and optoelectronic applications).

Indeed, we study the production and characterization of nanoparticles and nanocomposites based on TiO_2 and SiO_2 for application to restoration and consolidation in archaeological artifacts, for exploring the possibility to use NPs as consolidating materials without introducing chemical, physical or esthetical changes in artifacts. Finally, our study has demonstrated that LA cleaning does not affect the Thermoluminescence measure.

This thesis develops into five chapters. In the first chapter, we will introduce the LA processes, the second describes the Diagnostic techniques and experimental setup. Instead, in the third chapter we will discuss the materials analyzed, while in the fourth chapter describes the use of by-products generated from LA for consolidation of Cultural Heritage assets and for realization of nanocomposites for high-tech applications. Finally, in the fifth chapter we will conclude the study by listing the achievements.

Abstract

Questo lavoro di tesi, sviluppato nel periodo tra marzo 2012 e novembre 2014, si focalizza sulla ricerca di nuovi metodi di pulizia, diagnostica e restauro peri beni di interesse storico-artistico basati sull'utilizzo della tecnica della Laser Ablation, in diversi mezzi (in aria, in acqua e in vuoto), studiandone l'efficacia su diversi materiali quali leghe, metalli e materiali lapidei artificiali.

La tesi si propone, inoltre, di esaminare diverse tipologie di indagine, di consolidamento ed eventuale restauro conservativo di manufatti archeologici, oltre che introdurre nuove possibili strategie di studio nella diagnostica e nella valorizzazione e fruizione dei beni culturali, attraverso il sempre più vicino contributo delle nanotecnologie e dei nanomateriali, le cui potenzialità vengono applicate a questo settore solo in minima parte.

Obiettivo principale della tesi è verificare in primis l'applicabilità di diverse tecniche, tipiche dell'analisi chimica e fisica alla diagnostica dei Beni Culturali in diversi ambienti, cercando di rendere la metodologia utilizzata il meno invasiva possibile e il più efficace possibile.

Infatti una prerogativa fondamentale è quella di riuscire ad effettuare una pulizia attraverso Laser Ablation sulle diverse tipologie di materiale, direttamente in situ, impiegando apparecchiature e prototipi portatili utilizzabili sia in ambienti subaerei che subacquei (quest'ultimi realizzati durante il corso del dottorato di ricerca) per rimuovere selettivamente croste e patine di alterazione che spesso ricoprono i manufatti archeologici.

Per testare l'efficacia della metodologia diagnostica utilizzata, le indagini sono state effettuate attraverso metodologie non distruttive (o in alcuni casi microdistruttive) su diverse tipologie di materiali (come bronzo, ceramiche e metalli nobili, sia di interesse storico-artistico che di uso commerciale) in diversi ambienti (sia subaerei che subacquei), ottenendo informazioni confrontabili con quelle ottenute in laboratorio.

Gli studi morfologici sono stati effettuati mediante microscopia ottica, la microscopia a scansione SEM e la più recente microscopia a Forza Atomica AFM (poco utilizzata nel campo dello studio dei reperti archeologici e di interesse storico-artistico).

Le analisi chimiche sono state effettuate con diverse tecniche spettroscopiche tra cui la spettroscopia a fluorescenza di raggi X (XRF), la spettroscopia di fotoemissione in seguito a bombardamento di raggi X (XPS), le spettroscopia di fotoluminescenza (PL), la Catodoluminescenza (CL) ed infine la spettroscopia a diffusione di raggi X (EDX).

Altro tema trattato nel presente lavoro, riguarda la generazione del particolato generato dalla Laser Ablation e il suo riutilizzo per applicazioni di restauro e consolidamento di reperti archeologici e per la realizzazione di nanocompositi per applicazioni ad alto contenuto tecnologiche principalmente rivolte al fotovoltaico e all'optpelettronica.

Infatti è stato approfondito lo studio sulla produzione e caratterizzazione di nanoparticelle e nanocompositi a base di TiO_2 e SiO_2, impiegato di recente per la conservazione e la protezione dei Beni Culturali, con il quale, è possibile eseguire sui beni culturali tipologie di rivestimenti trasparenti, idrofobici e consolidanti.

Per quanto riguarda reperti di natura ceramica, è stato dimostrato che il processo di pulizia in LA non pregiudica la possibilità di datare un manufatto in termoluminescenza.

Introduction

Physical methods applied to cultural heritage became, in the last decades, increasingly important and frequent. Today is duty conducting any restoration process using scientific criteria, essential to have all the information to get the knowledge framework of the past and current situation of the cultural object. Therefore, these methods, allows to answer questions about the state of deterioration of the work, of any previous restorations, the authenticity of the artefact etc. Recently, the scientific applications in archaeology is increasing. The junction between all these applications takes the name of "Archeometry". This research area concerns the scientific study, by laboratory analysis of the artefacts based on the interaction radiation-matter, and allow to get any kind of information on the artifacts. The modern approach to the study of cultural heritage is highly interdisciplinary.

In this chapter, we will discuss mainly of the Laser Ablation technique, of the experimental setup, its characteristics, its processes, its applications in the field of cultural heritage, of the production and recovery of nanomaterial (particulate matter) and the subsequent re-use of waste materials nanocomposites with high industrial content. In recent years, technological applications and in particular in the fields of cultural heritage are evolving. The use of laser equipment has increased sharply (both as a diagnostic technique as a method of cleaning and restoration). This technique, in this thesis, was used on archaeological materials, such as ceramics and metal objects, but also on commercial ceramic and metal workshop. My study is based mainly on cleaning phase of archaeological finds and subsequently in recovery of by-products, generated by laser ablation, for construction of high-tech materials. These studies of laser ablation are still developing for optimal control of material removal, due to its peculiarity to process virtually any material with high precision and minimal collateral damage.

The technique of Laser Ablation (LA) is an important contribution of physics to the conservation of cultural heritage. In the last decades, the laser ablation (LA) techniques have shown an excellent alternative to organic solvent in the treatment of metallic surface and in conservation and restoration of cultural heritage [1]. This technique began to be used routinely only since the '90s with the restoration of wooden works, in stone and bronze (Parthenon, the St. Matthew by Lorenzo Ghiberti, the frescoes on wooden of *Santa Maria della Scala* in Siena, the Etruscan bronze *Arringatore* and the *David* by Donatello) [2]. The performance of the LA mechanisms is still being studied nowadays due to their complexity, for which there is not a model that describes the process in a comprehensive manner.

The scientific investigations have focused on the efficiency, selectivity and efficacy of laser ablation, as well as on the possible advantages that it can provide with respect to traditional cleaning techniques [3]. The model most likely accepted provides that the laser ablation on a target, beginning with the absorption of the incident photons by target with the consequent production of heat and photoionization of the irradiated area (thickness of a few microns) up to the evaporation of a thin layer of material and small solid fragments. It is, then, a process of removing material from the object surface through vaporization and erosion processes. At high laser flux, the material is typically converted to a plasma cloud said *plume* (a cloud consisting of atoms, molecules, electrons, ions, solid particles and parts of molten material) of ablated material. The experimental set-up consists of a pulsed laser and a set of optics that have the task of focusing the beam near a target [4].

In this study, laser operation on surface cleaning acquires a considerable importance due to its ability to remove selectively stranger materials than the original surface. However, there are problems in the operation of cleaning such as thermal shock, chemical-physical and mechanical properties of artifacts, alien substrate to be removed, which must be taken into account to be able to have a result that does not change the artifacts characteristics. The most important problem to use the LA processes in cultural heritage artefacts cleaning is the possibility to remove protective layers and decorative elements [5]. This problem can be solved varying the laser parameters during the ablation. In particular, we present in this work a study of ability to laser ablation to remove only impurities without changing the artefact surface. Therefore, in this study several different laser parameters have been tested on both archaeological artefacts and commercial materials, to investigate a larger set of surfaces.

Often the cleaning of artworks involves the removal of dirt from damaged surfaces or fragile substrates. Traditional cleaning techniques such as water, chemical and mechanical cleaning can result in permanent damage. This is a non-contact, selective, and environmental friendly cleaning technique. LA allows deep cleaning without causing any damage to the artwork or monument.

In the first phase of investigation, we performed laboratory studies on the physical mechanism that induces laser cleaning. Many spectroscopies was performed to provide quantitative information on the process, and to determine the optimum laser emission parameters for various materials. Then, we carried out cleaning tests on samples including a large selection of materials, typically employed for archaeological pottery, archaeological metals, and so on and tests on various media as air and marine water. Analyses confirmed that laser cleaning allows highly precise and progressive operations, by removing layers of a few microns per laser pulse, following the stratigraphy of the alterations. Successful operations were achieved on severely degraded artefacts. Selective removal of alteration materials with respect to the original substrate was often applicable, allowing the full preservation of very thin age patinas. Several works on gold, silver and bronze artefacts have definitely demonstrated the effectiveness of LA in metal artefacts cleanness. In fact, the LA remove organic matrix patinations on archaeological artefacts reducing the impurities amount on sample surface [5].

It is possible that these techniques frequently induced environmental pollution and can be toxic for human operators. We studied how to remedy this drawback. Recovering the dispersed material from LA (generally this method we tested on metals in marine water), we can realize nanocomposites materials for high technology used in medical engineering, in the pharmaceutical industry, in biomedical devices, in electronics industry, in construction industry. For example to incorporate in a

single matrix two different nanostructures (nanoparticles produced by LA deposited on carbon nanotubes) with specific properties is a versatile method to transfer and to integrate in a single material the different properties of two materials, enabling to realize multifunctional composites, for using in advanced applications like catalysis, energy storage, nanobiotecnology, optoelectronics, etc. [6] [7].

1.　　　Lasers Physics

The term "laser" is an acronym for Light Amplification by Stimulated Emission of Radiation. The process of light amplification by stimulated emission of radiation (laser) can currently provide electromagnetic radiation with exceptional properties from the infrared over the full visible to the ultraviolet spectral range. It is particularly the coherence in the phase and in the direction of laser emission that has allowed for its wide spread usage in industrial, medical and scientific applications, largely surpassing the capabilities of any other light source. There are different mechanisms for obtaining the coherent emission of light from a medium. Light amplification by stimulated emission of radiation is most commonly realized by pumping an active medium within a cavity or optical resonator.

Lasers are based on the mechanism, that Atoms can absorb or emit Energy via Photons. The Energy is given by

$$E = h\,v$$

where *h* is the Planck Constant and v is the frequency.

Atomic physics describes an atom as a central nucleus of protons and neutrons, surrounded by a cloud of electrons which encircle the nucleus in different orbitals. When appropriate energy is supplied to the atom, electrons can jump from low-energy orbitals (ground state) to high-energy orbitals further away, leading to atomic excitation by the process of energy **absorption**.

Some of the electrons in the high-energy orbit spontaneously return to the ground state, releasing the difference in energy in the form of a photon, with a wavelength, which depends exactly upon the difference in energy of the 2 states and has a random phase and direction. This process is called **spontaneous emission** and forms the basis of light emitted by a neon sign, fluorescent light bulb and television tube.

This emitted photon can collide with one of the mirrors in the resonating cavity and reflect back into the lasing medium causing further collision with some of the already excited atoms. If an excited atom is struck, it can be stimulated to decay back to the ground state, releasing two photons identical in direction, phase, polarization and energy (wavelength). This process is termed **stimulated emission**. These mechanisms are illustrated in Figure 1.
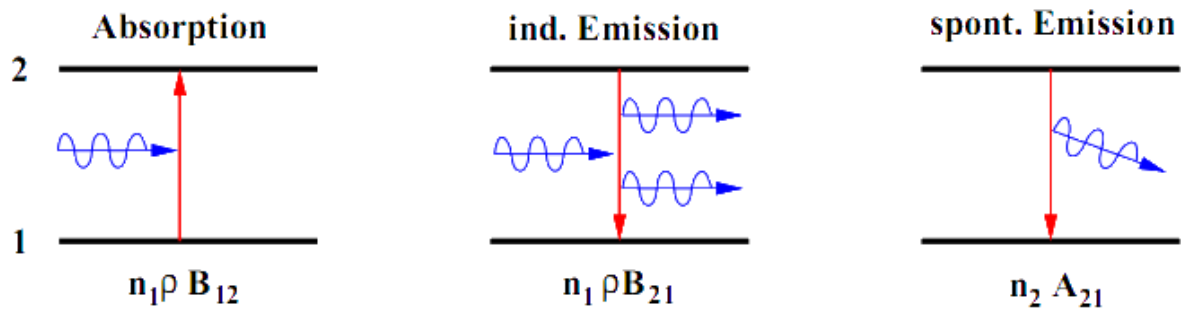
Figure 1: illustration of the emission and absorption process

A small number of photons are allowed to escape from the lasing medium though the partially reflective mirror of the output coupler. This is the usable laser light and may be in the visible spectrum or beyond (infrared or ultraviolet).

A Laser consists mainly of three parts, a lasing medium that allows the induced transitions due to the population inversion, a pump source, which supplies the required energy, and a resonator, which reflects the emitted light, so that the process of induced transitions can be activated. A Laser, which works on the principle of a two-level-system, can not be realized, because it is not possible to create a population inversion.

In view of the black body radiation, Einstein was able to formulate the equilibrium state of a quantized radiation field with its source and derive the three basic processes of *absorption*, *spontaneous emission* and *stimulated emission* together with the respective probabilities described by the Einstein coefficients B_{nm}, A_{mn} and B_{mn}.

Among these three processes, only stimulated emission generates electromagnetic radiation equivalent in *frequency*, *phase*, *polarization* and *direction* within the amplification of light. These properties are responsible for the distinctive coherent emission of a laser. Then, the elements of a laser are configured to particularly enhance stimulated emission in its competition with absorption and spontaneous emission. These against coherent amplification by nullify photons or generating incoherent radiation. Therefore, unlike other forms of light, laser light has special properties that make it significantly more effective and dangerous than conventional light of the same power.

The laser light particles (photons) are usually:

- **Monochromatic**: consisting of a single wavelength or colour
- **Coherent**: photons are in phase (like marching soldiers)
- **Collimated**: photons are almost in parallel (aligned), with little divergence from the point of origin

A laser consists of three basic components:

- A **lasing medium** or "gain medium": May be a solid (crystals, glasses), liquid (dyes or organic solvents), gas (helium, CO_2) or semiconductors.
- An **energy source** or "pump": May be a high voltage discharge, a chemical reaction, diode, flash lamp or another laser.

- An **optical resonator** or "optical cavity": Consists of a cavity containing the lasing medium, with two parallel mirrors on either side. One mirror is highly reflective and the other mirror is partially reflective, allowing some of the light to leave the cavity to produce the laser's output beam – this is called the output coupler.

The active medium usually provides a three or four level structure of quantized states that are coupled in a particular manner via radiative and non-radiative processes.

A Laser uses the principle of induced emission to create coherent monochromatic light of high intensity. A cascade effect of stimulated emission of photons occurs, resulting in further amplification (optical gain) and soon many of the atoms emit light along the same axis. For a laser to sustain function, the majority of the atoms must be maintained in the excited state, hence called "population inversion". This is achieved by the continuous input from the energy pump (continuous wave laser) or by intermittent pumping resulting in a pulsed wave laser. Coherence is a property of waves that enables stationary interference. Considering the Maxwell-Boltzmann distribution, it is clear that the ground state has a higher population than the excited state in thermal equilibrium.

The pumping process serves to deposit energy into the active medium, which populates the excited energy levels and brings the system into the state population inversion between the two levels that serve for the lasing transition.

When the population of an excited state level exceeds the population in the energetically lower level, the probability of stimulated emission surpassed the respective rate of absorption. Pumping an active medium for a continuous, steady state cycling through the three or four levels of the system and indirectly populating the state involved in the stimulated emission process is commonly achieved by optical pumping (flash or arc lamps, diodes or other lasers).

Further, considering the competition between spontaneous and stimulated emission, the medium is commonly brought into an optical resonator, which consists of reflective faces that trap the emission in specific modes. The dimensions of the cavity determine the frequencies at which these modes can oscillate. By introducing the resonator, the radiation field is directly coupled back to the active medium. This allows for the number of photons per cavity mode to surpass unity and under these conditions, the probability of stimulated emission exceeds the value for spontaneous emission. For this case, the threshold for lasing is meet when the amplification by stimulated emission further compensates the losses within the cavity. When this occurs, the modes of the cavity that are within the bandwidth of the gain profile of the medium spontaneously begin to oscillate and the system transfers into the state of lasing.

A closed cavity (confinement in all three dimensions) and an open cavity (on-axis confinement in one dimension) are principally possible but the exceedingly high number of modes for a reasonable cavity size make closed configurations unpractical for the wavelengths in the ultraviolet, visible and near infrared spectrum.

Open cavities used for lasers usually consist of two high reflective mirrors, where one of the mirrors shows a slightly lower reflectivity in order to allow for a small percentage of the coherent emission to escape the cavity. The number of nodes along the axis of the resonator defines the longitudinal modes of the cavity and their frequencies. Described process is shown in figure 2.
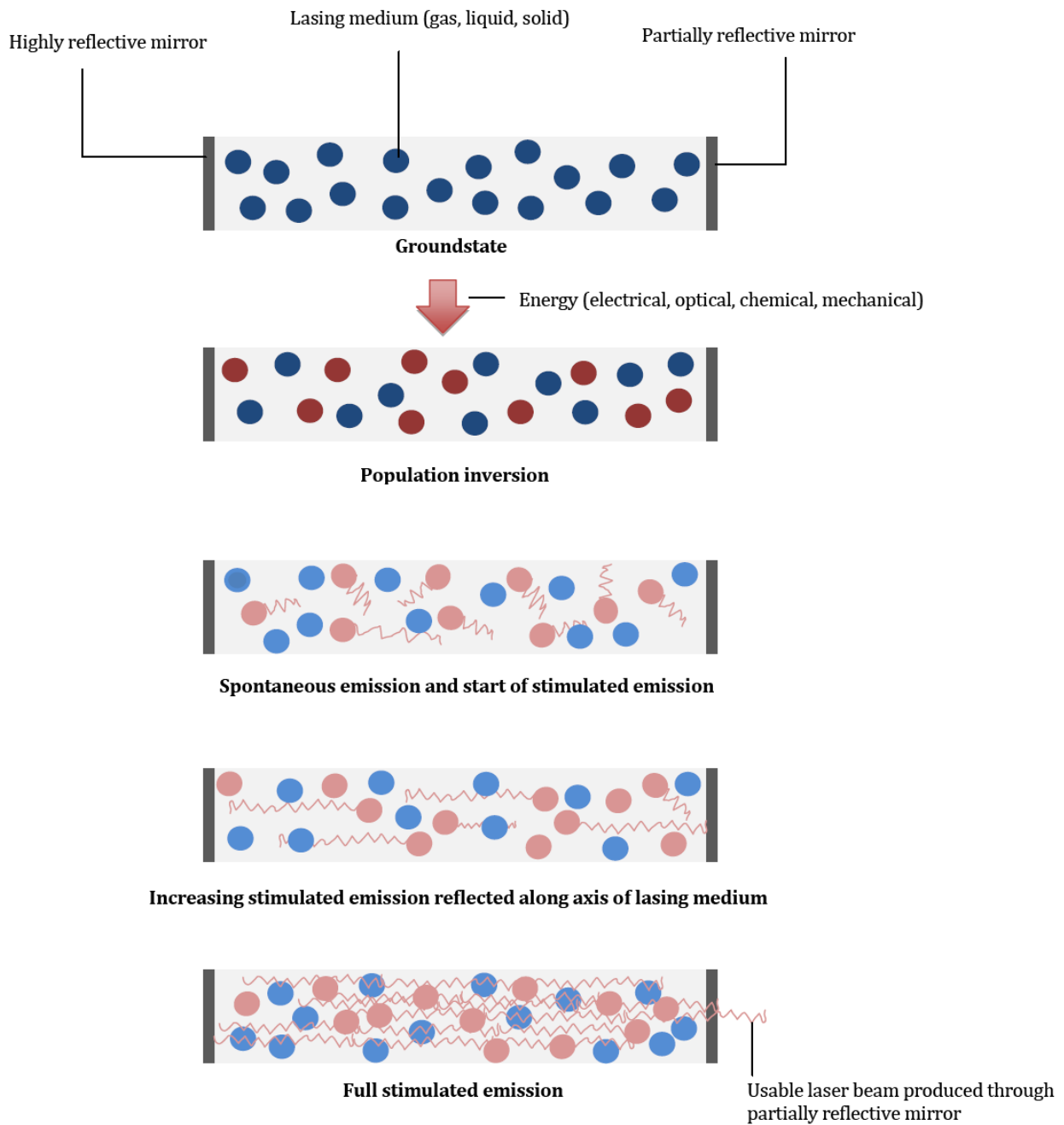
Figure 2: Production of the light beam

While most lasers are designed to operate with a Gaussian profile in the cross-section of the intensity distribution normal to the axis of a cavity, the transversal mode of an open cavity can also show nodes (two dimensional Laguerre polynomials for cylindrical symmetry). The structure of the transversal electromagnetic mode (denoted by TEM_{nm}) is determined by the curvature of the cavity mirrors and their distance. These are, usually, adjusted to meet the stability criterion, which describes the capability to contain the radiation within the cavity and avoid losses out of the open configuration. Since the geometry varies for different transversal modes, the frequency of the emission from different modes can be shifted from the frequency of the ideal Gaussian TEM_{00} mode.

1.1.   The Nd YAG-Laser

As described above, when light is absorbed or emitted, electrons transfer takes place between the energy levels. An electron transition from the level with the energy E_1 to a level with the energy E_2 can occur if an incoming photon is absorbed with the energy $E_{Ph}=E_2-E_1$. In the reverse case, a photon with the energy $E_{Ph}=E_2-E_1$ is emitted if a transition of an electron of the atom takes place from a state with energy E_2 to one with energy E_1. The two processes of absorption and emission differ in that an external electromagnetic field with the energy E_{Ph} must be present for absorption, whereas no field is present for emission.

It is seen that photons with a slightly different energy also take part in these processes. The reason for this is that the energy levels are broadened due to various mechanisms. Depending their vibration state the atoms are due to their temperature and how they are affected by interactions with their environment, there is a broadening dE of energy levels, which means that photons within this region are accepted. The width of the transition is given by the half width dE for the relevant transition (Fig. 3a). The same theory is valid for emission. E_0 corresponds to the value E_2-E_1. Furthermore, it should be mentioned that there are also situations in which this value can be displaced. The shape of the absorption curve corresponds to a Gaussian distribution. By definition dE is the width of the curve at which the absorption has fallen to one half of the maximum value. This is known as the full width at half maximum (FWHM). If there are other transitions within the vicinity of this transition, they may overlap, producing a substantially wider absorption curve (Fig. 3b). This is particularly important in the case of the absorption of laser diode radiation in Nd-YAG, which is discussed later.
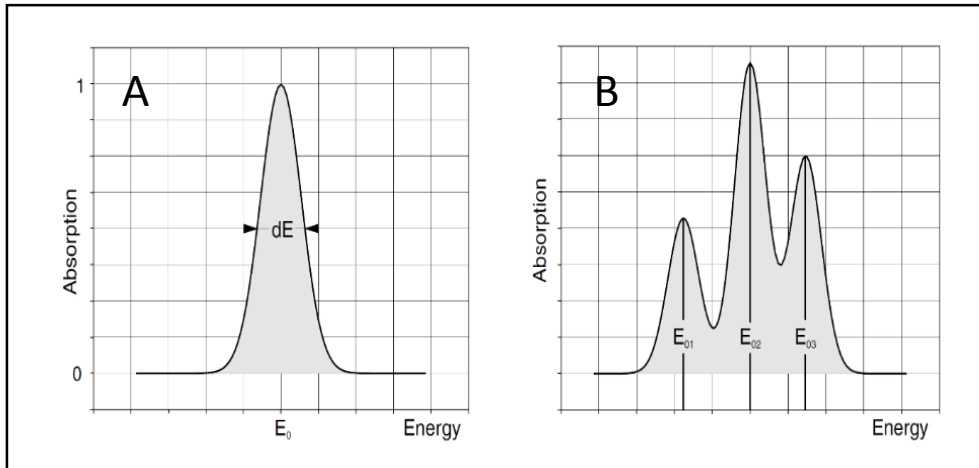
Figure 3: A) dE absorption curve. B) Absorption curve of laser diode radiation in Nd-YAG

In principle, an atom may have any number of energy levels, but they must be discrete. The transitions between the individual levels take place according to defined selection criteria. When the atom is excited with a defined energy, an emission spectrum is observed with characteristic energies and this spectrum gives precise information about the energy levels involved. Excitation by optical pumping has therefore developed as a very important method used in spectroscopy. It is also an indispensable technique for the excitation of a number of different types of lasers.

Optical pumping in conjunction with Nd-YAG lasers is of particular interest, because these have become widely accepted for many uses, along with the CO_2 laser. The laser active material which, in the case of the Nd-YAG laser, is excited by optical pumping, consists of Neodymium atoms that are accommodated in a transparent host crystal (YAG=Yttrium Aluminium Garnet). Whereas up to a few years ago Nd-YAG lasers were almost excited using discharge lamps, optical pumping with laser diodes is becoming more significant. This is because laser diodes are available economically and they emit narrow band light at high optical powers, which matches the energy levels of the Nd-YAG crystal (Fig. 4). The advantage over the discharge lamp is that the emission of laser diodes is nearly completely absorbed by the Nd-YAG, whereas the very wide spectral emission of discharge lamps is absorbed to only a small extent. The efficiency of optical pumping with discharge lamps is about 3%, but figures of up to 50% can be achieved using laser diodes.

Since the Nd atoms are situated within the YAG host crystal, the otherwise degenerated energy levels of the isolated Nd atom split into a number of states. This gives rise to the ground state $^4I_{9/2}$ from 5 substates and the state $^4F_{5/2}$, which can be pumped from 5 substates. Since the wavelength of the pump-light source (diode laser) can vary within low limits, a total of three to four transitions can be pumped with high efficiency. The Nd atoms of the $^4F_{5/2}$ state pass very quickly into the laser output level $^4F_{3/2}$. The laser transition, which is technically most interesting takes place between the $^4F_{3/2}$ state as starting level and terminates in the $^4I_{11/2}$ state with an emitted wavelength of 1064 nm. From here the Nd atoms relax again into the ground state $^4I_{9/2}$ until the pumping process starts from the beginning again. The Neodymium, therefore, has an ideal four level system [8].
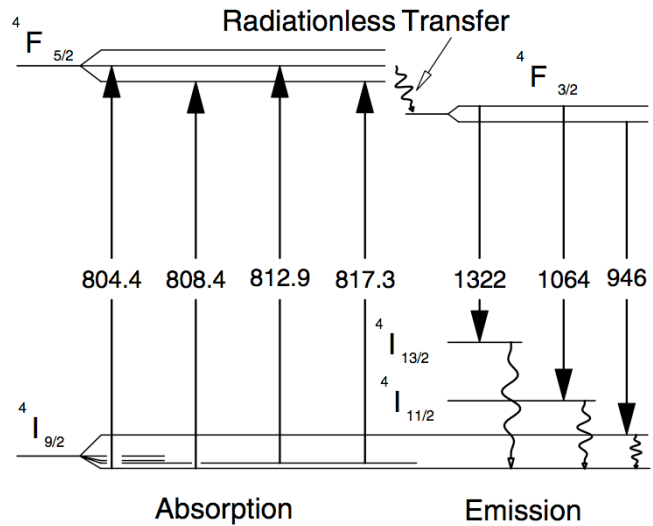
Figure 4:The scheme for the Nd:YAG medium with the four-levels relevant for lasing [9]. Some energy levels of the Nd atom are illustrated. Here, only those are shown which are significant for optical pumping with laser diodes and which are important for the laser

The principle is shown in figure 5. Under the radiation of a light field (optical pumping), transitions from ground state 1 to the upper level 4 occur. The reverse processes from state 4 to state 1 are prevented by very fast transitions from state 4 to state 3 without radiation. Laser transition takes place from level 3 into level 2 that is thermally not populated. Finally, Nd atoms relax again back to ground state 1.
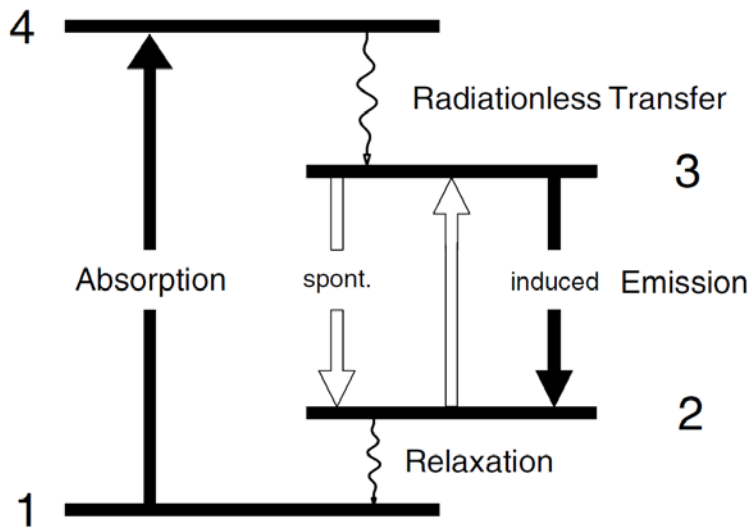
Figure 5: Absorption and emission process of a 4 energy levels system

1.2.   Laser Ablation

The simplest application of laser ablation is to remove materials from a solid surface in a controlled process. Very short laser pulses remove material so quickly that the surrounding material absorbs very little heat, so laser drilling can be done on delicate or heat-sensitive materials. Several operators have employed laser ablation to cleaning surfaces and produce nanoparticles of metal, metal oxides and so on.

Laser cleaning represents the most important contribution of physics to the restoration of cultural heritage. A number of scientific investigations were reported over the last two decades in journals, conference proceedings, and books, focusing on the efficiency, selectivity, and then effectiveness of laser ablation, as well as on the possible advantages, which can provide respect to traditional cleaning techniques [2].

The ablation process depends on thermal and optical properties of the materials and on laser parameters such as wavelength, laser intensity, pulse duration [10].

The main principle of Laser ablation is the conversion of optical energy into thermal energy via electronic excitation. If the energy of the Laser is high enough, the chemical bondings of the material can be destroyed, so that the material vaporizes and may be ejected from the material.

By this process, it is possible to create small holes on the surface of the material. The hole structure, especially the depth, depends on the optical properties of the material and on the wavelength of the laser.

We said above, that the processes governing ultra short pulsed laser ablation are not again completely understood. Currently, several studies have been done on the mechanisms of laser absorption on material, as well as its removal and expansion but none of them can be considered exhaustive.

Important physical effects occurring with femtosecond LA. Femtosecond laser ablation has the important advantage in such applications, compared with ablation using nanosecond pulses, because there is little or no collateral damage due to shock waves and heat conduction produced in the material being processed. To choose the best laser for cleaning through LA, we must consider all the parameters, such as wavelength, frequency and energy [11][12].

In the following, we describe the basic processes occurring during the irradiation of solid targets with ultra short, nanosecond laser pulses. The detailed course of the very complex phenomenon occurring during the interaction depends strongly on the parameters of the laser pulse and the target material. Typical intensities used in the nanosecond laser ablation and deposition experiments are in the range of 10^8 - 10^9 W/cm^2. At intensities above $10^{13} - 10^{14}$ W/cm^2 the ionization of any target material takes place early in the laser pulse time. For example, femtosecond pulse interacts with a dielectric, almost

full single ionization of the target occurs at the beginning of the laser pulse. Following ionization, the laser energy is absorbed by free electrons due to inverse Bremsstrahlung and resonance absorption mechanisms and does not depend on the initial state of the target. Consequently, the interaction with both metals and dielectrics proceeds in a similar way. The interaction of a long pulse and metals occurs at relatively low intensity compared with that for a transparent dielectric whose absorption is negligibly small [11].

Another very important parameter is the medium where the process takes place.

In this thesis, we will consider liquid as the principal medium, because, nowadays, it grows more and more the need to apply this technique on underwater archaeological artifacts. The large part of our studies have been done on the nanoparticles production in liquid. This type of technique is called LASiS (Laser Ablation Synthesis in Liquid).

1.2.1. LASiS

The laser ablation synthesis in liquid solution (**LASiS**) of nanomaterials (**NMs**) gained increasing interest for its versatility, low cost and easily execution [13].

Laser ablation implies the removal of microscopic and nanoscopic amounts of matter from the surface of solid material. Usually, the material must undergo a change of the fundamental state of aggregation and transform into some volatile phase, e.g., a gas or a plasma. The transition from the solid phase to the gas phase can occur in a stepwise fashion by the melting of the solid and evaporation of the liquid. Boiling occurs when the vapor pressure of the liquid phase exceeds the ambient pressure. Boiling rates become very high when the temperature of the liquid approaches the critical temperature. The latter case is sometimes referred to as 'phase explosion' [14].

The number of scientific reports on LASiS of functional materials for specific nanotechnology applications is continually growing. For instance, NMs obtained by LASiS were applied in SERS labelling, self-healing optical limiting devices, friction-reducing coatings, photonic materials, antibacterial nanocomposites, neural electrodes, water splitting, catalysis and cell sorting/targeting. In LASiS, the NMs are obtained by focusing laser pulses on a bulk target immersed in a liquid solution (Fig. 6).
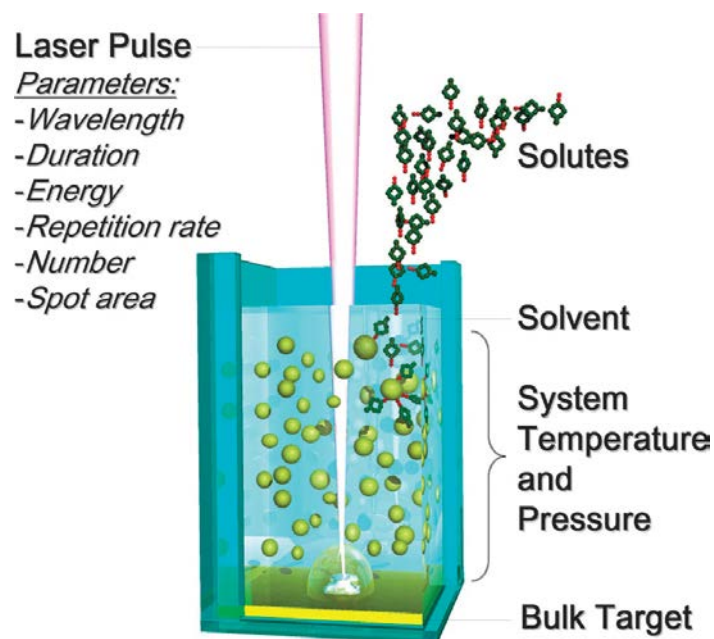

Figure 6: main experimental parameters of LASiS [15].

13

The target can be either a single piece or pressed powder, although the dynamics of the synthetic process does not vary. Nanoparticles (NPs) formation may take place by various mechanisms like nucleation and growth or ejection of hot drops and solid fragments from the target [15]. The parameters of the synthesis are divided into two categories:

- material parameters (bulk target, solvent and solutes, system temperature and pressure)
- laser parameters (wavelength, duration, energy, repetition rate, number of laser pulses and the spot area on the target)

Laser irradiation is generally used to obtain the size refinement of nanomaterials, while maintaining their initial composition and it does not fall within the topic of this perspective.

Under certain conditions, sublimation may occur, a direct transition between the solid phase and the gas phase. Otherwise, a direct transition to a fluid phase can be accomplished by very rapid heating of solid matter to temperatures higher than the critical point.

Finally, laser radiation of sufficiently high intensity leads to ionization and transforms solid material into dense plasma. When the laser fluence is kept constant while the pulse duration is decreased, the optical electric field strength will, at some point, exceed the breakdown threshold of the material. Thus, plasma formation is expected to become the dominant mode of laser ablation when the pulse duration is made shorter and shorter. However, in opaque metals and semiconductors for pulse durations of the order of 100 fs, ablation takes place before the onset of plasma formation [16].

The main stages of LASiS can be resumed as follows (see Fig. 7):

The process starts with the absorption of the laser pulse by the bulk target, and then a plasma plume containing the ablated material expands into the surrounding liquid, accompanied by the emission of a shockwave. During the expansion, the plasma plume cools down and releases energy to the liquid solution. This phenomenon generates a cavitation bubble that expands in the liquid and then collapses on a time scale of the order of hundreds of microseconds, by emission of a second shockwave.

We can identify four main parameters whose profiles in time and space primarily determine the phase and structure of final NMs:

- temperature (T)
- pressure (P)
- concentration of the ablated material (C_M)
- concentration of solution species (C_S)

The most complex point in LASiS is that, due to the hemispherical symmetry of the laser ablation phenomena, the four parameters are not uniform in space neither constant in time. To gain a better perspective on the evolution of the four parameters, it is instructive to describe the temporal sequence of the ablation stages when a single laser pulse hits the target (Fig. 7). In the following, we assume that the fluence (energy delivered per unit area) is above the ablation threshold (usually in the $10 - 10^3$ J cm^{-2} range) and we set the time $t=0$ as the instant when the laser pulse hits the target.
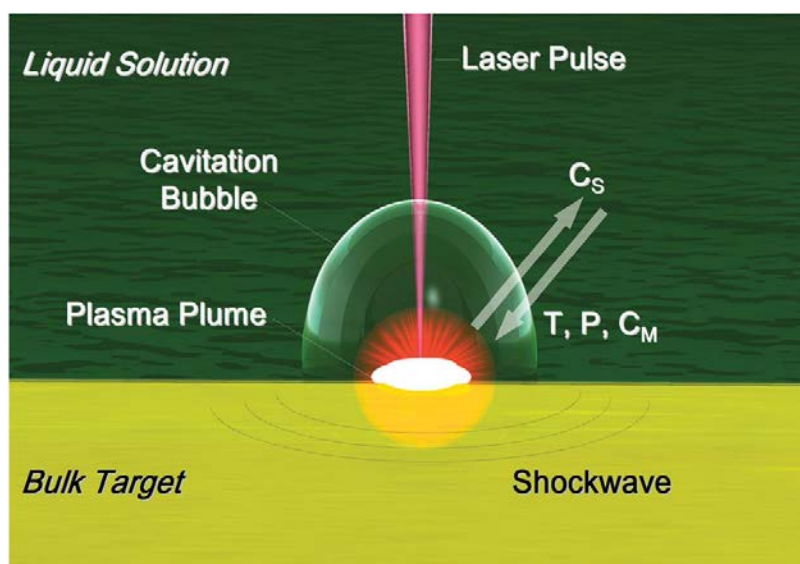
Figure 7:the main stages of LASiS.The white arrows indicate that, upon increasing the distance from the laser spot, the temperature(T), pressure(P), and concentration of the ablated material(Cm)decrease, while the concentration of solution species(Cs)increases [15]

1. For t<0 the laser pulse must pass through a layer of liquid before reaching the target. Laser energy should be delivered to the target only, and not to the liquid solution. In particular, liquid breakdown must be avoided. There is a fluence threshold (F_{th}) that must not be exceeded in order to avoid nonlinear optical effects like multiphoton absorptions from the liquid. Fixed the energy per pulse, longer pulses have higher F_{th} and permit the delivery of more energy to the target. The liquid solution should be transparent at the laser wavelength, although there are frequent exceptions to this rule. In fact, water absorption at 1064 nm is not null. Usually, under ordinary LASiS conditions, it is assumed that solvent absorption does not play a relevant role in NPs formation, because the portion of energy delivered to the target is orders of magnitude larger than that absorbed by the liquid. Only in specific cases the liquid solution can significantly absorb or scatter laser light, due to the presence of absorbing solutes or of already formed NPs, with consequent reduction of the energy transferred to the target.

2. From t = 0 to pulse duration (τ_{pulse}) there is absorption of the laser pulse. Due to the high photon density, linear and nonlinear absorption processes occur when the laser pulse hits the target. The thickness of the target in which light is absorbed is of the order of the material skin depth (few nanometers). Nonlinear optical processes depend on the electromagnetic field intensity, which is proportional to the pulse fluence *f* divided by the pulse duration τ_{pulse}. At the fluence required for LASiS, pulses of less than a few ps lead preferentially to instantaneous multiphoton absorption processes and, on cascade, to localized photoinduced ionization. Since optical absorption is simultaneous to laser–matter interaction, direct photoionization lasts for a time equal to τ_{pulse}. Direct photoionization is highly probable for a pulse duration of up to 10^{-8} s. However, by increasing τ_{pulse} above 10^{-12} s, that is the minimum time required for the electron–lattice thermalization, the electron kinetic energy can be released as thermal energy to the lattice. In this case, thermal processes like thermionic

15

emission, vaporization, boiling and melting may occur simultaneously to photoionization, affecting a larger volume than that defined by the spot area and the target skin depth.

3. For t = 10^{-12} s to 10^{-10} s there is detachment of the ablated material. After multiphoton absorption and direct photoionization, the locally induced space-charge separation fields and electron–ion collisions initiate, on a timescale of 10^{-12} s, the detachment of matter from the target. Then, the detachment proceeds sustained also by the transfer of kinetic (thermal) energy from excited electrons to the lattice, namely by heating of the lattice, which occurs on a timescale of several ps. The temperature difference between the irradiated zone and the rest of the system is very large, and solid targets dissipate heat very efficiently, therefore material detachment occurs by thermal and coulombic mechanisms in a region almost coincident with the laser spot. In the literature, no differences were reported in the detachment of ablated material, on the timescale of 10^{-12} s to 10^{-10} s, when the process takes place in gas or in liquid phase. Nowadays technology is not able to reach such high spatial and temporal resolutions. However, physical parameters of detached material are crucial for following steps of NMs formation (nucleation, growth and reactivity with solution species). Therefore, understanding the process of material detachment is a key point for controlling the versatility of LASiS. The precise description of the ablation mechanism is not simple and multiple fragmentation processes are possible, depending on laser parameters, even simultaneously in different locations within the laser spot. The most popular theory exploits classical thermodynamics as a first approximation to describe laser ablation.

In this frame, only three kinds of thermal processes may lead into material detachment from a laser-irradiated target: vaporization, normal boiling and ''explosive boiling''. Under ordinary LASiS conditions and with laser pulses shorter than 10^{-7} s, ''explosive boiling'' is considered the main thermodynamic mechanism of material detachment from the crater. Explosive boiling, also called ''phase explosion'', occurs when solid matter is rapidly superheated (320 K) up to the thermodynamic critical temperature, at which the spinodal decomposition in vapour and liquid phase in the irradiated material occurs by homogeneous nucleation. When energy is transferred to the target by ps and fs pulses, however, molecular dynamics calculations evidenced that material detachment is too fast and far from thermodynamic equilibrium to be described by explosive boiling. In this case, the ablation mechanism is generically defined as ''fragmentation'' and consists of the detachment of hot atoms, vapours and liquid drops under out of equilibrium conditions (Fig. 8).
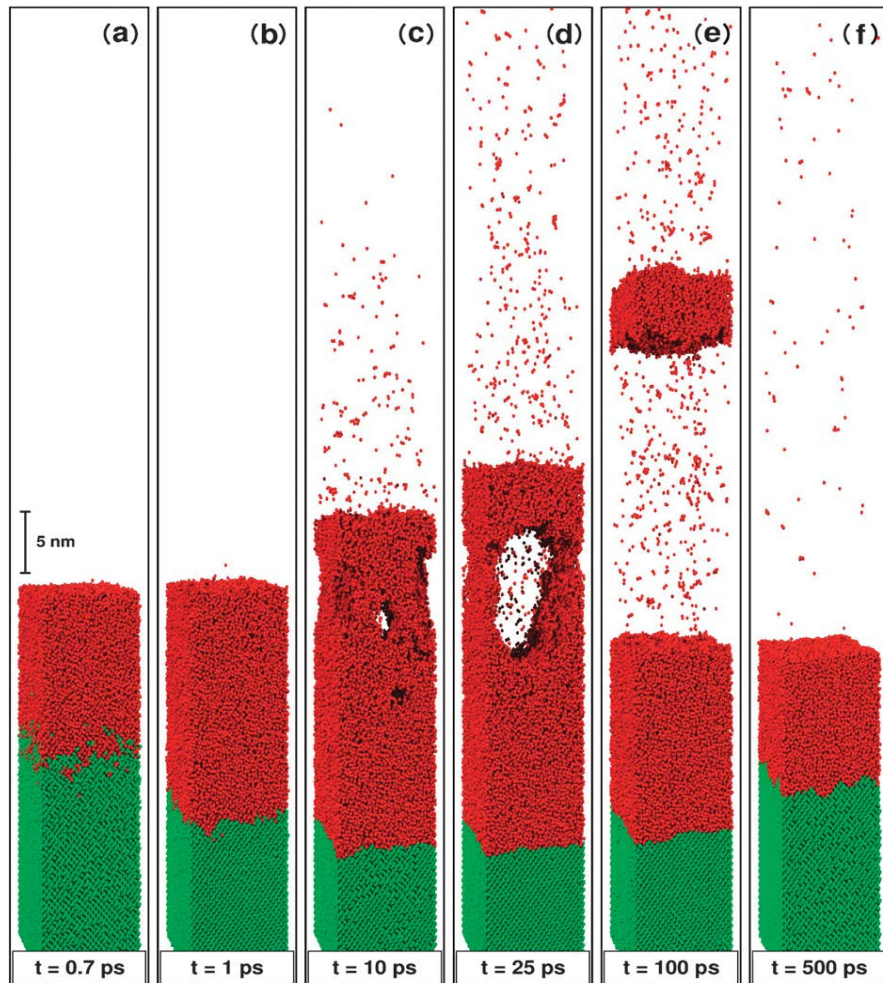
Figure 8: ''fragmentation'' calculated by molecular dynamics simulations, which show the structural evolution of the Si(100) substrate irradiated with a 500 fs (266 nm) laser pulse at a fluence of 0.255 J cm^{-2} [17].

Although thermodynamics and molecular dynamics (MD) provide useful information about the first instants of material detachment from the target, several unclear points are principally related to the effect of photoionization, of photomechanical stress and of plasma confinement on the crater surface due to the liquid buffer. In particular, photoionization could contribute to material detachment by coulombic explosion, similar to what was observed during laser irradiation of particle suspensions. Simultaneously to the ablation process, the recoil pressure of the ablated material drives one shockwave propagating into the target and a second specular shockwave counter propagating into the liquid solution, with supersonic velocity (of the order of 10^3 m s^{-1}). A shockwave is a pressure wave travelling in a medium and implies an abrupt discontinuity in density and temperature along its front.

The energy of shockwaves generated by laser ablation is of the order of 10–50% of the absorbed pulse energy. Shockwave propagation heats the liquid and the target and may promote the detachment of matter from the crater. The ablated material contains highly ionized species due to high temperature and direct photoionization, hence it is considered a

non-equilibrium "plasma plume". The plasma plume generates light with an emission spectrum composed of continuous background and discrete lines. The continuous emission background is caused by bremsstrahlung and radiative recombination, while discrete emission is typical of the relaxation of excited atomic and molecular species. Plasma temperature, pressure and density are of the order of 10^3 K, 10^{10} - 10^9 Pa and 10^{22-23} atoms per cm^3 respectively. After the end of the laser pulse, the plasma plume has a lifetime of the order of tens of ns: in the first ns, the emission is dominated by the continuum, while discrete atomic and molecular lines prevail in the last ns. The evolution kinetic of the plasma plume is very fast, because heating by the laser pulse abruptly alternates with cooling due to plume expansion and heat exchange with the solvent. Moreover, melted drops and, sometimes, solid fragments can be present in the plasma plume. Therefore, thermodynamic equilibrium is not reached in the plasma plume and its emission does not obey Planck's law. When τ_{pulse} is of the order of 10^{-11} s or more, there is a temporal and spatial overlap of the laser pulse with the plasma plume, meaning that the plume itself can absorb energy from the laser pulse. This effect is called "plasma shielding" because it reduces the amount of laser energy directly delivered to the target, while increasing the temperature and the lifetime of the plasma plume.

4. For t = 10^{-10} s to 10^{-7} s there is an expansion and quenching of plasma plume. Although in the first picoseconds after the arrival of laser pulse, the physics is similar for laser ablation in gas or in liquid, for t = 10^{-10}–10^{-9} s an important difference is observed because the liquid buffer strongly confines the plasma plume onto the crater area. The confinement slows down the cooling rate at the interface between the ablated material and the target, because the hot ablated material can provide thermal energy to the underlying target. As a final result, the ablation yield in liquid is higher than in gas because a larger portion of the target reaches the energy threshold for detachment. The important result is that, in liquid, target ablation takes place by energy transfer both from the laser pulse to the solid target and from the plasma plume to the heated target, and the latter process may prosecute for several nanoseconds after the end of the laser pulse. For times shorter than about 10^{-10} s, the spatial gradients of T, P, C_M and C_S can be considered very sharp and one can identify three regions: the solid target, the expanding plasma plume and the liquid solution. After about 10^{-10} s, the plasma plume expands and cools in the solution by releasing its energy to the liquid buffer on one side, and to the solid target on the other side. The liquid is heated up to temperatures of the plasma plume, i.e. 10^3 K, with consequent degradation, ionization and pyrolysis of solution molecules. During this process, the spatial gradients of T, P, C_M and C_S become smoother and rapidly change in time and space, while target and solvent species mix together. Semi-quantitative estimations of these gradients are accessible by experimental and theoretical studies, but their reliable quantitative evaluation is missing at the moment.

A very important point of LASiS is the lack of clear information about the timescale of the nucleation and growth processes. Regarding the start of the nucleation, the concentration, the temperature and pressure are important parameters and, unfortunately, can not be deduced from the literature concerning laser ablation in gas. Optical emission spectroscopy confirmed that reactions between target and solvent species may occur already in the plasma plume, but did not provide quantitative information about the relevance of such a

phenomenon. Moreover, it is not clear if molten material preferentially undergoes solidification or further vaporization and, subsequently, NMs nucleate and grow. Besides, during laser ablation in gas, a fraction of the detached material is redeposited into the crater, while it is not clear what is the extent and what are the parameters governing this process during laser ablation in liquids.

The size distribution of NPs obtained by LASiS is always lognormal. The sole exception is when laser pulses modify already formed NPs. Granqvist et al. showed that NPs have lognormal size distribution when their growth is fed by atom diffusion simultaneously to the drift of NPs through a finite growth region [18] [19]. Subsequent NPs agglomeration does not influence the lognormality if it takes place under the same drift conditions. In LASiS, the finite growth region is the area between the target and the liquid solution, while NPs drift velocity is provided by the expansion of the ablated material.

5. For $t = 10^{-6}$ s to 10^{-4} s there is an expansion and collapse of cavitation bubble. The plasma plume is typically extinguished after a time of $10^{-8}–10^{-7}$ s. The energy released by the plasma plume to the surrounding liquid induces the rise of a cavitation bubble on a timescale of $10^{-7}–10^{-6}$ s, which expands up to times of the order of 10^{-4} s (Fig. 9) [15].
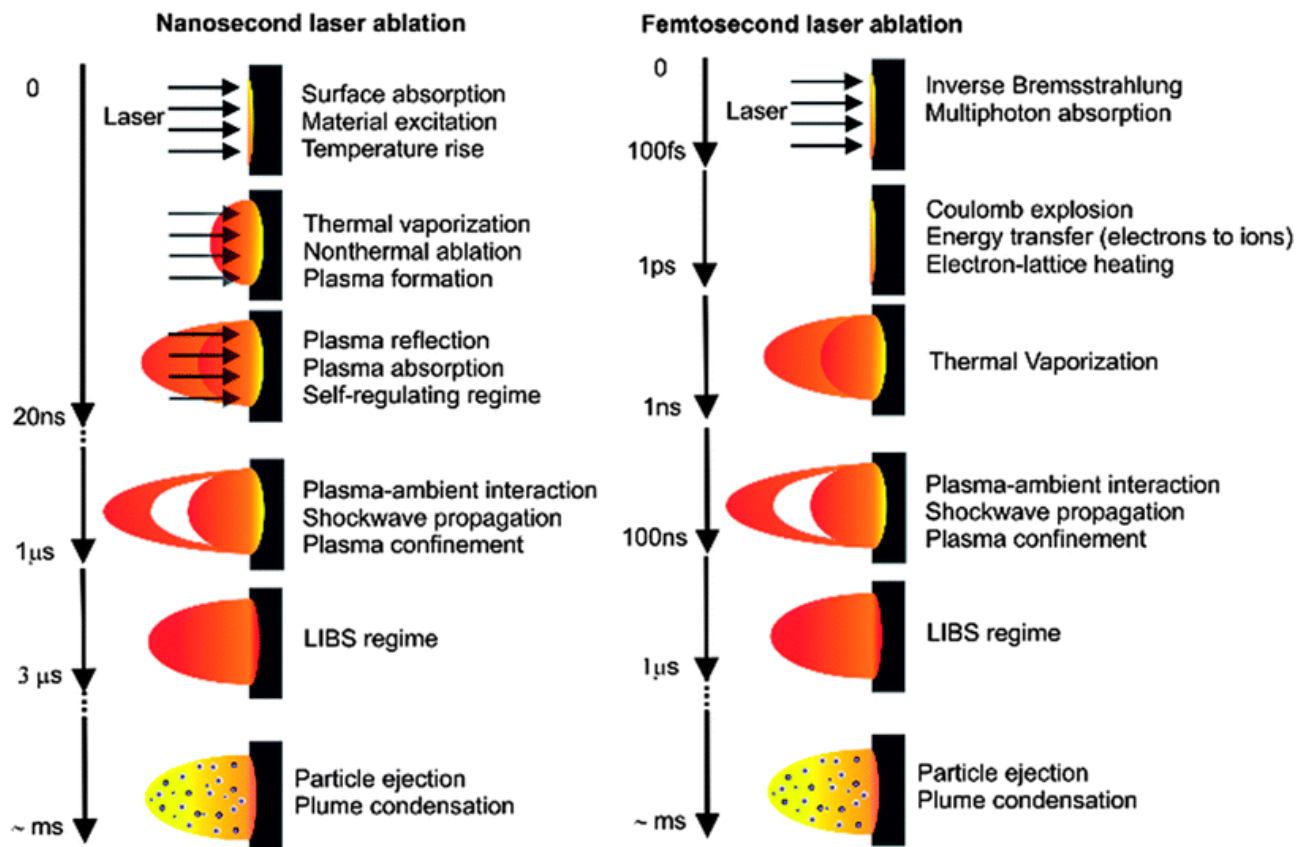
6.

Figure 9: nanosecond and femtosecond laser ablation mechanism.

The bubble travels with supersonic speed ($>10^3$ m s^{-1}) in the liquid up to a maximum radius of the order of millimeters, under ordinary LASiS conditions.

During its expansion, bubble's temperature decreases and bubble's internal pressure drops to a value lower than in the surrounding liquid. At this stage, the bubble collapses emitting a shockwave. This is the last physical process related to laser ablation of a target in liquid solution.

In principle, already formed NPs can travel in front of expanding cavitation bubbles. However, some authors suggested that NMs are formed inside the bubble during its expansion, on a time scale of 10^{-6}–10^{-4} s. Since the NMs come from the initially hot plasma region, and the cavitation bubble originates by the release of heat from this region to the surrounding liquid, the hypothesis that NMs are inside the bubble is realistic. This is a relevant point because the concentration of solution species inside the bubble is much lower than in the liquid. In addition, solution species inside the bubble are in higher energetic states and the temperature inside the bubble is higher than in the surrounding liquid during bubble expansion.

Thermal conductivity of the gas is lower than that of the liquid; therefore, NPs that form inside the bubble remain hot for longer time than in the liquid. For the same reason, the temperature gradient at the bubble/liquid interface may promote nucleation and condensation of NMs. There is experimental evidence that excited target species still exist inside the cavitation bubble, but there is no quantitative insight into the spatial distribution of the ablated matter, namely one cannot exclude that the majority of NMs are already formed and are located elsewhere in the solution.

When the bubble collapses, high energy is released by emission of a shockwave. It has been evaluated that temperature and pressure of the same order of the plasma plume (10^3 K and 10^{10} Pa) are reached in the collapse point, with possible effects like aggregation and phase transition of the already formed NMs or material detachment from the target.

7. For t $> 10^{-4}$ s there is a slow growth and agglomeration of NMs. After the shockwave generated by the collapse of the cavitation bubble, the system reaches steady state physical and chemical conditions. In this stage, NMs can undergo minimal modifications due to the condensation of ablated atoms and molecular clusters that still survive in solution. If NMs dispersion is not stable, agglomeration starts, which will yield precipitation on a timescale longer than minutes for micrometric and nanometric particles. Depending on the NPs composition, also surface oxidation can occur or prosecute at this stage.

The 6 processes are described in Figure 10.
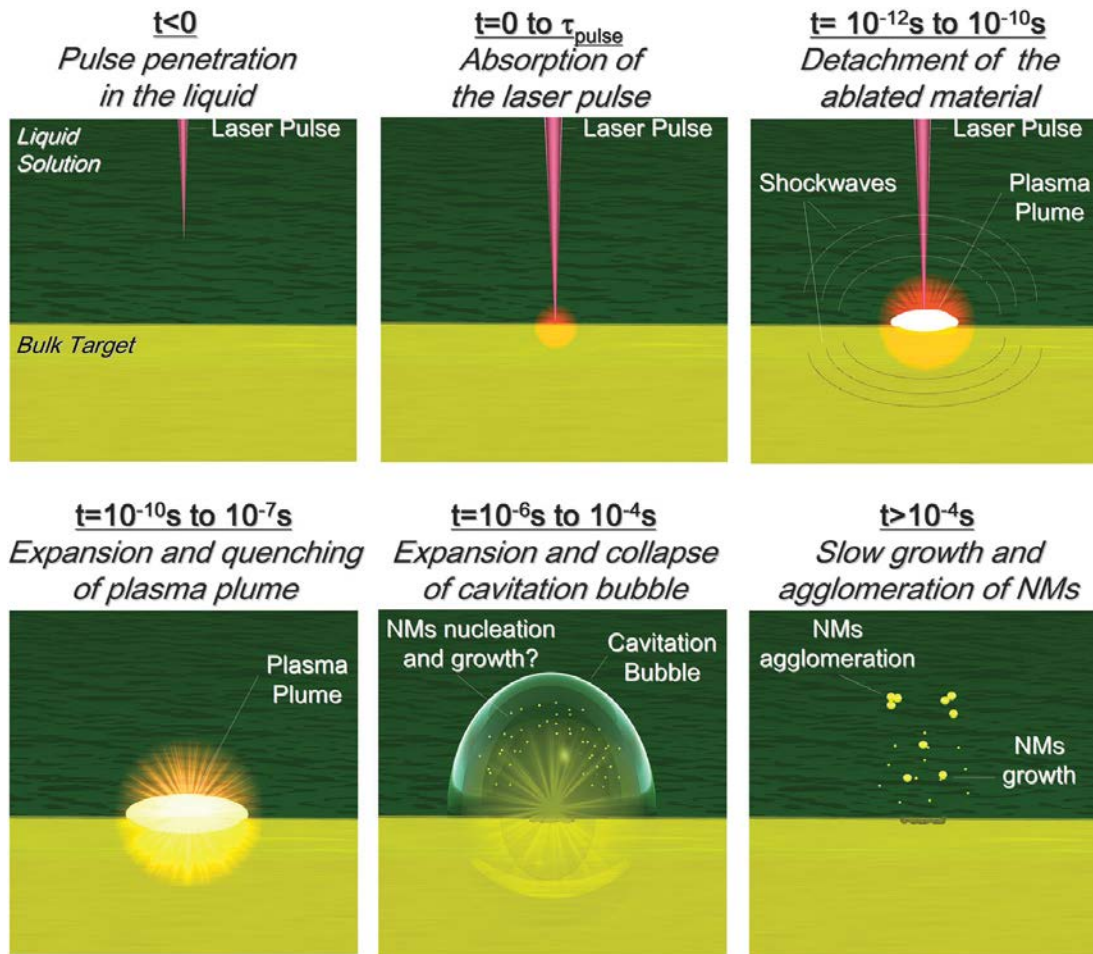
Figure 10: timeline of LASiS where the nucleation and growth of NMs are hypothesized in the 10^{-6} - 10^{-4} time ranges [15]

The amount of material to be investigated is very small which is practically unreadable of investigation techniques. In addition, there is the problem of light emission from the plasma plume, which interferes with laser beam and with optical absorption spectroscopic techniques. So far, the only techniques used to laser ablation process and real time nanoparticles formation are listed below:

- Time resolved optical emission spectroscopy; used for diagnostics of plasma with sub-ns time resolution and sub-millimetric spatial resolution.
- Time resolved ns-shadowgraphy; used for information on the time evolution of the plasma plume, of the shockwaves and of the cavitation bubbles with a micrometric spatial resolution.
- Photoacoustic spectroscopy; used for information on the time evolution of shockwaves with a time resolution of the order of 10^{-6} s.
- Optical absorption spectroscopy; performed with sub ns time resolution.
- Dynamic light scattering; used for information on the presence of objects with a size of a few nm or larger (but not discriminate between and NPs bubbles) with a time resolution of minutes and a spatial resolution of the order of 10^{-3} m.

Currently, time resolved X-ray techniques have been applied for real time investigation of NMs growth during laser ablation. The X-ray techniques benefit is the ability to select condensed phases

and high atomic weight materials. Many X-ray techniques are ideally exploitable such as wide angle scattering (X-ray diffraction – XRD), small angle scattering (SAXS), absorption (XAS and all its variants). Another problem is that many techniques mentioned so far, yield volume weighted signals. Indeed, a single micrometric particle detached from the target produces more signal than thousands of nanoparticles.

Below will be described the effect of LASiS parameter on composition and structure of NMs. The most important parameter is of course the target material, because different material, as we know, yield different products and show different reactivity under the same experimental conditions [15].

The main laser parameters are:

    Pulse wavelength
    Energy pulse
    Pulse duration
    Spot area
    Repetition rate
    Number of laser pulse

- Pulse wavelength:
  It is appropriate to the choice a laser wavelength that does not interfere with the NPs already formed, in order to avoid the absorption and the interaction of the laser with the nanoparticles, which can lead to modifications during their synthesis. Generally, the typical results are the decrease in average size and the broadening of the size distribution [13] [20] [21]. The target skin depth (i.e. absorption coefficient) depends on pulse wavelength; in fact, with UV radiation absorption coefficients of solid materials are larger. Shorter wavelengths are uniformly absorbed by interband transitions in metal targets, disintegrating the irradiated area, instead, at the further wavelength, radiation is absorbed by defects and impurities in the metal target that generating on the laser spot area a wrinkled profile. Therefore, the more reactive species are formed by UV radiation, which can generate chemical reactions between solute and solvent, while visible light shows intermediate properties between UV and IR radiations [15].

- Energy pulse:
  The laser beam energy affects mainly on the amount of material to be removed, in fact, has been studied that increasing the energy, the mechanism of LA does not change while it only increases the production of NPs [22] [23] [20]. Larger size distributions, larger average NPs size and so larger amount of ablated material are observed when the pulse energy is increased. It was observed that increasing the energy of the laser pulse, several mechanisms are possible simultaneously, like fragmentation (is more probable in the central part of the laser spot), phase explosion, boiling and vaporization (that are more probable on the edge of the crater).

- Pulse duration:

As already discussed in the previous paragraphs, the duration of the laser pulse (τ_{pulse}) has a very important effect on size distribution of nanoparticles. Increasing pulse duration and using the same fluence are preferred thermal mechanism of ablation, while mechanism of photoionization are less frequent [15]. In figure 11 we can appreciate the footprint of the laser pulse on a metal, either in gas and in liquid.
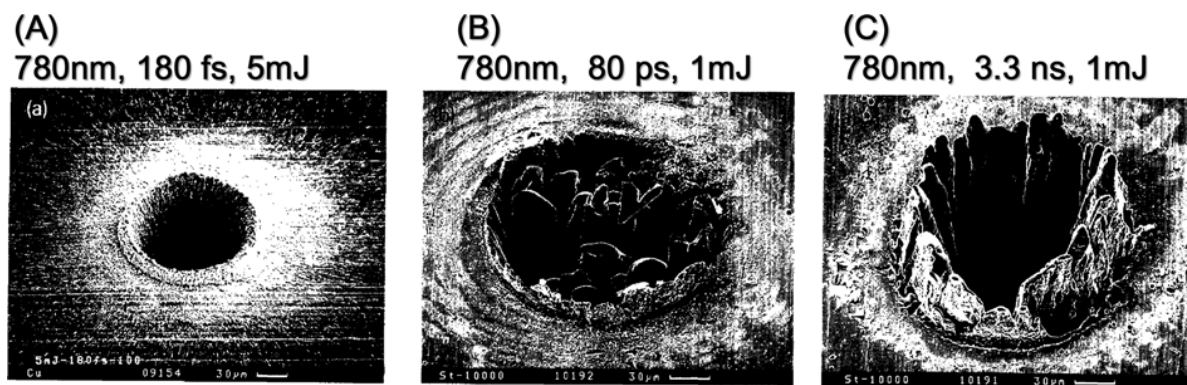

Figure 11: footprint on metal targets in gas with fs (A), ps (B) and ns (C) laser pulses [15].

Figure 11(A) shows the crater generated by fs laser pulse in gas. The figures show the occurrence of thermal ablation processes and the crater is typical of ultrafast localized heating, dominated by direct photoionization processes. At longer times, as in Figure 11 (B and C), pulses of ps or longer generate craters with less sharp shape. Very typical of the simultaneity of direct photoionization and thermal ablation processes like vaporization, boiling and ejection of melted material due to the high pressure generated in the crater.

Pulse duration, in this case, is comparable to the electron–lattice thermalization speed and the area outside of the crater can heat while the laser pulse is in action. In the case of ns laser pulses, laser pulse and ablated material coexist. In this time fraction, laser transfers energy to laser plume due to the laser shielding which causes increase in temperature and further vaporization of the melted drops just ejected from the surface.

It was observed that the NMs size distribution, obtained with ns laser pulses, is sharper than those products with ps and fs laser pulses.

With microseconds, milliseconds and nanoseconds laser pulses, the main mechanism is thermal ablation because the removal of material takes place by vaporization and boiling generating three types of reactions may take place:

A vapour phase reactions between vapours of the target and of the solution, a liquid phase reactions between melted droplets from the target and the liquid solution and a solid phase reactions between solidified drops from the target and the liquid solution [15].

- Spot area:

The studies carried out so far, it can be said that, by increasing the spot area of the laser and maintaining a constant fluence, increases the concentration of ablated material.

A larger area corresponds to a larger average size and the size distribution of the NP. More energy is supplied to the target by increasing the area of the spot, a greater amount of

material is ablated and the concentration of the target species in the plasma plume is greater, consequently obtaining nanoparticles larger.

- Repetition rate:
  The time interval (Δt_p) between two consecutive laser pulses is defined repetition rate. Higher repetition rate corresponding to smaller Δt, then it can be said that the production of NPs for unit time increase with the repetition rate. There was a linear increase only for Δt_p longer than the lifetime of the cavitation bubble, which is of the order of $10^{-4} - 10^{-3}$s and corresponds to repetition rate lower which is of the order of $10^3 - 10^4$ Hz. The cavitation bubble has a discontinuity of refractive index at the liquid/gas interface, which causes scattering of laser light and reduces the laser energy reaching the target. Laser ablation of the target, during the expansion of the cavitation bubble, takes place in a low density hot gaseous phase (comparable to the case of laser ablation in gas). Furthermore, it has been studied that the confinement of the plasma plume on the crater causes a less efficient and the plasma etching on the target decreases. For high repetition rate, these effects are limiting factors (this can be considered the simplest plan to increase LASiS production). If the repetition rate increases, consequently increases the concentration of NPs near the crater since the time for NP diffusion from the ablated region decreases. This effect can promote the coalescence and aggregation of NPs, but in the same way, the scattering of incoming laser pulses and the following reduction in the ablation product. Furthermore, the average temperature of the crater is sensibly higher than room temperature for repetition rates of the order of kHz, in addition, the fraction of matter that reaches the energy threshold irradiation is larger and, compared to LASiS at room temperature, the ablation yield is improved.

- Number of laser pulse:
  The number of laser pulse is relative to ablation time; therefore, the number of laser pulses is proportional to the quantity of ablated material. However, increasing the number of laser pulses, the ablation product can modify. Molecules in solution, during LA, can interact with the target bulk, which can modify the chemical composition (also in inert materials). This is caused by detachment of material by bulk, high temperature and high pressure in proximity of the crater during LA. For instance, in the case of alloys, the chemical composition can change because the crater on target becomes richer in the element with the highest heat of vaporization. Therefore, the contribution of the number of laser pulses, drastically affects the composition of NPs.
  Obviously if the target surface undergoes morphological changes can affect the absorption properties of the material itself with consequent change in the ablation yield and of the ablation process. For example, if the target surface is polished, its reflectivity is increased and the absorbed energy is lower. Instead, if a rough surface absorbs more light entail consequent inhomogeneity in the shape of the detached material [15].

After describing the laser parameters, we describe the material parameters, namely solutes and solvents.

- Solutes:

  As previously explained, solutes can modify chemical-physical proprieties of solution (viscosity, density and surface tension of solvent) and interact directly with NPs. The increase of density and viscosity in solution improves the confinement of the plasma plume on crater and the ablation efficiency. When NMs concentration is very high, during LA, bubbles can form hollow microspheres. Few studies on this topic have been made yet but we can say that the effects due to the solute–NP interactions veil the effect of the modification of physical–chemical properties of the solution. Moreover, if solutes establish chemical bonds with NPs there is limitation of NPs growth, in fact, the size of gold NPs can be reduced from 20 nm in pure water to 5-2 nm in millimolar thiol solution [15]. Several interactions between solute and NPs are observed in several cases.

  To improve the colloidal system must control the growth of NPs. This can happen, for example, by introducing NaCl into the solution. The ion Cl^- has the ability to bind to AuNPs, increasing the repulsion between NPs.

  Therefore, the growth of NPs stops when it is prevented the formation of chemical bonds between the NPs. Similar effects have been seen in other cases; for example by adding surfactants in solution or by lowering the pH of the solution. We can affirm that the reactions that occur between the ablated material and the solute happen during and after the detachment of material from the target, in proximity of the crater and NPs can act as nucleation sites due to a temperature higher than that room [15].

- Solvent:

  It was seen that growing nanomaterials in LASiS, in different solutions and without changing the parameters of the laser, the result changes. This study was conducted to understand the origin of colloidal stability. It is appropriate to state that the solvent greatly influence the composition and structure of the NPs [15]. In the figure 12, are shown growths of different metals to vary the solvent.

  In *Gold* NPs, laser ablation in organic solutions show that the average size is lower and the fraction of non-spherical and aggregated nanoparticles is larger than in H_2O and coagulation and precipitation is observed on the medium long term. It was observed that the greater stability of AuNPs occurs in H_2O. The decrease in average NPs size can be due to a lower ablation efficacy. This is due because the density of Au atoms removed from the surface of gold is lower, or to the capping effect originated by organic solvents, which hinder coalescence of nuclei. It was also observed that the laser ablation could degrade the solvent itself. An example is the formation of enolates and amorphous carbon in acetone. In fact, it is likely that degraded solvent molecules in the ablation region absorb on AuNPs and they act as inhibitors of growth. AuNPs in toluene is the most apparent example of the capping action of by-products generated by solvent degradation, in fact in figure 12, we can see that the Au NPs is enveloped in a graphitic matrix (due to toluene pyrolysis).
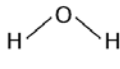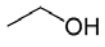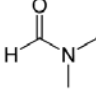
Figure 12: summary table of metal NPs obtained in different solvents with 9 ns pulses at 1064 nm 10 J/cm²
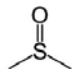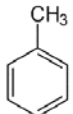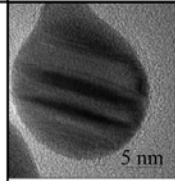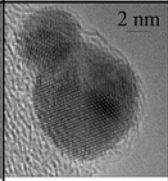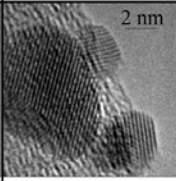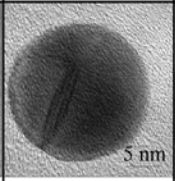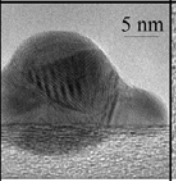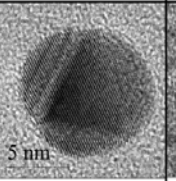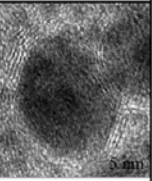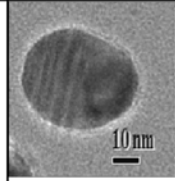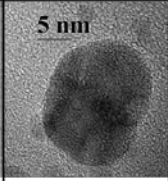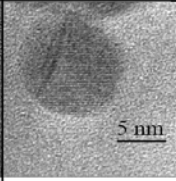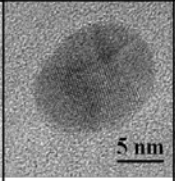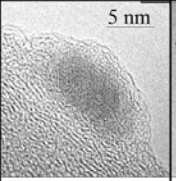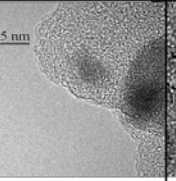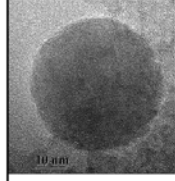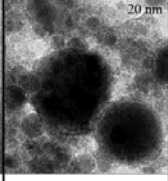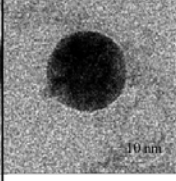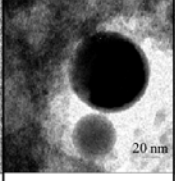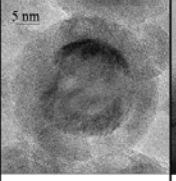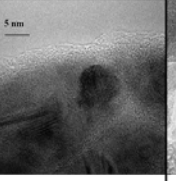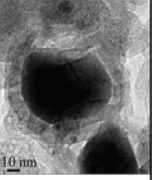
Silver is a noble metals with similar features to gold. Gold has a standard reduction potential of 1.69 eV, while silver 0.80 eV. It was observed that the formation of AgNPs in H_2O yields a thin passivating layer of Ag_2O. When AgNPs is performed in ethanol, acetonitrile and dimethylformamide, the results are similar to those of Au, in fact the dimension of particles are smaller than H_2O. Even for silver nanoparticles is observed an amorphous coating. Since silver has a higher tendency to oxidation, it is possible that the concentration of oxidative species in the plasma plume is lower during ablation of Ag than of Au, because part of silver atoms binds to oxygen atoms.

Iron provides further insight into the effect of solvents on LASiS, due to its low reduction potential compared to gold and silver. In addition, reacts with C giving carbides, with O giving various oxides and with H_2O it can give crystalline and amorphous hydroxides. Local temperature and pressure influence the composition of the final product. It also depends on the concentration of the solution and molecules ablated material. It was observed that two distinct populations of NMs (carbides and oxides) suggests that different formation ways are required at different locations or at different times during LASiS. Iron oxide NPs are smaller than carbide NPs, signifying that they are formed at longer times, when the temperature and the iron concentration are lower, and they can result from the reaction of iron with dissolved O_2 or O atoms from the ethanol molecules. In opposition, iron carbide NPs form only at low oxygen concentration and in the presence of pyrolysed ethanol molecules, which requires high temperature. As discussed about laser ablation of gold and silver, pyrolysis of

organic solvents generates different by products with different chemical and physical properties like, for instance, alcoholates from ethanol and graphite from toluene. In addition to describing, how varied the growth of NPs in different solvents is appropriate to describe mainly the optical properties of a NP. In the next section will describe what are the physical origins and consequently the optical properties at the nanoscopic scale of NPs.

1.2.2.   Physical origin and optical properties of metallic NPs

The physical properties and the optical response of a metal nanoparticle, differ significantly from those that can be observed on a bulk material. They are placed into an intermediate stage between those of the solid and those of the molecule. The effects of size reduction (quantization effect) on the electronic properties appear when the size of the nanoparticle become comparable, or lower, to the mean free path of the quasi-free electrons within the metal. From a classical point of view, we can affirm that if a target is small, collisions between electrons and the surface can no longer be neglected compared to other processes of interaction (electron-electron collisions and electron-phonon collisions). The response of the quasi-free electrons is modified by the interaction with the surface and the subsequent collapse of the periodicity of the system.

The density of electronic states remains almost unchanged for dimensions larger than 3 nm. Consequently, the interband absorption (and the dielectric constant associated with it) varies little, except that size is very small. However, after the collisions, we observe a sharp increase in the contribution of ε interband. In the case of noble metals, the properties that result from this greater interaction with the interfaces can be associated with a purely classical effect: it speaks of dielectric confinement. This effect gives rise to a resonance in the absorption spectrum of such materials when their dimensions become very small compared to the wavelength of the incident electromagnetic field. Quantum effects may be ignored up to dimensions on the nanometric scale.

1.2.3.   Interaction of an electromagnetic wave with a NP

When an object, such as a single atom, a molecule or a solid particle or liquid, is illuminated by an electromagnetic wave, the electric charges in its interior are forced to oscillate due to the electric field of the incident wave. When an accelerated electric charge it radiates electromagnetic energy, we will have a secondary radiation emitted from the obstacle in all directions, with the same wavelength of the incident field: i.e. scattered radiation. Furthermore, the excited elementary charges can transform part of the electromagnetic energy incident in other forms (such as into

thermal energy): to this dissipation of energy within the particle corresponds to the absorption. The presence of the particle results in an extinction of the incident ray.

This extinction, being due to the absorption and diffusion, thus depends on the chemical composition, shape, orientation of the particle, from the surrounding medium and the frequency of the incident beam.

If we consider a plane monochromatic electromagnetic wave incident on a medium, it will induce a polarization in the medium that characterizes its optical response. If instead, consider a set of non-magnetic NPs, which are located in a vacuum (free particles) which interact with the electromagnetic wave, and assuming some parameters, such as the degree of dilution to treat NPs as independent and also consider NPs larger than 2 nm, the optical response can be calculated in a quasi-static approximation (or dipole). According to the studies conducted so far, we can say that for small particles, optical extinction is only due to their absorption [15].

When the size of the particle increases (>2 nm), the dipole approximation falls and multipole effects come into play [24].

This results in a strong increase in the scattering, which grows to dominate absorption. In this case, the interaction between the electromagnetic wave and the NPs can be treated only the Mie theory. Below will be described the resonance of the surface plasmon.

From a classical point of view, the plasmon resonance may be associated with resonant excitation, induced by external electromagnetic field, of collective oscillation of electrons (both conduction electrons that bound electrons of the bands deep) inside a sphere metal. The oscillating charge over the surface of the particle generates an electric dipole field, which increases the electric field felt by the particle (field that is considerably enhanced in resonance conditions). Such oscillation can be likened to that of an electron gas in a massive system, however modified in this case by the presence of interfaces. Hence the name of resonance plasmon of surface.

1.2.4. Study of a single metal particle: Mie theory

When the size of the nanoparticles analysed exceed tens of nanometers, the spread of a wave incident is no longer negligible compared to its absorption and extinction appears to be the sum of both contributions. In this case it is necessary to consider the higher order multipoles, the quasi-static approximation is no longer valid. The first to address the problem with success was Gustav Mie, in an attempt to understand the origin of the scattered and absorbed colours by a solution of colloidal gold particles dispersed in water.

The solution of Mie, despite being obtained to the diffraction from a single sphere, can also be applied to diffraction by any number of spheres. However, it is necessary to impose certain restrictions: the diameter and the composition of the balls must be uniform, the balls must be randomly distributed and must be separated from each other by distances much greater than the incident wavelength.

Under these conditions, the total scattered energy by the system is equal to the scattered energy from a single sphere, multiplied by the total number of spheres.

Thanks to this generalization, the Mie solution finds application in many areas (study of the optical properties of metal suspensions, atmospheric dusts and interstellar particles, the theory of the rainbow and the effects clouds and fog on the transmission of light). The solution of Mie describes the scattered wave by the metal particle as a linear superposition of spherical waves, each generated by an electric multipole and is obtained as exact solution of Maxwell equation for a particle in electromagnetic field.

Extinction section effective of the particle can be written:

For particles larger than a few tens of manometers, the spectra of extinction, diffusion and absorption can be calculated explicitly implementing the following equation:

$$\sigma_{ext} = \frac{2\pi}{n_m^2 k_0^2} \sum_{l=1}^{\infty} (2l + 1)\, Re\,\{a_l + b_l\}$$

Figure 13 shows schematically the inhomogeneous polarization in a particle larger than the incident wavelength and the subsequent appearance of the quadrupole.
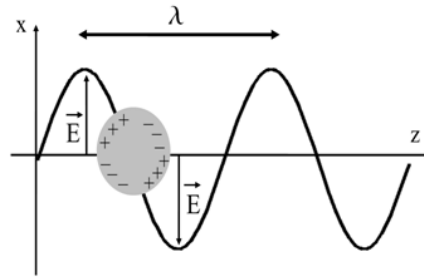
Figure 13: inhomogeneous polarization and appearance of the quadrupole

In dipolar approximation, i.e. for diameters between a few nanometers and a few tens of nanometers, the size of the nanoparticles have a weak impact on the resonance frequency of the surface plasmon, which can be considered independent of the size of the object. It can only detect a slight blue-shift of the particles resonance of diameter less than 2 nm, due to quantum effects (that we have not examined). Dependence on the size of absorption effective section of the peak is very strong, linked by a relationship of proportionality to the volume.

Has been studied that, for nanoparticles larger than 20-30 nm, the experimental results are comparable from the theoretical ones. Above these values, therefore, the quasi-static approximation can no longer be applied.

In the case in which resorts to the Mie theory (D> 30 - 50nm), the spectral profiles appear shifted toward the red, and it assists to the appearance of multipole resonances.

The physical origin of the resonance of the surface plasmon is the same for all metals. Nevertheless, by some interesting differences appear in the spectra varying the composition of the material.

The resonance frequency of the surface plasmon of a metal depends also from the surrounding environment through the dielectric constant.

So far, in addition, we have always understood that the NPs are perfectly spherical particles. However, the shape of the nanoparticles often deviates from a perfect nanosfera and it is to be considered the generalization compared to the case of spherical particles is formed by nanoellipsoids: these particles is the appearance of effects related to the polarization of light.

The resonance frequency of the surface plasmon, to a particular polarization, is determined, even in this case, to the dielectric constant of the particle and that of the matrix.

In figure 14 it is possible to see how different the resonance peak of the absorption spectrum of spheroidal nanoparticles of silver, incorporated into a matrix of SiO_2, to vary of their shape.
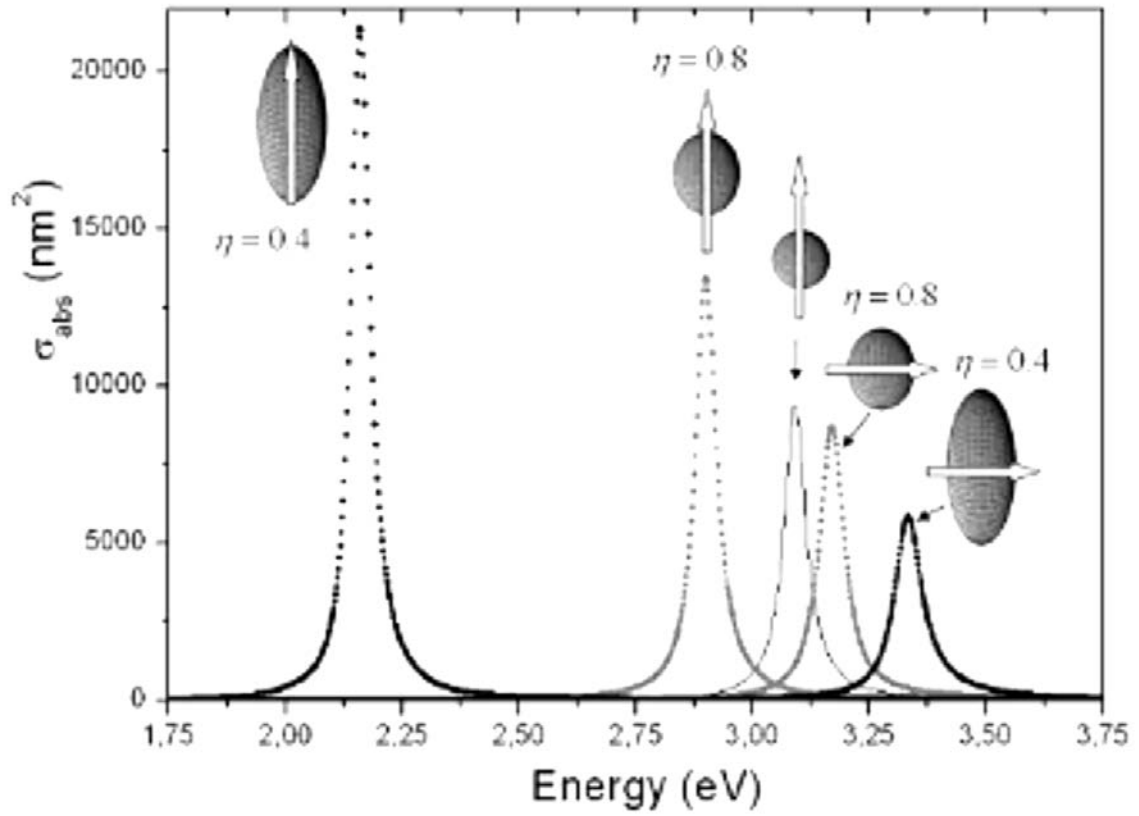
Figure 14: variation of the resonance peak to vary the shape of the AgNPS.

2.   Diagnostic techniques and experimental setup

This chapter describes all the diagnostic techniques used in this thesis. The techniques will be described from a theoretical point of view, besides the description of the experimental setup.

For ease of reference, the various techniques are described in typology order.

Morphological Analysis

2.1.   Atomic Force Microscope – AFM

The scanning tunnelling microscopy (STM) has previously become a useful tool in surface science because its ability to characterize surfaces of metals and semiconductors in real space on an atomic scale. However, one limitations of STM is the necessity of sample conductivity. The atomic force microscope (AFM) instead, is a synthesis of the mechanical profilometer, using mechanical springs to sense forces, and the STM, using piezoelectric transducers for scanning [25].

An AFM is a deceptively simple instrument that requires a considerable amount of engineering construct such that the AFM is capable of measuring images with nanometer resolution. The basic components of an AFM are a computer, control electronics, and a stage. They are showed in figure 14.
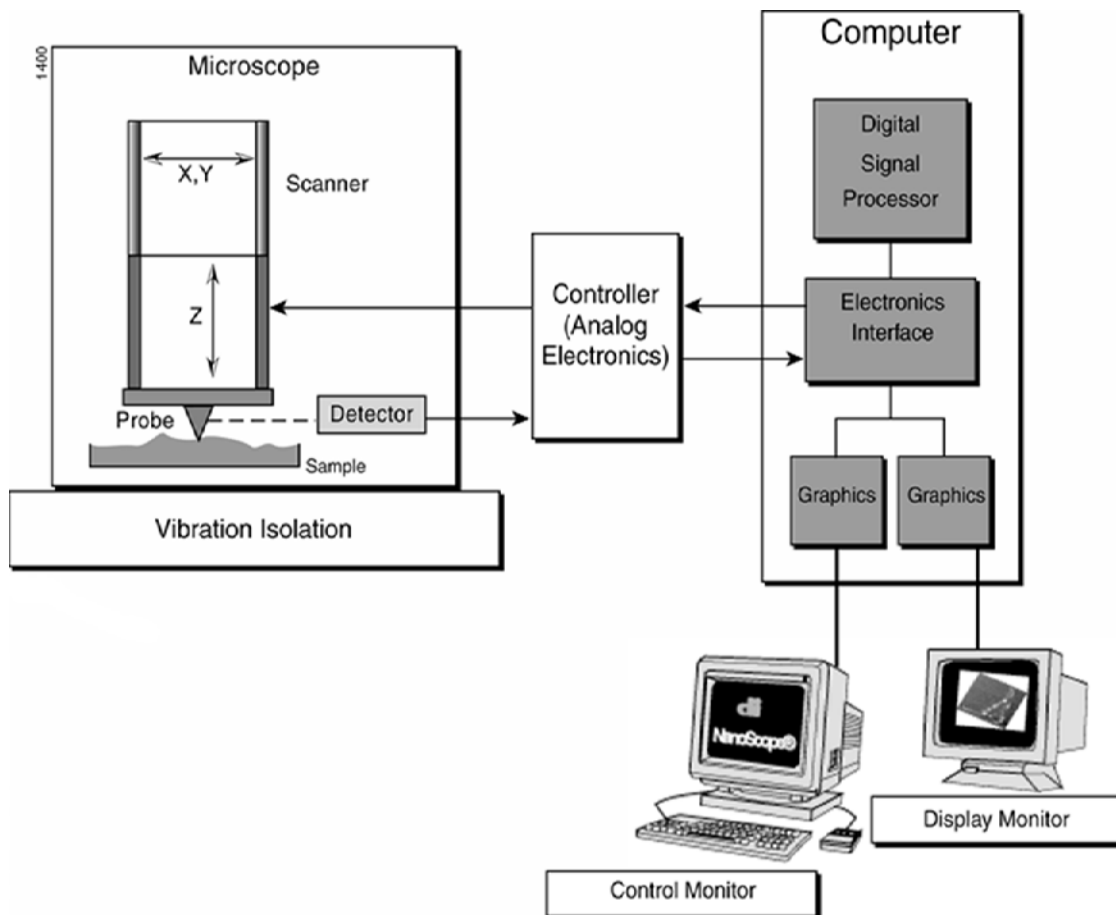
Figure 15: AFM components

The electronics control generate the electronic signals required for moving stage components such as the Z motors and the XYZ scanner. The control electronics also digitize the images measured in the stage so that the computer can display them. Software in the computer is used for acquiring and displaying AFM images. In addition, software for processing and analyzing AFM images typically resides in the computer. Typically, the AFM stage includes an AFM scanner and a CCD camera, along with motion control systems for moving the scanner relative to a sample in the X-Y-Z axis.

Often the electronics are separated from the stage because fans used to cool the electronics cause unwanted vibrations in the stage which reduce the resolution of the AFM [26]. Nowadays, commercial AFM's can be applied with an efficiency comparable to electron microscopes. Samples are measured without special surface preparation at ambient pressure or in liquids. The instrument characterizes the morphology of the samples with quantitative information about properties such as roughness or height distributions.

The forces that come into play can be two: Contact and non-contact mode.

If the microscope is operated in non-contact mode at tip-sample separations of 10 to 100 nm, forces (van der Waals, electrostatic, magnetic or capillary) can be identified and give information about surface topography, distributions of charges, magnetic domain wall structure and liquid film distribution. The probing tip, at separations of the order of Å, is in contact with the sample. In this mode, ionic repulsion forces allow the surface topography to be traced with high resolution. It can

get, under best conditions, until atomic resolution. In addition, frictional forces and elastic or plastic deformations can be detected under appropriate conditions [25].

The Atomic Force Microscope used for measurements is the *Dimension Icon* of the *Bruker*.

The Dimension® Icon™ Scanning Probe Microscope (SPM), shown in Figure 16, produces high resolution, three-dimensional images by scanning a sharp tip over the sample surface. The tip is part of a flexible cantilever mounted on one end of a cylindrical piezoelectric tube mounted near the top of the microscope. Voltages applied to the X and Y electrodes on the piezoelectric tube deflect the tube horizontally to produce a precise raster scan over the sample surface. A voltage applied to the Z electrodes on the piezo tube controls the vertical height of the tip. The Dimension Icon head includes X, Y and Z position sensors. The sensed XYZ position information provides the feedback for closed loop control of probe tip location, ensuring that the probe completes each move command at the intended position. Stepper motors coupled to lead screws translate slides with the sample attached. A separate motor drive controls the height of the microscope and tip relative to the sample surface [27].

Figure 16: Dimension Icon SPM System

In AFM, the probing tip is attached to a cantilever-type spring. In response to the force between tip and sample the cantilever, is deflected.

Images are taken by scanning the sample relative to the probing tip and digitizing the deflection of the lever or the z-movement of the piezo as a function of the lateral position x, y.

An SPM probe is comprised of a tip affixed to a cantilever mounted on a substrate, which is inserted in a probe holder.

The Dimension Icon's motorized Z-stage provides accurate, automatic tip engagement and approach. The rigidity of the Z-stage permits low noise and high accuracy imaging with the instrument. A motorized lead screw for coarse approach of the head drives the Z-stage to the sample. This configuration permits samples of different thicknesses to be imaged with little difficulty. The Dimension Stage Controller integrates the illuminator control, power supply, and air and vacuum pumps. The optical microscope includes a computer-controlled illuminator for easier optical focusing and zooming. Video image capture capability allows the user to easily incorporate video images into reports and publications.

The Dimension Icon SPM control station consists of four components: input and display devices (keyboard, trackball, mouse and monitors), computer, NanoScope V controller and Dimension Stage controller. Input and display devices include a large monitor (Dimension Icon), keyboard, mouse, and trackball. These devices convey information signals to the computer to operate the software and SPM. The NanoScope V Controller, controls the microscope head and scanning. The Dimension Icon NanoScope V controller is controlled via a 68-pin micro-SCSI cable connection between the rear of the controller and the computer while the Icon-PI Controller is controlled via a USB 2 cable.

The Dimension Stage Controller, controls the vacuum and air supply and optics illumination. The Dimension Stage Controller is controlled via a serial cable connection between it and the computer. The Dimension Stage Controller features gauges on the front panel to indicate vacuum and positive pressures. The Dimension Stage Controller channels positive pressure to the underside of the chuck during X-Y movements, allowing the chuck to glide smoothly over the granite. The Dimension Stage Controller drives the motors of the Z-stage, focuses, zooms and powers the video camera. The Dimension Stage Controller incorporates status LEDs, on the upper right front panel. The Dimension Icon Microscope Electronics Box, located below the microscope, switches between the different operating modes, amplifies and combines signals from the photodiodes as appropriate.

The optics system assists you in locating the cantilever and tip relative to the sample. The NanoScope software uses this information to engage the tip on the sample surface at the desired location. The system automatically focuses on most samples by adjusting the SPM height; however, the trackball is available for manual focus control.

The Dimension SPM head provides accurate imaging of a stationary sample while scanning the integrated detector-probe assembly above the sample. It is shown in figure 17. The Dimension SPM head allows optical correction of the laser beam path to track the movement of the probe while scanning under the fixed laser beam assembly. The Dimension SPM head is effective in imaging samples too large or heavy to scan by movement of the sample.

The Dimension SPM head places a corrective, tracking lens within the scanner tube to stabilize the laser beam focal point atop the scanning cantilever. This patented technology sharply reduces bowing and attenuation artifacts due to cantilever scanning across the laser beam's otherwise stationary focal plane.

The Dimension SPM head scans the tip and generates the cantilever deflection or probe feedback signal for the different imaging modes. A quad photodetector detects the beam emitted by the laser diode (1.0 mW max at 670nm) as it reflects off the cantilever. The integrated scanner head consists of the following subassemblies.

The preamp board is located inside the Dimension SPM microscope head. The preamp board contains a preamplifier circuit for both photodetector signals, a laser diode power supply circuit that regulates the output of the laser and a sensor preamplifier. The head is connected to a 48-pin male connector cable plugged into the socket on the front right of the Dimension Icon microscope.
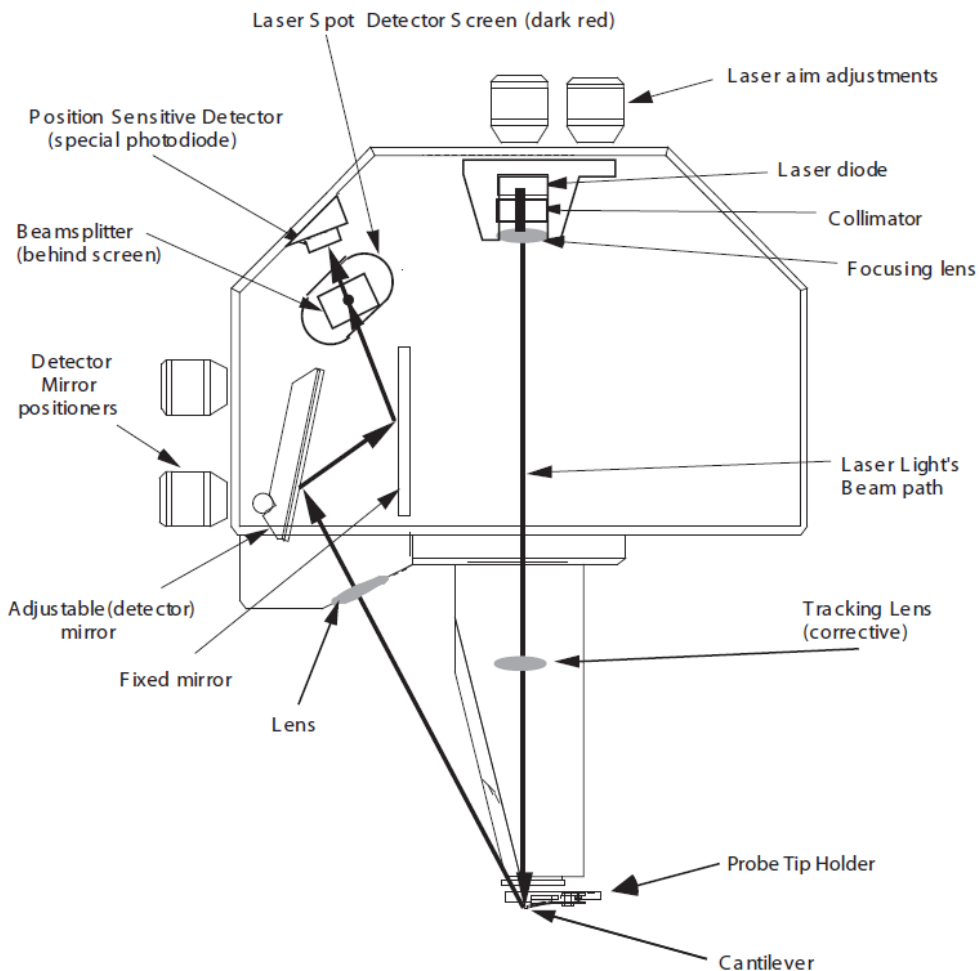
Figure 17: Dimension SPM Head

A kinematic tilt stage positions the laser beam on the cantilever. The tilt stage consists of the laser diode, collimator, focusing lens, base plate, and the X and Y laser diode adjustment knobs. The X laser diode adjustment knob moves the beam parallel to the major axis of the cantilever substrate.

The Y laser diode adjustment knob moves the beam perpendicular to the major axis of the cantilever substrate. An adjustable mirror positions the reflected laser spot relative to the four photodetector elements using a kinematic mount and the photodetector mirror adjustment knobs. The photodetector mirror adjustment knobs assist the user in adjusting the position of the mirror to maximize the SUM signal and set the deflection signals.

The four elements of the quad photodetector combine to provide different information depending on the operating mode. In all modes, the four elements combine to form the SUM signal. The amplified differential signal between the top two elements and the two bottom elements provides a measure of the deflection of the cantilever. This differential signal is used in Contact and TappingMode. Similarly, the amplified differential signal between the sum of the two left photodiodes and the sum of the two right photodiodes provides a measure of the torsion in the cantilever.

The beamsplitter diverts some of the laser light directed towards the photodetector toward the Laser Spot Detector Screen. This screen provides visual indication of the condition of the reflected spot and its position relative to the photodetector.

The cantilever holder is a small printed circuit card or acrylic block that holds the cantilever firmly at the proper angle. The standard cantilever holder is used for operation in air, while a cantilever holder with a clear glass window is used for fluid cell operations. Cantilever holders include the cantilever piezoelectric stack and the electrical contacts to the drive circuits. Cantilever holders include gold-plated spring sockets which mate with the gold-plated pins at the end of the scanner. The standard cantilever holder shown in figure 18 contains a piezoelectric stack to oscillate the cantilever when operating in TappingMode. The same cantilever holder is used for Contact AFM but no voltage is applied to the piezo stack.
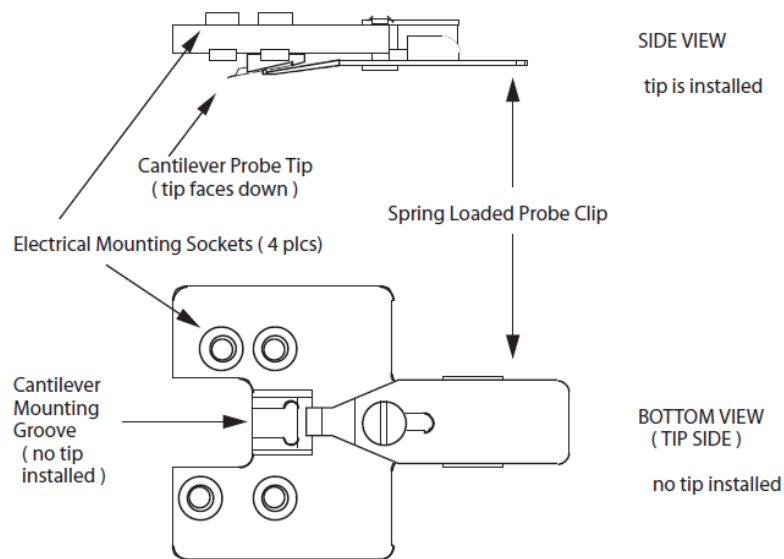
Figure 18: Standard Cantilever Holder

The Dimension Icon SPM can be used for several applications. Generally, the types of analysis mostly used are:

1. ScanAssist
2. TappingMode
3. ContactMode

1. ScanAsyst™ is the world's first imaging mode with automatic image optimization technology for atomic force microscopy (AFM). This innovation operates automatically and simultaneously, adjusting scan parameters, such as setpoint, feedback gains, and scan rate. Intelligent algorithms continuously monitor image quality to make appropriate parameter adjustments. This makes imaging as easy as simply selecting a scan area and scan size for almost any sample in either air or fluid.
2. TappingMode AFM operates by scanning a tip attached to the end of an oscillating cantilever across the sample surface. The cantilever is oscillated at or slightly below its resonance frequency with an amplitude ranging typically from 20nm to 100nm. The tip lightly "taps" on the sample surface during scanning, contacting the surface at the bottom of its swing. The feedback loop maintains a constant oscillation amplitude by maintaining a constant RMS of the oscillation signal acquired by the split photodiode detector. The vertical position of the scanner at each (x,y) data point in order to maintain a constant "setpoint" amplitude is stored by the computer to form the topographic image of the

sample surface. By maintaining a constant oscillation amplitude, a constant tip-sample interaction is maintained during imaging. Operation can take place in ambient and liquid environments. In liquid, the oscillation need not be at the cantilever resonance. When imaging in air, the typical amplitude of the oscillation allows the tip to contact the surface through the adsorbed fluid layer without getting stuck. The problem of having high-lateral forces (as the case for contact mode) between the cantilever and surface very high lateral resolution can be solved by having the tip touch the surface only for a short time, thus avoiding the issue of lateral forces and drag across the surface. Drafts of TappingMode are shown in figure 19 and 20.

3. Contact mode AFM operates by scanning a tip attached to the end of a cantilever across the sample surface while monitoring the change in cantilever deflection with a split photodiode detector. The tip contacts the surface through the adsorbed fluid layer on the sample surface.

A feedback loop maintains a constant deflection between the cantilever and the sample by vertically moving the scanner at each (x,y) data point to maintain a "setpoint" deflection. By maintaining a constant cantilever deflection, the force between the tip and the sample remains constant. An example of ContactMode feedback loop are shown in figure 21 [27].

In this thesis have been used only the first two types of analysis; ScanAsyst and TappingMode.
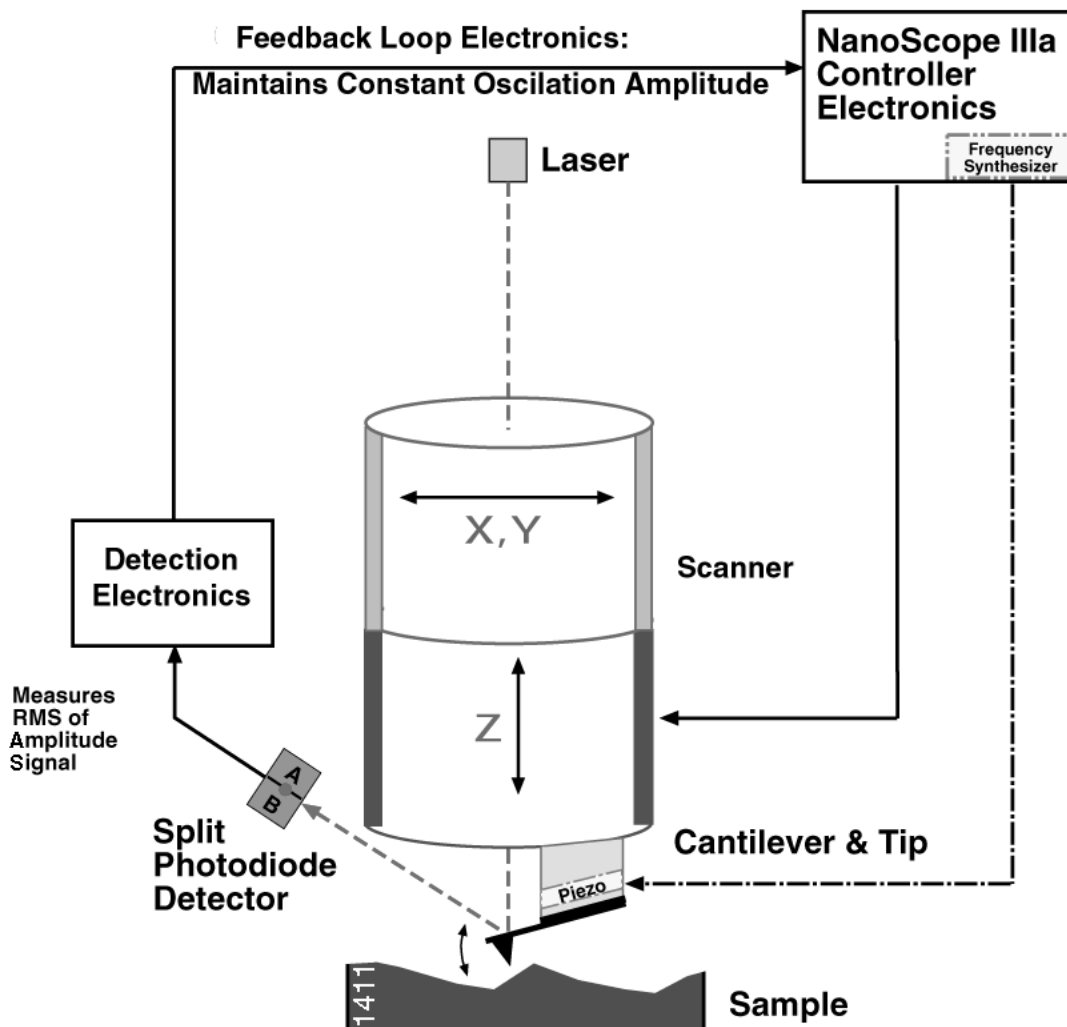
Figure 19: Feedback Loop Electronics
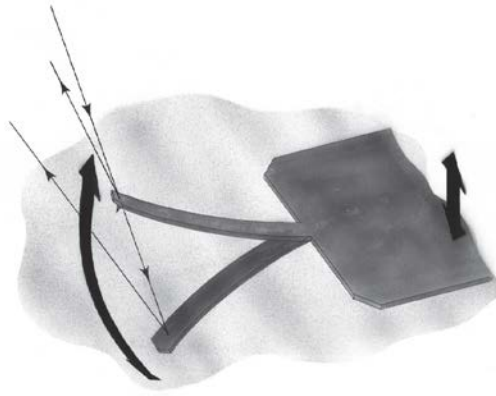
Figure 20: this picture depicts a cantilever oscillating in free air at its resonant frequency. A piezo stack excites the cantilever substrate vertically, causing the cantilever to move up and down. As the cantilever moves vertically, the reflected laser beam, or "return signal," deflects in a regular pattern over a photodiode array, generating a sinusoidal, electronic signal.
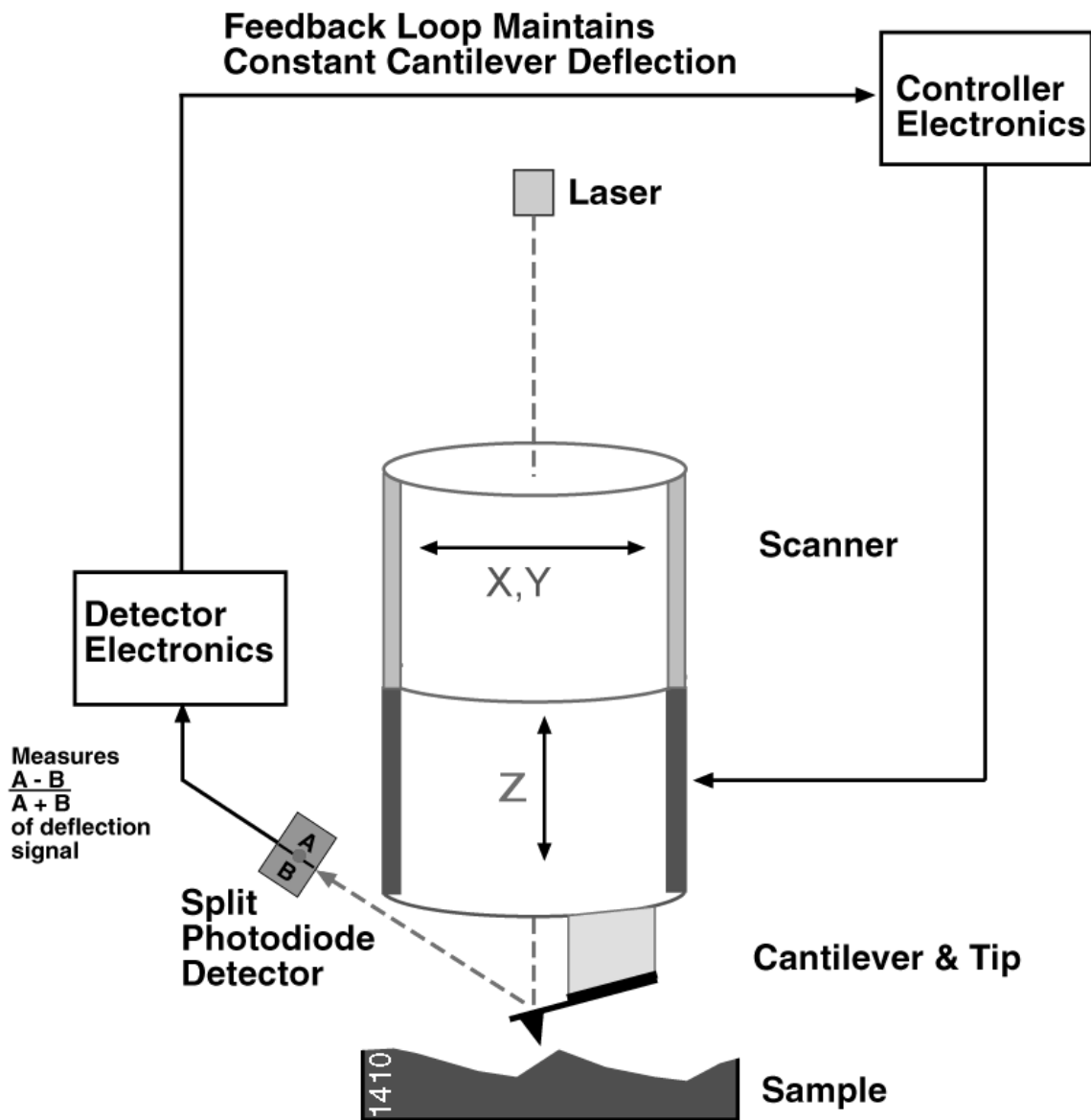
Figure 21: Feedback Loop Maintains Constant Cantilever Deflection

2.2.   Scanning Electron Microscope – SEM-EDX

Energy Dispersive X-ray Analysis (EDX) makes use of the X-ray spectrum emitted by a solid sample bombarded with a focused beam of electrons to obtain a localized chemical analysis. All elements from atomic number 4 (Be) to 92 (U) can be detected in principle, though not all instruments are equipped for 'light' elements (Z < 10). Qualitative analysis involves the identification of the lines in the spectrum and is fairly straightforward owing to the simplicity of X-ray spectra. Quantitative analysis (determination of the concentrations of the elements present) entails measuring line intensities for each element in the sample and for the same elements in calibration Standards of known composition.

By scanning the beam in a television-like raster and displaying the intensity of a selected X-ray line, element distribution images or 'maps' can be produced. Also, images produced by electrons collected from the sample reveal surface topography or mean atomic number differences according to the mode selected. The scanning electron microscope (SEM), which is closely related to the electron probe, is designed primarily for producing electron images, but can also be used for element mapping, and even point analysis, if an X-ray spectrometer is added.

There is thus a considerable overlap in the functions of these instruments.

The experimental setup used for SEM-EDX analysis is a FEI Quanta 200 SEM. The FEI Quanta 200 is variable-pressure scanning electron microscopes (ESEM™), in figure 24. All of which can accommodate multiple sample and imaging requirements for industrial process control labs, materials science labs, life science labs and cultural heritage.

The Quanta SEM systems can be equipped with analytical systems, such as energy dispersive spectrometer, wavelength dispersive x-ray spectroscopy and electron backscatter diffraction. In addition, the field emission gun (FEG) systems contain a S/TEM detector for bright-field and dark-field sample imaging. Another variable that changes amongst the SEM system is the size of the motorized stage (50mm, 100mm, and 150mm) and the motorized z-range (25mm, 60mm, and 65mm, respectively).

Specimens for SEM analysis are often described as "bulk" specimens. They are typically 1-3cm in diameter and often require little or no pre-preparation. Different SEMs have different stage sizes that limit the maximum size of the specimen. Typically, specimens are mounted on stubs that are 1 inch (2.5cm) in diameter. All specimens must be normally a) dry and b) electrically conductive. For metallic specimens this is not normally a problem, however most other specimens are not electrically conductive. Specimens are made electrically conductive by the application of a thin coat of electrically conductive material, usually a metal (Au, Pt, Cr) or carbon. These coatings are usually only a few nanometres thick and do not interfere with the structure of the specimen. Two processes can apply coatings: sputtering and evaporation [28].

Figure 22: FEI Quanta SEM

Three devices essentially constitute the experimental setup for EDX:

- *Electron microprobe*: it is a system for the formation of the beam. it generates electron beams characterized by high density and stability of current and small diameters, adapted to obtain the highest possible resolution.
- *X-ray detection systems*: the detector is made from a single crystal of Si doped with Li, which is transferred to the energy of X photons. The detector allows the realization of a graph, in which certain values of energy correspond peaks. Since every atom has well-defined lines, through the observation of the obtained spectrum can be traced to the elements in the sample.
- *Systems analysis of the X*: the amplified signal from the detector is conveyed in a device called multichannel analyzer (MCA), which acts as an analog-digital converter and sends the signal coming from the amplifier in discrete channels of energy, whose amplitude is usually of 10 or 20 eV. The signals of the X-rays are then distributed according to their energy and you get what is called the spectrum of X-rays the MCA is integrated in a computerized system that allows the display of the obtained spectrum on a monitor. It can also be stored on disk, it can be performed (by means of special software) the procedures for spectrum analysis and management of the obtained results.

Chemical Analysis

2.3.　　　Photoluminescence – CL

The technique of photoluminescence is used for identifying mineralogical phases present on the surface of the materials. It is widely used in the field of cultural heritage; in fact, it identifies the presence of any coatings, "alteration patinas" or extrinsic defects in the material.

Luminescent materials are mostly solid inorganic materials consisting of a host lattice with impurities. The impurity concentrations generally are low in view of the fact that at higher concentrations the efficiency of the luminescence process usually decreases (concentration quenching). The absorption of energy, which is used to excite the luminescence, takes place either by the host lattice or by impurities. In most cases, the emission takes place on the impurity ions, which, when they also generate the desired emission, are called activator ions. When the activator ions show too weak an absorption, a second kind of impurities can be added (sensitizers), which absorb the energy and subsequently transfer the energy to the activators. This process involves transport of energy through the luminescent materials.

Quite frequently, the emission color can be caused by ionic impurity. On the other hand, quite a few activator ions show emission spectra with emission at spectral positions which are hardly influenced by their chemical environment. This is especially true for many of the rare-earth ions.

In the case of luminescence center, the emission is generated on an optical center, in contradiction to, e.g., emission, which results from optical transitions between host lattice band states or from a transition between two centers. Such an optical center can be an ion or a molecular ion complex.

In luminescence phenomenon, the emission could also occur on the ion in a vacuum, i.e. when the optical transition involves electronic states of the ion only. Characteristic luminescence can consist of relatively sharp emission bands (spectral width typically a few nm), but also of broad bands, which can have widths exceeding 50nm in the visible part of the spectrum. Broad emission bands are observed when the character of the chemical bonding in the ground and excited state differs considerably. This is related to a change in equilibrium distance between the emitting ion and its immediate chemical environment and is commonly explained with the configuration coordinate diagram (figure 23).
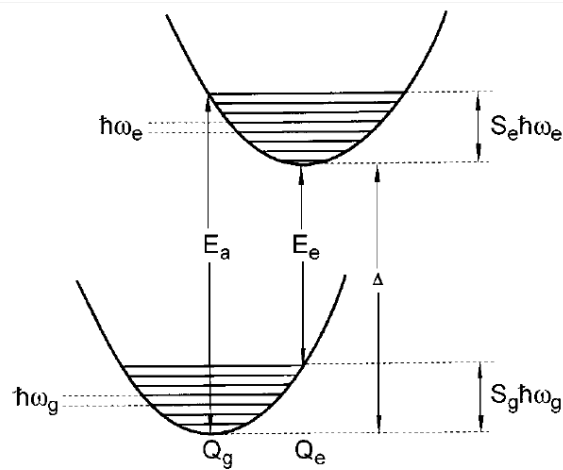
Figure 23: Configurational coordinate diagram

In this diagram, Q_g and Q_e represent the metal-ligand distances in the ground and excited states, respectively. E_a and E_e are the energies at which the absorption and emission bands have their maximum intensity, respectively. Δ is the energy of the so-called zero phonon line; this transition involves completely relaxed excited and ground states, and no excited phonon states are involved – hence the name of this kind of transitions. The phonon frequencies in the ground and excited state are given by $\hbar\omega_g$ and $\hbar\omega_e$, respectively. The relaxation energies in the ground and excited states can be expressed as a product of the phonon energy and the so-called Huang-Rhys factors. The Huang-Rhys factors S_e and S_g in the ground and excited state (being pure numbers), respectively, give the mean number of phonons involved in the absorption and emission processes, respectively. In the harmonic approximation, the curvature of the parabolic band (determined by the bond strength), the phonon frequencies, and the Huang-Rhys factors are the same in the ground and excited state [29].

The obtained spectra reconstruct the trap levels and centers of luminescence due to the intrinsic or extrinsic impurities present in the material, then to the identification of molecules and minerals. Instead of thermoluminescence, this technique provides local information and not the entire sample (the analysis is, in fact, limited to the area hit by the beam of photons). In addition, its sensitivity is very high, and determines the presence of defects up to a level of 0.1 ppm (it is currently used in petrography to establish the purity of the buds).

The setup used consists of a Horiba Jobyn Yvon Olympus microscope mounting objectives 10x, 50x, 100x. The microscope is equipped with a laser source of 378 nm with a power of 12mW for the generation of photo-luminescence, and a spectrometer Triax 320 (Horiba Jobyn Yvon) that works in the range of 200-1500 nm for the processing of the optical signal. The optical detection system is composed of a monochromator in series to a CCD; the monochromator is an instrument with two slits: the first input for the collection of the signal coming from the sample and the second output for the signal transfer to the CCD. The sample was positioned in the housing of the microscope and focused via remote with the 100x objective through a camera connected to a computer. After focusing the sample, due to the optics of the microscope, the sample was sent on a UV laser beam (incidence angle zero), with respect to the normal to the sample. The photoluminescence signal was then collected by the objective 100x (incidence angle zero) and sent through an optical system (including a notch filter that excludes the laser frequencies of departure, to avoid overlap between the input signal and signal output) to an optical fiber that is connected to the entrance slit of the spectrometer. It is possible to see the apparatus used in Figure 24.

Figure 24: photoluminescence setup

The monochromator is constituted by some toroid mirrors that focus the input signal on a turret in which there are housed three different diffraction gratings (each analysed intervals of wavelengths different from 'UV up to the IR spectrum). These mirrors decompose the signal into its components in various wavelengths. The turret is controlled by remote. Via software, we can choice the diffraction grating that best suits the analysis of the coming spectra. The output signal from the tower is collected by another toroidal mirror and sent to the CCD.

The CCD detector is a Si wafer with a resolution of 1024 x 128 pixels that has the task of transforming the incoming optical signal into an electrical signal by photoelectric effect, so that it is interpretable by appropriate software.

2.4. X-ray Fluorescence Spectroscopy – XRF

When a primary x-ray excitation source from an x-ray tube or a radioactive source strikes a sample, the x-ray can either be absorbed by the atom or scattered through the material. The process in which an x ray is absorbed by the atom by transferring all of its energy to an innermost electron is called the "photoelectric effect." During this process, if the primary x-ray had sufficient energy, electrons are ejected from the inner shells, creating vacancies. These vacancies present an unstable condition for the atom.

As the atom returns to its stable condition, electrons from the outer shells are transferred to the inner shells and in the process, giving off a characteristic x-ray whose energy is the difference between the two binding energies of the corresponding shells. The emitted x-rays produced from this process are called "X-ray Fluorescence," or XRF. The process of detecting and analyzing the

emitted x-rays is called "Xray Fluorescence Analysis." In most cases, the innermost K and L shells are involved in XRF detection.

A typical x-ray spectrum from an irradiated sample will display multiple peaks of different intensities (Fig. 25).
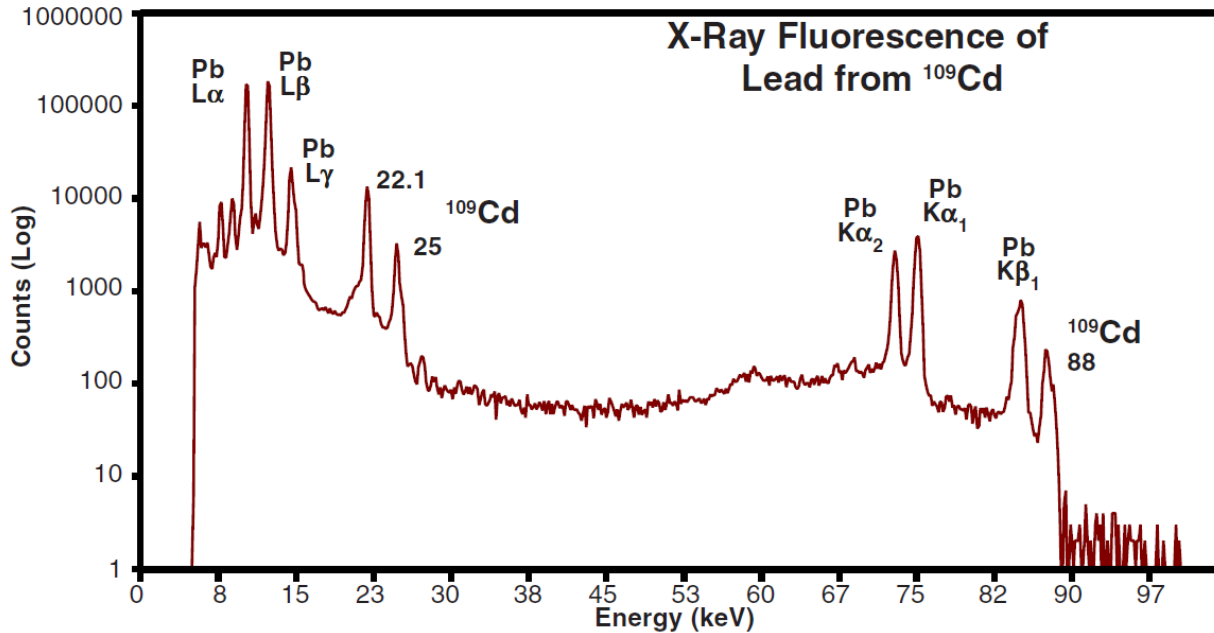
Figure 25:Spectra taken using Amptek XR-100CR 5 mm x 5 mm x 500 µm X-Ray Detector (20 µs shaping time - opnional feature) and Amptec MCA8000A Multichannel Analyzer.

The characteristic x-rays are labelled as K, L, M or N to denote the shells they originated from. Another designation alpha (α), beta (β) or gamma (γ) is made to mark the x-rays that originated from the transitions of electrons from higher shells. Hence, a Kα x-ray is produced from a transition of an electron from the L to the K shell, and a Kβ x-ray is produced from a transition of an electron from the M to a K shell, etc. Since within the shells there are multiple orbits of higher and lower binding energy electrons, a further designation is made as α1, α2 or β1, β2, etc. to denote transitions of electrons from these orbits into the same lower shell.

The XRF method is widely used to measure the elemental composition of materials. Since this method is fast and non-destructive to the sample, it is the method of choice for field applications and industrial production and mainly in art, for control of materials. Depending on the application, XRF can be produced by using not only x-rays but also other primary excitation sources like alpha particles, protons or high energy electron beams.

Sometimes, as the atom returns to its stable condition, instead of emitting a characteristic x-ray it transfers the excitation energy directly to one of the outer electrons, causing it to be ejected from the atom. The ejected electron is called an "Auger" electron. This process is a competing process to the XRF. Auger electrons are more probable in the low Z elements than in the high Z elements. The description of the phenomenon of production of X-ray and production of Auger electron is shown in Figure 26.

45
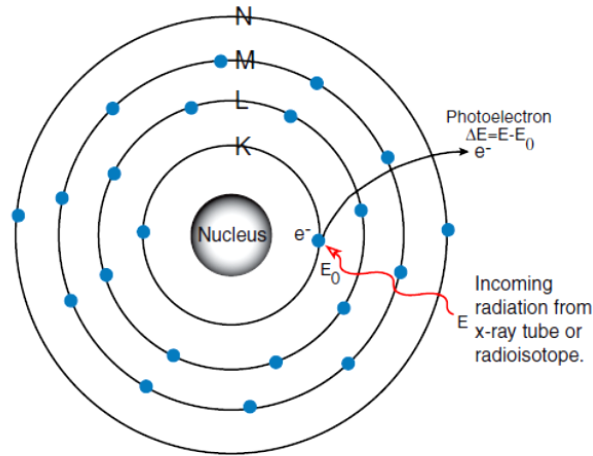
1) An electron in the K shell is ejected from the atom by an external primary excitation x-ray, creating a vacancy.

The K Lines

$\Delta E = E_1 - E_0 = K_\alpha$

$\Delta E = E_2 - E_0 = K_\beta$
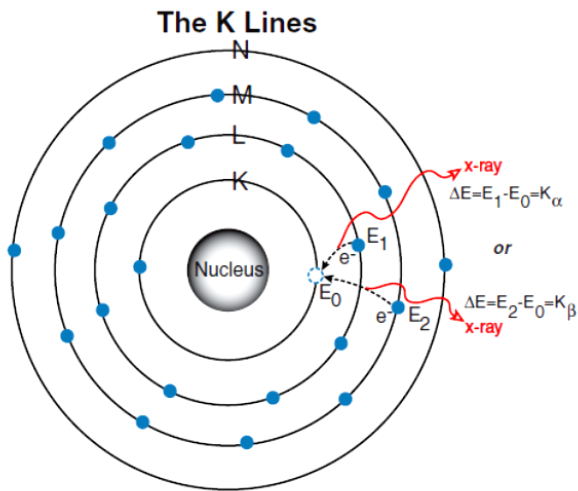
2) An electron from the L or M shell "jumps in" to fill the vacancy. In the process, it emits a characteristic x-ray unique to this element and in turn, produces a vacancy in the L or M shell.

The L Lines

$\Delta E = E_2 - E_1 = L_\alpha$

$\Delta E = E_3 - E_1 = L_\beta$
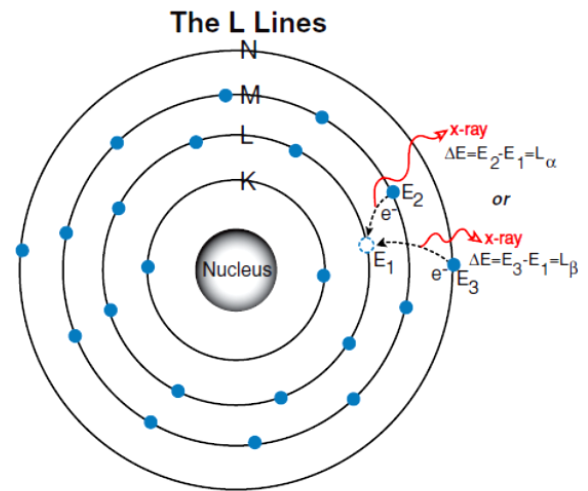
3) When a vacancy is created in the L shell by either the primary excitation x-ray or by the previous event, an electron from the M or N shell "jumps in" to occupy the vacancy. In this process, it emits a characteristic x-ray unique to this element and in turn, produces a vacancy in the M or N shell.

$\Delta E = E_1 - E_2 - E_3$
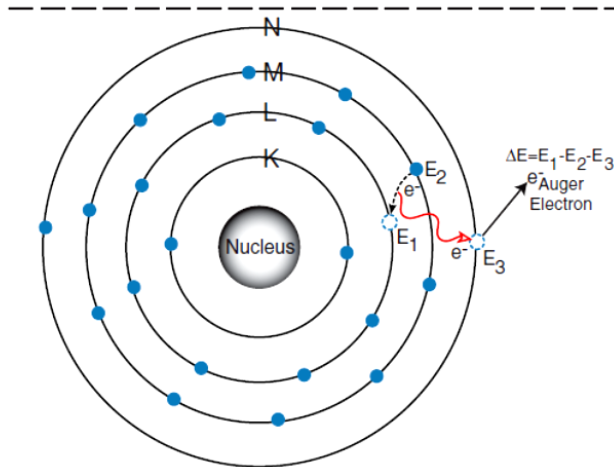
"Auger" Electron
The excitation energy from the inner atom is transferred to one of the outer electrons causing it to be ejected from the atom.

Figure 26: description of the phenomenon of production of X-ray and production of Auger electron

The device used for the XRF measurements is a Mini–X mounted on MP1 with X-123SDD, which is showed in figure 27. Mini-X is the X-ray generator and X-123SDD is the detector.

Figure 27: XRF portable setup

Mini–X is a self-contained, miniature X-ray tube system, which includes the X-ray tube, high voltage power supply and USB controller. Designed for X-ray fluorescence analysis applications - XRF.

Mini-X is the first of its kind; a self-contained, packaged, miniature X-ray tube system, which includes the X-ray tube, the power supply, the control electronics and the USB communication to the computer. It is designed to replace radioisotopes in X-ray fluorescence analysis applications.

Mini-X to simplify the XRF process by providing a grounded anode, variable current and voltage controlled via USB and ease of operation.

It features a 50 kV/80 µA power supply, a gold (Au) or silver (Ag) transmission target, and a beryllium end window.

To further simplify the use of Mini-X an AC adaptor is provided to supply the 12 VDC needed to power the system. The only connections needed to operate the tube are a USB cable and AC adaptor. A flashing red LED and a beeper warns the user when x-rays are present.

The Mini-X is designed to generate voltages up to 50 kV. The high voltage system is fully shielded inside the Mini-X enclosure.

The Mini-X contains a high voltage power supply. High voltage is not exposed, but the Mini-X should still be grounded as a precaution. It should be mounted to a metal fixture via the provided brackets.

Radiation levels external to the X-ray tube housing with the brass safety plug ON do not exceed 2.5 mrem/h measured 5 cm from the surface of the housing

Beryllium window is on the front of the unit. The ambient temperature surrounding the X-ray tube must not exceed 50° C.

The Mini-X is provided with two collimators (Fig. 28). They consists of a brass collimators with aluminium (Al) inserts and a cover that screws into the Mini-X. The collimators have 1 and 2 mm diameter holes. A brass safety plug is also provided which, when installed, reduces the flux from an operating tube to less than 25 µSv/h (2.5 mrem/hr) at 5 cm away.

Figure 28: Mini-X collimators

The Mini-X has a hardware interlock in order to prevent accidental exposure (Fig. 29). This interlock must be shorted (enabled) in order for the Mini-X to produce X-rays. The left figure below shows the interlock disabled. The Mini-X will not produce X-rays in this configuration. The right figure shows the interlock enabled. The gun will produce X-rays in this configuration. Always store the Mini-X with the interlock disabled when not in use.
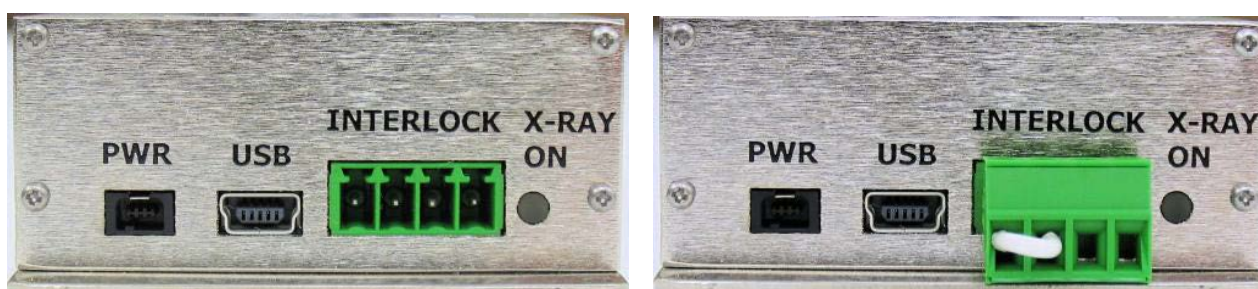
Figure 29: Showing the interlock disabled (left) and enabled (right).

This connector has two functions: it permits the user to implement a safety interlock, which turns off the X-ray tube when a switch is opened, and it permits the user to implement an external indicator to show when the tube is in use. The Mini-X is shipped with a set of filters to modify the output spectrum of the tube to better suite a particular application. The use of any filter will reduce the flux, so the current may have to be increased to obtain an appropriate flux.

The specification are showed below, in table 1.

	Silver (Ag) Target	Gold (Au) Target
Target Thickness	0.75 μm	1 μm
Tube Voltage	10 to 50 kV	10 to 50 kV
Tube Current	5 μA min. / 200 μA max.	5 μA min. / 200 μA max.
Approximate Dose Rate	1 Sv/h @ 30 cm	1.3 Sv/h @ 30 cm
Approximate Flux	10^6 counts per second/mm^2 on the axis at a distance of 30 cm (50 keV/1 μA)	1.3×10^6 counts per second/mm^2 on the axis at a distance of 30 cm (50 keV/1 μA)
Continuous Power	4 W max. @ 100% duty cycle	4 W max. @ 100% duty cycle
Window Material	Beryllium (Be); window at ground	Beryllium (Be); window at ground
Window Thickness	127 μm	127 μm
Focal Spot Size	Approximately 2 mm	Approximately 2 mm
Output Cone Angle	120°	120°
Cooling	Air cooled	Air cooled
High Voltage Stability	< 0.03% RSD	< 0.03% RSD
Leakage Radiation	<5 μSv/h (0.5 mrem/h) at 5 cm with safety plug installed	<5 μSv/h (0.5 mrem/h) at 5 cm with safety plug installed
Power Consumption	9 W at 50 kV and 80 μA	9 W at 50 kV and 80 μA
Input Voltage	12 VDC (AC adapter included)	12 VDC (AC adapter included)
Control	USB, mini-USB connector (cable included)	USB, mini-USB connector (cable included
Setting Time	Typical < 1 second	Typical < 1 second
Weight	360 g	360 g
Humidity	30 to 90% (non condensing)	30 to 90% (non condensing)
Operating Temperature	-10 °C to +50 °C	-10 °C to +50 °C
Storage Temperature	-25 °C to +60 °C	-25 °C to +60 °C
Safety Controls and Indicators	1) External hardware interlock 2) Flashing LED 3) Beeper	1) External hardware interlock 2) Flashing LED 3) Beeper
Software	Mini-X Control Software controls voltage and current Mini-X API for custom programming applications	Mini-X Control Software controls voltage and current Mini-X API for custom programming applications
Warranty	One year or 2000 hours, whichever comes first	One year or 2000 hours, whichever comes first

Table 1: specifications of Amptec Mini X

The X-123SDD combines in single package Amptek's high performance X-ray spectroscopy components: (1) the XR-100SDD silicon drift X-ray detector and preamplifier, (2) the DP5 digital pulse processor and MCA, and (3) the PC5 power supply.

The X-123SDD uses a *silicon drift detector* (SDD) similar to a Si-PIN photodiode but with a unique electrode structure to improve energy resolution and increase count rates. The SDD is mounted on a thermoelectric cooler, with the input FET and coupled to a custom charge sensitive preamplifier. The thermoelectric cooler reduces the electronic noise in the detector and preamplifier but the cooling is transparent to the user: it operates like a room temperature system.

The pulse processor is the DP5, a second generation digital pulse processor (DPP) which replaces both the shaping amplifier and MCA found in analog systems. The digital technology improves several key parameters: (1) better performance, specifically better resolution and higher count rates; (2) greater flexibility since more configuration options are available and selected by software, and (3) improved stability and reproducibility. The DPP digitizes the preamplifier output, applies real-time digital processing to the signal, detects the peak amplitude, and bins this in its histogram memory. The spectrum is then transmitted to the user's computer. The PC5 supplies the power to the detector, including low voltages for the preamps, high voltage to bias the detector, and a supply for the thermoelectric cooler, which provides closed loop control with a maximum temperature differential of 85 °C. All of these are under software control. The X-123SDD input power is unregulated +5 VDC with a current of about 250 mA.

The detector is mounted on an extender, with lengths from 0 to 9". In its standard configuration, only two connections are required: power (+5 VDC) and communications (USB, RS232, or Ethernet). An auxiliary connector provides several additional inputs and outputs used if the X-123SDD will be integrated with other equipment. It also includes an Application Programming Interface (API) DLL to integrate the unit with custom software.

Below, in table 2, are showed the most important specifications of the X-123SDD.

Spectroscopic Performance	
Energy Resolution	135 to 155 eV FWHM @ 5.9 keV
Electronic Noise (typical)	73 eV FWHM (8.7 e⁻ rms)
Energy Range	Efficiency >25% for X-rays from 1 to 25 keV. May be used outside this range with lower efficiency.
Peak to Background	7,000 to 1 (ratio of counts from 5.9 keV to 2 keV)
Maximum Count Rate	Depends on peaking time. Recommended maxima are shown below.

Peaking Time (µsec)	9.6	4.8	2.4	0.8
Shaping Time (µsec)	4.4	2.2	1.0	0.4
Recommended max input rate (sec⁻¹)	4.9×10^4	1.0×10^5	1.9×10^5	5.6×10^5
Typical resolution (eV FWHM @ 5.9 keV)	140	150	160	200

Detector and Preamplifier	
Detector Type	Si drift diode (SDD)
Detector Active Area	7 mm² (collimator area 4.45 mm²)
Detector Thickness	450 µm
Be Window Thickness	1 mil (25 µm) or 0.5 mil (12.5 µm)
Thermoelectric Cooler	2-stage (85° ΔT_{max})
Preamplifier Type	Amptek custom reset, charge sensitive
Preamp Conversion Gain	1 mV/keV

Pulse Processor	
Gain	Combination of coarse and fine gain yields overall gain continuously adjustable from 0.84 to 127.5.
Coarse Gain	Software selectable from 1.12 to 102 in 16 log steps.
Fine Gain	Software selectable, 0.75 to 1.25, 10 bit resolution
Full Scale	1000 mV input pulse @ X1 gain
Gain Stability	<20 ppm/° C (typical)
Pulse Shape	Trapezoidal. (A semi-Gaussian amplifier with shaping time τ has a peaking time of 2.2τ and is comparable in performance with the trapezoidal shape of the same peaking time.)
ADC Clock Rate	20 or 80 MHz, 12 bit ADC
Peaking Time	30 software selectable peaking times between 0.2 and 102 µs, corresponding to semi-Gaussian shaping times of 0.1 to 45 µs.
Flat Top	16 software selectable values for each peaking time (depends on the peaking time), > 0.05 µsec.
Baseline Restoration	Asymmetric, 16 software selectable slew rate settings
Fast Channel Pulse Pair Resolving Time	120 nsec

Coarse Gain steps:

1.12	2.49	3.78	5.26	6.56	8.39	10.10	11.31
14.56	17.77	22.42	30.83	38.18	47.47	66.26	102.0

Table 2: specifications of X-123SDD

2.5. X ray Photoelectron Spectroscopy – XPS

Between the contemporary surface characterization methods, electron spectroscopy for chemical analysis (ESCA) is the most widely used. ESCA is also called X-ray photoelectron spectroscopy (XPS), and the two acronyms can be used interchangeably. The popularity of ESCA as a surface analysis technique is attributed to its high information content, its flexibility in addressing a wide variety of samples, and its sound theoretical basis [30] [31].

This paragraph will introduce the ESCA method and describe its theory, instrumentation, spectral interpretation and application. The intent of this introduction is to provide a broad overview. Many general reviews on this subject exist and further reading about ESCA theory and applications is encouraged. The surface to be analyzed is placed in a vacuum environment and then irradiated with photons. For ESCA, the photon source is in the X-ray energy range. The irradiated atoms emit electrons (photoelectrons) after direct transfer of energy from the photon to core-level electrons. Photoelectrons emitted from atoms near the surface can escape into the vacuum chamber and be separated according to energy and counted. The energy of the photoelectrons is related to the atomic and molecular environment from which they originated. The number of electrons emitted is related to the concentration of the emitting atom in the sample.

For ESCA, the photon source is in the X-ray energy range. The irradiated atoms emit electrons (photoelectrons) after direct transfer of energy from the photon to core-level electrons. Photoelectrons emitted from atoms near the surface can escape into the vacuum chamber and be separated according to energy and counted. The energy of the photoelectrons is related to the atomic and molecular environment from which they originated. The number of electrons emitted is related to the concentration of the emitting atom in the sample.

The most basic ESCA analysis of a surface will provide qualitative and quantitative information on all the elements present (except H and He). More sophisticated application of the method yields a wealth of detailed information about the chemistry, electronic structure, organization, and morphology of a surface. Thus, ESCA can be considered one of the most powerful analytical tools available.

When a photon impinges upon an atom, one of three events may occur:

1) the photon can pass through with no interaction
2) the photon can be scattered by an atomic orbital electron leading to partial energy loss

3) the photon may interact with an atomic orbital electron with total transfer of the photon energy to the electron, leading to electron emission from the atom. In the first case, no interaction occurs and it is, therefore, not pertinent to this discussion.

The second possibility is referred to as 'Compton scattering' and can be important in high-energy processes. The third process accurately describes the photoemission process that is the basis of ESCA. Let us examine four observations associated with this photoelectric effect in more detail. First, no electrons will be ejected from an atom regardless of the illumination intensity unless the frequency of excitation is greater than or equal to a threshold level characteristic for each element. Thus, if the frequency (energy) of the excitation photon is too low, no photoemission will be observed. As the energy of this photon is gradually increased, at some value, we will begin to observe the photoemission of electrons from the atom. Second, once the threshold frequency is exceeded, the number of electrons emitted will be proportional to the intensity of the illumination (i.e., once we have irradiated the sample with photons of sufficient energy to stimulate electron emission, the more photons we irradiate the sample with, the more photoelectrons will be produced). Third, the kinetic energy of the emitted electrons is linearly proportional to the frequency of the exciting photons – if we use photons of higher energy than our threshold value, the excess photon energy above the threshold value will be transferred to the emitted electrons. Finally, the photoemission process from excitation to emission is extremely rapid (10^{-16} s). The basic physics of this process can be described by the Einstein equation, simply stated as:

$$E_B = h\nu - KE$$

Where E_B is the binding energy of the electron in the atom (a function of the type of atom and its environment), $h\nu$ is the energy of the X-ray source (a known value), and KE is the kinetic energy of the emitted electron that is measured in the ESCA spectrometer.

Thus, E_B, the quantity that provides us with valuable information about the photoemitting atom, is easily obtained from $h\nu$ (known) and KE (measured). Binding energies are frequently expressed in electron volts (eV; 1 eV = 1.6×10^{-19} joules).

The initial state is just the ground state of the atom prior to the photoemission process. If the energy of the atom's initial state is changed, for example, by formation of chemical bonds with other atoms, then the E_B of electrons in that atom will change. The change in E_B, ΔE_B, is called the chemical shift.

It is usually assumed that initial state effects are responsible for the observed chemical shifts, so that, as the formal oxidation state of an element increases, the E_B of photoelectrons ejected from that element will increase.

This assumes that final state effects such as relaxation have similar magnitudes for different oxidation states. For most samples, the interpretation of ΔE_B solely in terms of initial state effects is usually adequate.

$$\Delta E_B = -\Delta \varepsilon_k$$

A caution must be made against solely using initial state effects for interpreting chemical shifts. The electron rearrangements that occur during photoemission result in the lowering of E_B.

If the magnitude of the relaxation energy varies significantly as the chemical environment of an atom is changed, the EB ranking that would be expected based on initial state considerations, can be altered. Most of the atomic relaxation component results from rearrangement of outer shell electrons, which have a smaller EB than the emitted photoelectron. In contrast, the inner shell electrons (EB larger than the emitted photoelectron) make only a small contribution to the atomic relaxation energy and can usually be neglected. The form of extra-atomic relaxation depends on the material being examined. For electrically conducting samples such as metals, valence band electrons can move from one atom to the next to screen the core hole. For ionically bonded solids such as the alkali halides, electrons are not free to move from one atom to the next.

The magnitude of reduction in E_B produced by extra-atomic relaxation in ionic materials is smaller than the extra-atomic relaxation in metallic samples.

Accurate measurement of E_B can provide information about the electronic structure of a sample.

E_B is determined by measuring the KE of the emitted photoelectron. To do this properly, a calibrated and suitably referenced ESCA spectrometer is required.

Conducting samples such as metals are placed in electrical contact with the spectrometer, typically by grounding both the sample and the spectrometer. This puts the Fermi level (E_F), the highest occupied energy level, of both the sample and spectrometer, at the same energy level.

The sum of the KE and E_B does not exactly equal the X-ray energy, as implied in the Einstein equation. The difference is the work function of the spectrometer (φ_{sp}). The work function, φ, is related to the E_F and vacuum level (E_{vac}) by:

$$\varphi = E_F - E_{vac}$$

Thus, φ is the minimum energy required to eject an electron from the highest occupied level into vacuum. The Einstein equation now becomes:

$$E_B^F = h\nu - KE - \varphi_{sp}$$

Therefore, both KE and φ_{sp} must be measured to determine E_B^F. The superscript ^{F} on E_B means that E_B is referenced to E_F. For conducting samples it is the work function of the spectrometer (φ_{sp}) that is important.

This can be calibrated by placing a clean Au standard in the spectrometer and adjusting the instrumental settings such that the known E_B values for Au are obtained (*e.g. E_F = 0 eV, 4f7/2 = 83.96 eV*).

For measuring E_B, the procedure described in the previous section is the one of choice when the electrical conductivity of the sample is higher than the emitted current of photoelectrons.

As discussed previously, the complete ESCA spectrum of a material contains peaks that can be associated with the various elements (except H and He) present in the outer 10 nm of that material. The area under these peaks is related to the amount of each element present. Therefore, by measuring the peak areas and correcting them for the appropriate instrumental factors, the percentage of each element detected can be determined.

The photoionization cross-section is the probability that the incident X-ray will create a photoelectron from the orbital of element.

Therefore, below equation can be solved for n_i. Once n_i is known for each element present in the ESCA spectrum, the atomic percentages can be calculated as:

$$\%n_i = 100 \left(\frac{n_i}{\sum n_i} \right)$$

The ESCA experiment is necessarily tied to the complex instrumentation needed to stimulate photoemission and to measure low fluxes of electrons. A schematic drawing of a contemporary ESCA instrument is shown in figure 27. The equipment used in this thesis is shown in figure 31.

The primary components that make up the ESCA instrument are the vacuum system, X-ray source, electron energy analyzer, and data system (Fig. 30) [32].
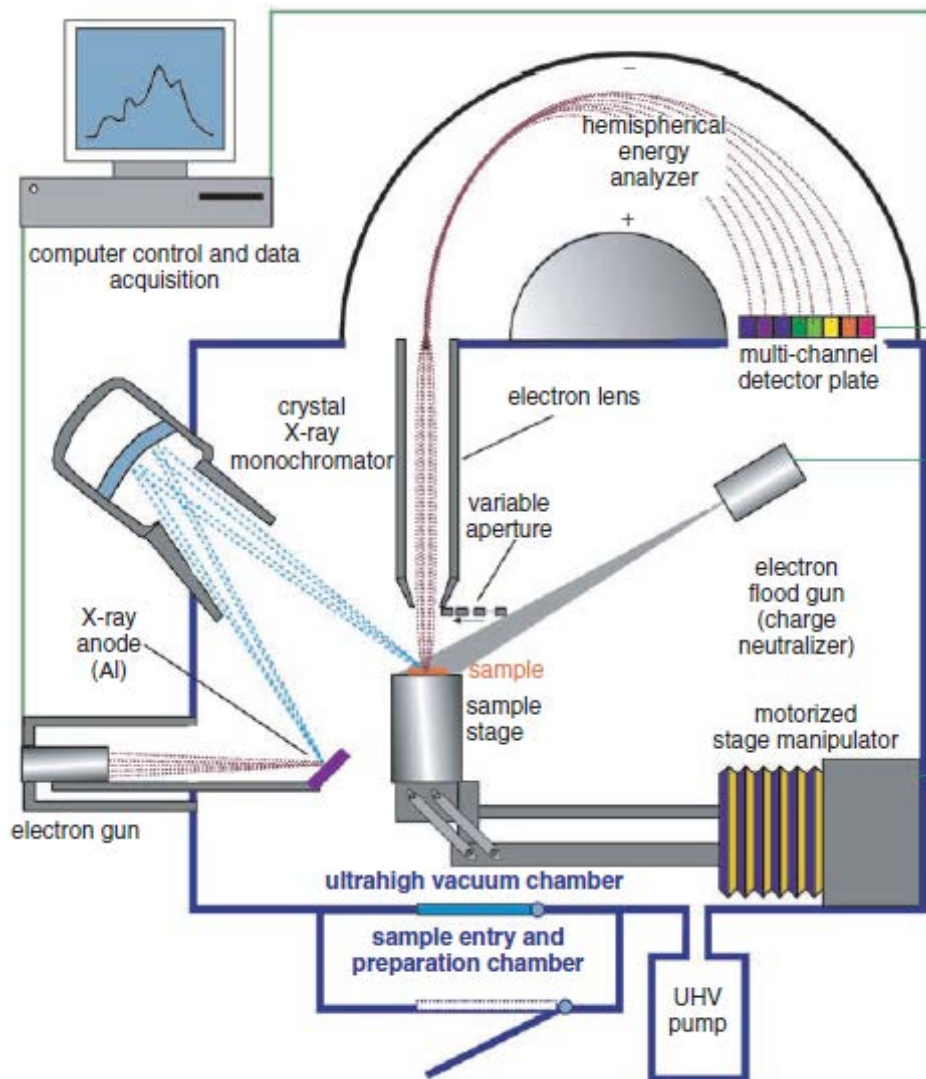
Figure 30: A schematic diagram of an ESCA spectrometer using a monochromatized X-ray source. The key components of a modern spectrometer are identified

Figure 31: equipment used for XPS

The heart of the ESCA instrument is the main vacuum chamber where the sample is analyzed (analysis chamber).

For XPS analysis, the samples have been placed in the analytical chamber, they must be properly positioned for analysis. This is accomplished with a sample holder/manipulator.

Sample manipulators typically have the capability to translate a sample in three directions and to rotate it in one or two directions (figure 32).

Figure 32: sample manipulator

X-rays for an XPS experiment are usually produced by impinging a high-energy (~10 keV) electron beam onto a target.

A specific fluorescence line is used instead of the background emission (Bremsstrahlung) since its intensity is several orders of magnitude higher than the background emission. Most spectrometers use only one or two anodes, with Al and Mg the most common for non-monochromatic sources and Al the most common for monochromatic sources. Instead, in our case was used Mg (Kα: 1253.64 eV). Since most of the incident electron energy is converted into heat, anodes are usually water cooled. This allows operation at higher power loads without significant degradation (e.g. melting).

The energy resolution of the X-ray source is determined by the natural width of the fluorescence line (typically 1–2 eV). Besides, the emission from weaker (satellite) X-ray fluorescence lines will also strike the sample, resulting in the appearance of satellite peaks in the ESCA spectrum and high-energy electrons, Bremsstrahlung, and heat will strike the sample, which can result in sample degradation. These are several disadvantages. The flux of electrons and Bremsstrahlung can be minimized by placing a thin, relatively X-ray-transparent foil between the X-ray source and the sample. The presence of the foil will also minimize contamination of the sample by the X-ray source. For Al and Mg anodes, a ~2 μm thick Al foil is commonly used. The best way to optimize single energy production is to use an X-ray monochromator. The most popular monochromatized source combines an Al anode with one or more quartz crystals. The lattice spacing for the 1010 planes in quartz is 0.425 nm, which is appropriate for the Al Kα wavelength (0.83 nm). For these wavelengths, the Bragg relationship (nλ = 2dsin θ) is satisfied at an angle of 78°.

The area of the sample irradiated by the X-source depends on the geometry of the source and the type of electron gun used to stimulate X-ray emission. Most non-monchromatized sources illuminate a spot that is a few centimeters in diameter. In contrast, the monochromatized sources typically illuminate an area that is a few millimeters or smaller in diameter. With a focused electron gun and the quartz crystal used as both a monochromator and a focusing element, spot sizes <50 μm in diameter can be realized.

The most common type of energy analyzer used for ESCA experiments is the electrostatic hemispherical analyzer. It consists of two concentric hemispheres of radius R_1 and R_2. A potential of ΔV is placed across the hemispheres such that the outer hemisphere is negative and the inner hemisphere is positive with respect to the potential at the center line, $R_0 = (R_1 + R_2)/2$.

This will maintain a constant absolute resolution, ΔE, for all photoelectron peaks, since the analyzer resolution is defined as $\Delta E/E$, where E is the energy of the electron as it passes through the analyzer. This ratio is a constant for a given analyzer, so if E is fixed (constant pass energy), ΔE will be fixed. This relationship shows that the lower the pass energy, the smaller ΔE will be.

The data acquisition is performed by employing a computer with Keithley 3108-KPCI interface, used to convert analog-to-digital data and vice versa. The interface sends the voltage to the lens of the analyzer, to fix the energy analysis and receive the response signals. The final data are the mean of several acquisitions, in order to reduce the effects of background noise.

The ESCA experiment must be conducted under vacuum for three reasons. First, the emitted photoelectrons must be able to travel from the sample through the analyzer to the detector without colliding with gas phase molecules. Second, some components such as the X-ray source require vacuum conditions to remain operational. Third, the surface composition of the sample under investigation must not change during the ESCA experiment. Only a modest vacuum ($10^{-6}–10^{-7}$ torr;

1 torr = 133 Pa) is necessary to meet the first two requirements. For most applications, a vacuum of 10^{-10} torr is adequate.

Samples are typically introduced into the analysis vacuum chamber via a load-lock or preparation chamber. In its simplest form, the load-lock is a small volume chamber that can be isolated from the analytical chamber and then backfilled to atmospheric pressure. One or more samples are placed in the load-lock chamber, which is then evacuated, typically with a turbomolecular pump. After the samples are pumped down, they are transferred into the analytical chamber. Depending on the vacuum requirements and the type of samples, the pump down process can be as short as a few minutes or as long as several hours. In many cases, it is desirable to do more elaborate sample processing before introducing the sample into the analytical chamber. For these cases, custom chambers providing an UHV environment with ion guns, deposition sources, sample heating and cooling, sample cleaving, gas dosers, etc., are available. The configuration of these sample preparation chambers depends on their intended use.

In order to reduce the number density of gas particles, and thereby the pressure, in a vessel, gas particles must be removed from it. This is the purpose of the vacuum pump. Fundamentally, a distinction can be made between two classes of pump:

- Those that remove gas particles from the pumped volume and convey them to the atmosphere in one or more stages of compression. These are called compression or gas transfer pumps.
- Those, which condense or chemically bind the particles to be removed to a solid wall, which is often part of the vessel being pumped. These are called entrapment pumps.

Within these two classes, there are subsections which further distinguish the method of operation of a pump. In the class of compression pumps there are:

a) Pumps that operate by creating periodically increasing and decreasing chamber volumes.
b) Pumps that transfer gas from a low pressure to a high-pressure side in which the pump chamber volume is constant.
c) Pumps in which the pumping action is due to diffusion of gases in a stream of high velocity particles.

In the class of entrapment pumps there are:

a) Pumps that pump vapours by condensation or remove gases by condensation at very low temperatures.
b) Pumps that bind or embed gases at extensive gas-free surfaces by adsorption or absorption.

3.   Materials

For the development of this thesis, we have been taken into consideration different materials which are the main components of archaeological artifacts. We worked on both artifacts and commercial pure materials.
All the analysed materials were divided into three categories: metals, alloys and artificial stone.
For each category, we have chosen a representative material. The results obtained are comparable with those from literature.
For metals category of has been studied Silver, for alloys the bronze and for artificial stone materials the pottery.

3.1.   Metals

Since ancient times, the first metals used have been copper, gold and silver, i.e. metals that are found in the native state, and that have mediocre mechanical properties and low hardness for machining. Metallic materials are studied from the archaeometric point of view. Many studies for establishing the metallurgical technology of ancient civilizations use the identification of the chemical composition and the study of the surface morphology.
To study the effect of LA on the metals we have considered silver.

3.1.1.   Silver in cultural heritage

The silver is part of noble metals, with copper and gold. Silver, in antiquity, was less common than gold. It is found in small quantities in the native state, pure or associated with gold, and most often in the form of

sulphide (argentite, Ag_2S) associated with lead minerals or other elements. Among all the elements, it is the best conductor of electricity.

Silver was used in the production of coins, statues and other objects of daily use, but also in the mosaics and stained glass in the form of nanoparticles.

A very important issue for silver is corrosion, which depending on the exposure conditions (atmospheric exposure, underground, submersion, etc.) and duration of exposure. The alterations of the artefact are in relation and in equilibrium with the environment in which it is located. By varying the exposure conditions, the building will have to find new equilibrium conditions and therefore will undergo further transformations that can degrade and destroy it further, without appropriate intervention. Therefore, in most cases, to bring the artefact to the original aspect must use cleaning procedures.

Cleaning of metal surfaces is an important process in industry, in medical applications and in the conservation of cultural heritage. The conventional surface-cleaning techniques make use of ultrasonic technology and organic solvents (as carbon fluoro-chloride); nevertheless, these techniques commonly induced environmental pollution (causing, for example, depletion of the ozone layer) and can be toxic for human operators [33].

3.1.1.1. <u>Experiments on Silver</u>

In the last decades, the LA techniques have shown an excellent alternative to organic solvent in the treatment of metallic surface and in conservation and restoration of cultural heritage. The scientific investigations have focused on the efficiency, selectivity and efficacy of laser ablation, as well as on the possible advantages that it can provide with respect to traditional cleaning techniques.

One of first applications of the laser cleaning on metal artworks was made on the bronze panels of the *Porta del Paradiso* by Lorenzo Ghiberti [34]. It represents the first case where was operated a critical selection of the optimum laser parameters and was provided a study of laser pulse duration in cleaning process.

Several works on gold, silver and bronze artifacts have definitely demonstrated the effectiveness of LA in metal artifacts cleanness. In fact, the LA remove organic matrix patinations on archaeological artifacts reducing the impurities amount on sample surface [34].

A very frequent phenomenon on silver is the tarnishing. Tarnish is a thin layer of oxidation that forms over silver and other similar metals. Tarnish does not always result from the only effects of oxygen in the air. It often appears as a dull, gray or black film or coating over metal.

Particular attention must be dedicated to the effect of LA in different medium to study the characteristics of tarnishing. In effect, several archaeological artifacts are found in marine sites and often the removal from original sites is much difficult and can damage the artifacts. Moreover, increasingly the archaeologists prefer not to alter the marine archaeological sites and restore ancient artifact directly underwater conditions.

One of the well-known and unresolved problems of laser ablation on metals is the tarnishing of silver and gold using Nd:YAG (1,064 nm) laser which preclude the possibility to restore precious artifacts with the simple laser ablation technique. This in fact causes the confinement of laser cleaning to stone reliefs and bronzes statues [35].

3.1.1.1.1. LA on silver

LA procedure was performed in different medium (air, water and vacuum) demonstrating that in vacuum conditions not only the tarnishing problem is absent but also the cleanness is most effective eliminating the residuals of chloride. The experiments have been conducted on a series of commercial silver treated with HCl to simulate the formation of chloride patina in marine environmental. The LA cleanness was performed on pure Ag samples and HCl treated samples to understand the origin of tarnishing.

The experiments were conducted on a series of silver (purity > 99.99%) samples (A, B, C, E1-E3) with dimensions of 1 cm × 2 cm and a thickness of about 50 μm.

Samples A, B and C were immersed in a solution of HCl 37% for 72 h. The obtained samples are heated at about 120 °C to evaporate the residuals of HCl. The formation of chloride patina is observed on the samples. The patina, with thickness of about 300 microns (figure 33), gives a brownish colour to the sample. All the samples of E series are submitted to cleanness treatment in as received condition without treatments.

Each sample was submitted to cleaning procedure by laser ablation in different conditions: in air (samples A and E1), in marine water (samples B and E2) and under vacuum conditions (samples C and E3).
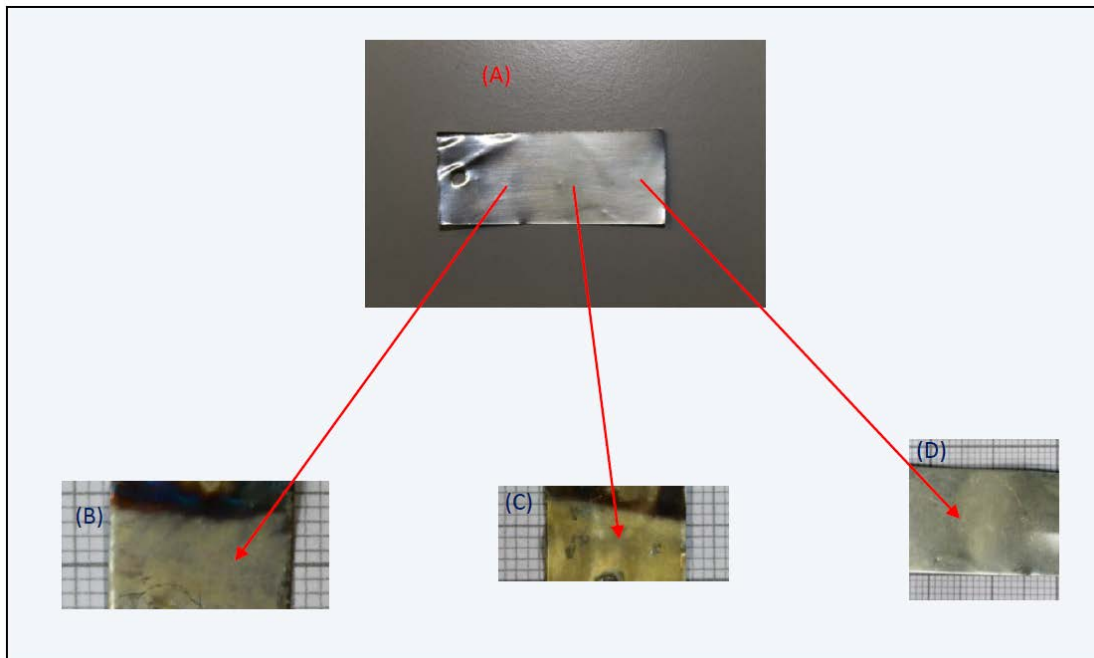
Figure 33: Images of (a) HCl treated Ag; (b) HCl treated Ag ablated in air; (c) in water; (d) in vacuum conditions.

The laser ablation procedure was performed irradiating for 1 h each sample by the output of the first harmonic (1.064 nm) of a Quanta-Giant series 710 Nd:YAG laser operating at 20 Hz. The spot size of the laser beam on the surface of the silver plate is about 4-5 mm and the power of laser is fixed at 500 mJ/pulse.

The cleanness procedure in marine water was obtained placing vertically the sample in a glass vessel (transparent to 1,064 nm) filled with a 40 mL of liquid (see figure 34 for laser ablation experimental setup).
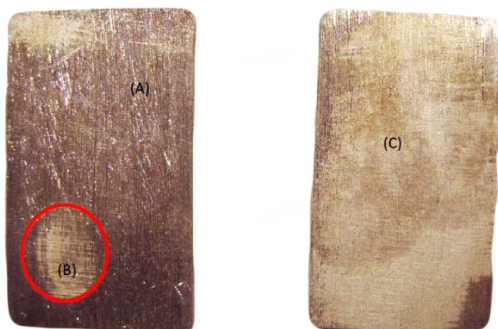
Figure 34: Pure Ag sample (a) ablated in air; (b) in water; (c) in vacuum condition.

Laser ablation under vacuum condition was conducted introducing the sample in a vacuum chamber with a pressure of about 10^{-8} torr while the laser beam reaching the sample trough a viewport in Kodial glass (borosilicate) and sapphire, transparent to 1,064 nm. In figure 35 a sketch of setup.
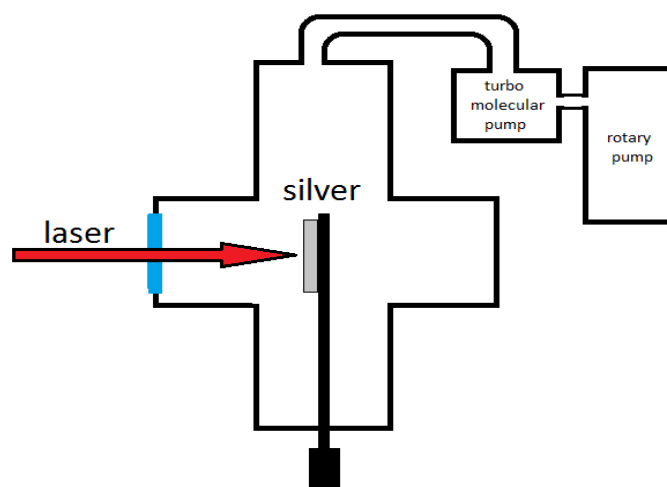
Figure 35: sketch of vacuum LA setup.

XPS measurements were conducted in an UHV (ultra-high vacuum) chamber equipped for standard surface analysis with a pressure in the range of 10^{-9} torr. Non-monochromatic Mg-Kα X-ray (hv=1,253.64 eV) was used as excitation source.

3.1.1.1.2. XPS analysis on Silver

The XPS spectra were calibrated with the C1s peak of a pure carbon sample (energy position 284.6 eV). All XPS spectra have been corrected by the analyser transmission factor and background subtracted using the straight-line subtraction mode. Moreover, the XPS data were fitted assuming a Gaussian distribution.

3.1.1.1.3. Optical absorption and reflectance analysis

. The reflected spectrum was obtained by a TRIAX 3,200 spectrometer (Jobin-Yvon) working in the 350-1,200 nm range. The white lamp of an Olympus microscope (Horiba-Jobyn Yvon) has been used as light source to enlighten the samples (through the 100 X objective). Reflectance *(r(λ)* and absorbance *(a(λ)* as function of wavelength are obtained with the well known relations:

$$r(\lambda) = \frac{I_r(\lambda)}{I_s(\lambda)}$$
$$a(\lambda) = I - r(\lambda)$$

Considering zero the transmittance.

The integrated reflectance *R(t)* and absorbance *A(t)* of each spectral transition was obtained by numerical integration, assuming a Gaussian distribution of the spectral bands.

3.1.1.1.4. Results on silver

The main difference observed on surfaces after LA in different medium is the appearance of a white patina on samples subjected to LA in air and in marine water (Figs. 33b-33c). The patina is absent in the sample ablated in UHV conditions (Fig. 33d).

The aim of this work is to investigate the origin of this patina explaining if it is linked to absorption of atmospheric elements during LA or caused by structural changes in Ag after LA.

Particularly interesting is the observation of patina formation also when pure Ag samples are ablated in air or water. In fact observing Fig.34, the different images indicate that the patina formation is not linked to HCl treatment and to presence of chlorine composite on surfaces, as explained below. It is well known, in fact, that the composites of silver and chlorine are extremely photosensible and that they can be impressed by a visible radiation forming colored patina on substrate [33]. Samples of pure Ag ablated in air and in water show the formation of white patina (Fig. 34), therefore in these samples the patina is less intense. Only after LA under vacuum condition the white substrate not appears on HCl treated (or pure) sample.

The chemical composition information on the samples and information on the structure of chemical bonds are obtained with XPS analysis. Survey spectra on as received sample (Fig. 36a) reveal the only presence of Ag as constitutive element of and O and C as impurities (probably adsorbed from atmosphere). Moreover survey spectra for HCl treated samples (Fig. 36b) show the additional presence of Chlorine, indicating the formation of a chemical patina on a sample surface.

The position of the peaks for all elements is almost identical in all samples (as received, HCl treated and LA cleaned) and allows us to identify the chemical bonds between atoms on sample surfaces and the patina composition.

The C1s line on all samples can be described as superposition of two lines centered at about 284 eV (main line of C1s) and 285.6 eV indicating the presence on surface of C-O structures. The Ag 3d 5/2 and 3d 3/2 lines (these taken for sample A has indicated in the inset of Fig. 36a) are centered at about 367.6 eV and 373.5 eV respectively indicating the presence of AgO [36]. Nevertheless the center peak for Ag 3d 5/2 line is very close to the value for AgCl (367.1 eV) and it is impossible to distinguish the two lines in treated samples because the experimental resolution of authors' data is about 0.5 eV. The chloride formation is definitively indicated by the Cl 2p lines taken from HCl treated samples (Fig. 36 B); the line is, in fact, center at 198.63 eV indicating the formation of AgCl [36].
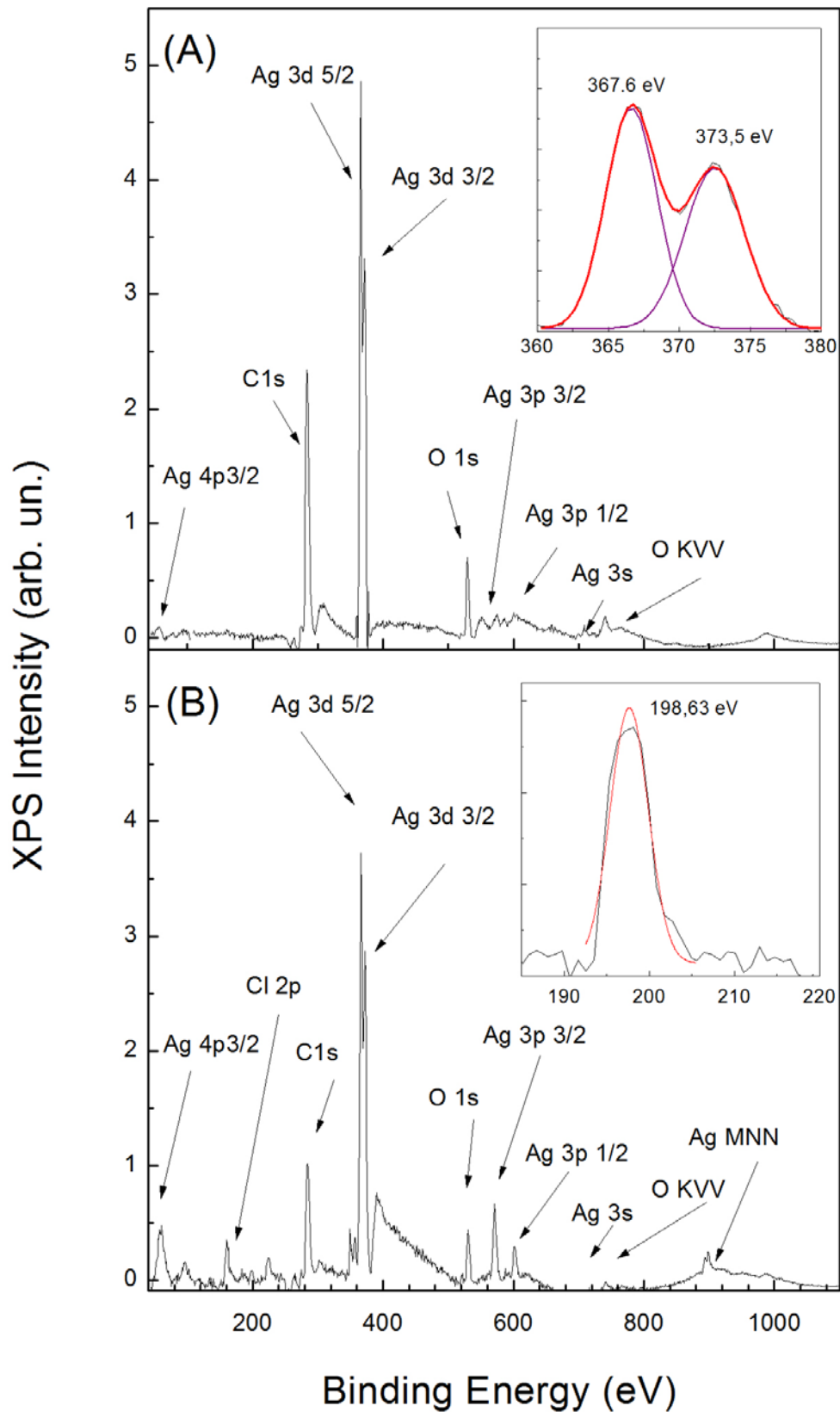
Figure 36: XPS survey spectra for (a) pure Ag sample and (b) HCl treated sample. Inset (a) Ag 3d5/2 and 3d3/2 lines for sample A and their Gaussian Analysis (b) Cl 2p line for HCl treated sample and its Gaussian analysis.

Table 1 indicates the element percentage in HCl treated and in LA cleaned samples. It is clear that the HCl treatment introduce a strongly presence of Cl which is reduced of about 3% by LA in air and marine water while disappears completely when LA is conducted in UHV ambient, clearly indicating the great effectiveness of this cleanness method in UHV.

	Ag	Cl	C	O
HCl treated Ag	10.83	7.66	77.63	3.88
HCl treated Ag ablated in air	10.69	4.13	78.75	6.43
HCl treated Ag ablated in water	10.50	4.23	77.84	7.43
HCl treated Ag ablated in vacuum	11.43	0	85.37	3.20

Table 3: Percentage of elements on sample surface obtained from XPS data.

The presence of pristine impurities of C is unchanged in all samples, indicating the inability of LA to remove the carbon residuals on surface. The presence of oxygen is unchanged for sample ablated in UHV while it increases in other samples, indicating the absorption of oxygen on surface if LA is conducted in ambient reach in oxygen.

The analysis of oxygen percentage indicates that a possible origin of white patina is the interaction between silver and oxygen.

This hypothesis is confirmed by analysis of optical reflectance and absorbance of different samples showed in Figs. 37 and 38.
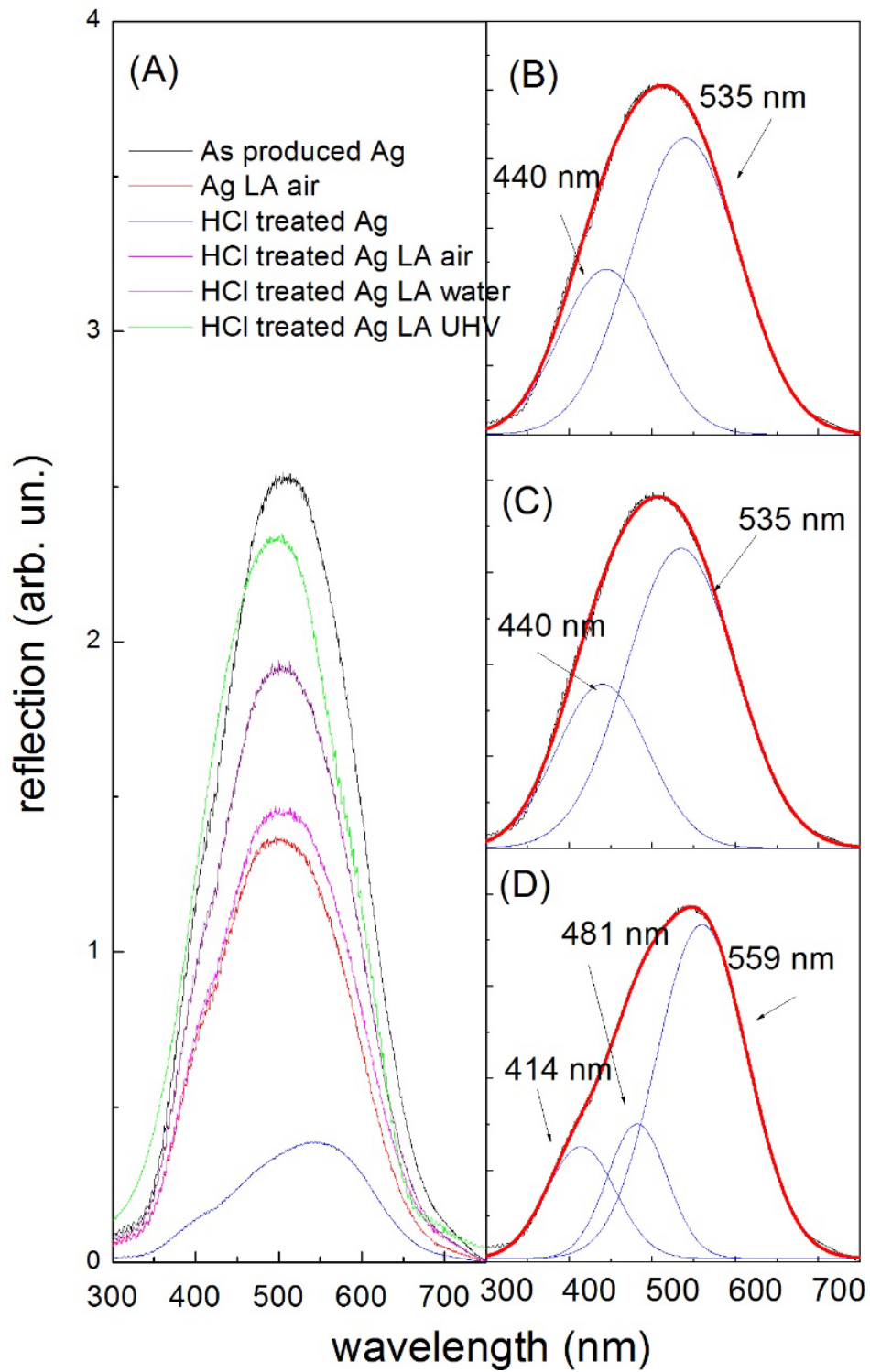
Figure 37: (a) Reflected spectra for all samples; (b) Gaussian Analysis for pure Ag; (c) Gaussian Analysis for HCl treated Ag ablated in air; (d) Gaussian Analysis for HCl treated Ag
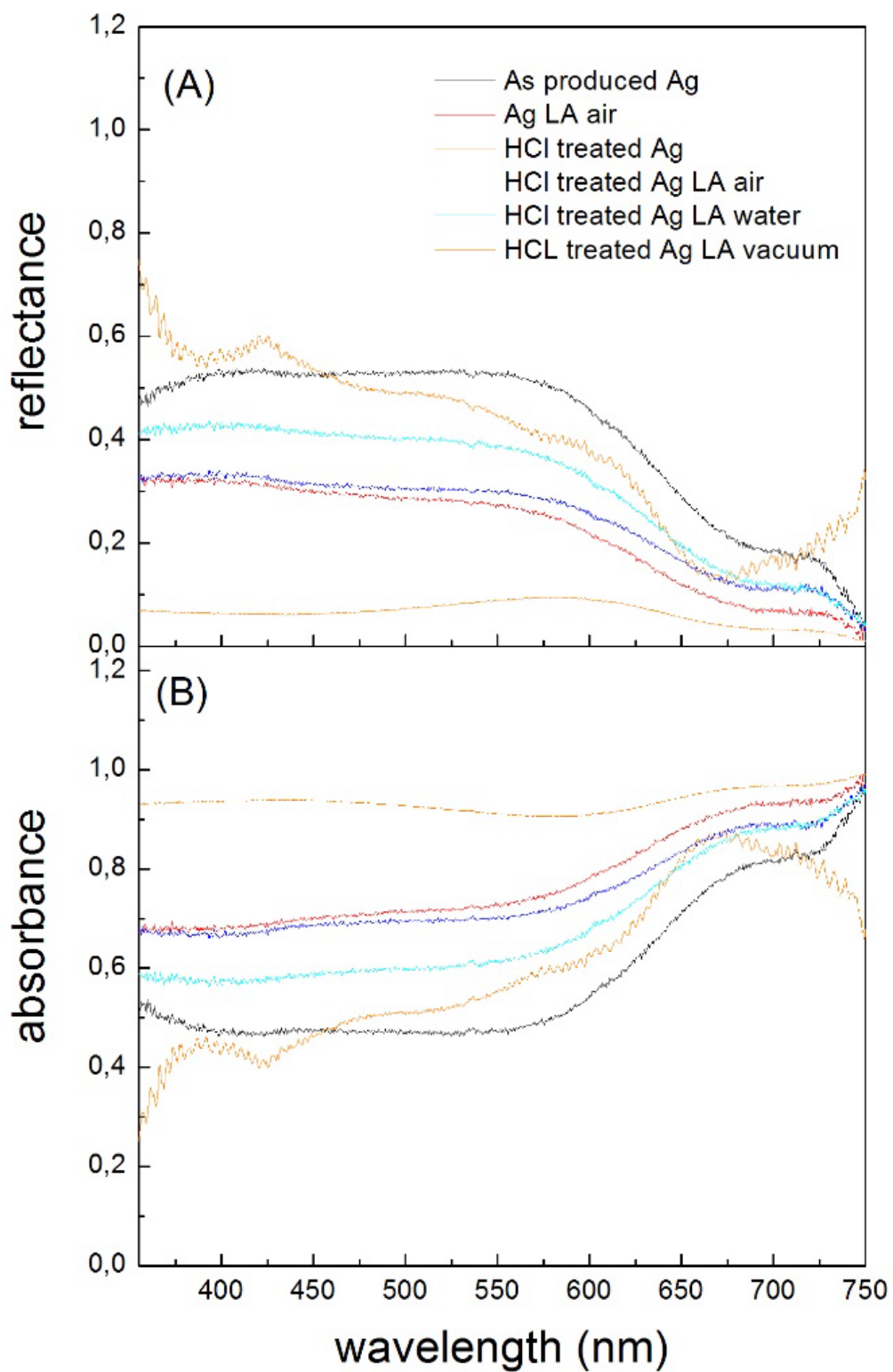
Figure 38: Reflectance and absorbance spectra for all samples.

The reflected spectra of all samples are showed in Fig. 37. It is clear that only the spectrum of HCl treated sample shows a different shape with three bands at 414 nm, 481 nm and 559 nm. All the cleaned samples display the same shape of as produced Ag with two main bands at 440 nm and 535 nm. The difference between the as produced and the ablated sample is only in the reflected intensity, as clearly visible in absorbance and reflectance spectra in Fig. 38 and in Table 4.

	Total reflectance	Total absorbance
Ag	0.48	0.52
Ag ablated in air	0.26	0.74
HCl treated Ag	0.07	0.93
HCl treated Ag ablated in air	0.28	0.72
HCl treated Ag ablated in water	0.36	0.64
HCl treated Ag ablated in vacuum	0.54	0.46

Table 4: Total reflectance and absorbance.

It is interesting to note that there are no differences in shape and in intensity between as produced and UHV cleaned samples. The only chemical difference observed in different cleaned samples is the oxygen percentage, that, as previous noted, increases during LA in medium reach in oxygen (air and water) while is unchanged when the LA become in oxygen free ambient (UHV conditions).

The absence of changes in reflectance shape indicates the absence of substantial chemical changes on surfaces. Moreover, the decrease in AgCl presence after laser ablation and the presence of patina on pure Ag samples exclude the possibility to link its formation to AgCl on sample surface.

Therefore, the white coloration assumed during LA in water and in air is a surface "tarnishing" caused by the formation of a silver oxide (AgO) thin film on sample surface during laser ablation. The AgO film causes decreases in light reflectance obtaining the "tarnishing" effect visible in Figs. 33b and 33c.

3.2.   Alloys

Since remote times, the alloys could be obtained in two ways: in the first method, combining simultaneously, in the same melting various metals; in the second method by combining the metals in two by two to obtain the final alloy more complete, having already obtained the first combinations. Today we understand that the second method is preferable, because during the melting of a metal, it is preferred to start from the metal of the highest point of fusibility until the one with the lowest point. To prevent the occurrence of liquation (withdrawal) must obtain a rapid cooling of the alloy. A too slow cooling result in a crystallization, which produces a lesser homogeneity of the alloy.

In this study was considered the alloys most famous and oldest in the world, namely, the bronze.

For about 2,000 years, from around 3,000 BC to 1,000 BC, bronze was the most important metal used for industrial purposes. Although the use of iron made tools began to increase after 1,000 BC, in the Roman world, bronze continued to be an essential medium. Like the Greeks and Egyptians before them, the Romans used bronze in numerous ways. Roman cooks used bronze pots and pans; some furniture was made of bronze, as were buckles and brooches for Roman military personnel used fastening clothing and belts, and bronze armor and other equipment. Additionally, in private homes and gardens and in public places, like the Roman Forum, bronze figurines and statues of gods, athletes, heroes, and government officials were ubiquitous. While bronze work and sculptures were prevalent during this period, it is important to note that, unlike their natural-stone counterparts, very few of these wonderful works have survived the ages. The reason is not necessarily that the material could not stand the test of time, however. In fact, many historians believe that eventually, bronze artwork that had no functional purpose was melted down to be used for tools and weaponry, especially in times of war. Additionally, other pieces that were not well guarded may have been stolen and melted down, as the bronze material proved to be very valuable.

Bronze-working generally became associated with statues of gods. It was discovered that Ceres was the first image cast in bronze in Rome. The art then passed from representations of gods to statues and likenesses of men in a variety of forms. Over time, the methods where perfected more and more and the finishes changed some. Overall, the same techniques used to create bronzes are applied today as they were in the old Roman days. The elegant bronze statues offered today are certainly created with the same artisan skill and precision, bringing not only a touch of our collective history, but also beauty that was revered in times long past, to our own era [37].

3.2.1. Bronze in cultural heritage

The name "bronze", indicated the copper-tin alloys, used since the second half of the third millennium BC in statuary, but also to produce weapons and bells. Bronze is an alloy, comprising copper (at around 80-90%) alloyed with tin and lead. Small amounts of other metals such as zinc, iron, nickel or silver may be found. Bronze founders used various metals in the casting process to take advantage of properties such as increased fluidity (zinc) and casting sharpness (lead).

The bronze so-called "for foundry", i.e. that of manufactured products, it has a percentage of tin generally variable from 4 to 10%. Today, there are bronzes with aluminium (copper-aluminum), silicon bronzes (copper-silicon), beryl bronze (copper-beryllium) and always bronzes containing tin, but with the addition of phosphorus (phosphorous bronze). The modern bronzes are used in many fields while the bronze for foundry, used for modern statuary, retains essentially the same chemical composition of a time [38].

In the context of Cultural Heritage, the most interesting alloy is the bronze alloy. With regard to the work of this thesis is appropriate to pay attention to the copper, which is the main component of bronze and consequently on the mechanism by which it can be affected causing the formation of so-called patina of alteration.

The *patina* is an alteration of the metal surface and results from the interaction between original bronze artifacts with the surrounding environment.

Into interface, between artifact and the environment, occurring processes of chemical and electrochemical corrosion, which determine an alteration of the metal surface. The result of these corrosive processes of surface lasted for years, centuries or millennia, is called patina [38].

The patina is a composite layer of corrosion products that still contain, at least partially, information on the original surface. The factors that activate the processes of corrosion are oxygen, water (which allows phenomena of electrochemical nature) and the earth with its components such as sulphur, carbonates, acids, chlorides, oxidizing agents, organic materials and high temperatures.

For artifacts that originate from excavation, it is known that alterations and modifications of the patina are due to a different growth environment, and then changing the environment change the factors that influence the formation of the patina itself. The patina might also be subsequently modified by restoration or maintenance. Finally, there may be contaminants in the air of urban environments or museums where they are stored.

The patina can be one of the most important factors of evaluation in a bronze artifact [39].

The process of formation of the patinas bronze in natural environments is in most cases linked to a phenomenon of decuprification, or to the process of selective dissolution of copper, connected to an internal oxidation of the alloys. In the literature, are often classified two main types of patinas, according to the presence or absence of an original surface (layer marker) that keeps the original shape of the artifact.

1) In the first type, the original surface is visible or hidden by simply crusting of earth. This type of coating has some remarkable protective properties and is usually characterized by an enrichment of tin on the surface, due to the dissolution of copper, in addition to the presence of carbonates, silicates, sulphates, etc..

2) In the second type of patina, usually the original surface has been destroyed or distorted by attacks of grave corrosive agents. It is systematically shown by the presence of compounds of oxide or hydroxide, with a relative enrichment in Cl [39].

3.2.1.1. <u>Experiments on commercial bronze</u>

Archaeological artifacts, bronzes in particular, are characterized by the formation of corrosive patinas on surface, which seriously damage them. Archaeological bronzes, in particular, are subjected to the so-called "bronze disease", a post: burial cyclic corrosion phenomenon occurring in atmosphere or in marine water, due to the presence of cuprous chloride (Cu_2Cl_2) within the patinas. Bronze disease rather than to get a deeper insight into the corrosion behaviour of Cu-Sn alloys in natural environments. Some authors have described the corrosions process indicating as cleaning mechanism the removal of chloride from patina with different techniques as chemical cleaning or laser ablation [40].

Below, will be shown a study of the LA effects on bronze disease patina in air and water environments, demonstrating the great effectiveness of LA under water conditions. The sample surface was monitored by X-ray photoelectron spectroscopy (XPS) and optical microscope images.

3.2.1.1.1. LA on bronze

Particular attention must be dedicated to the effect of LA in different medium. In effect, several archaeological artifacts are found in marine sites and often the removal from original sites is much difficult and can damage the artifacts. Moreover, increasingly the archaeologists prefer not to alter the marine archaeological sites and restore ancient artifact directly under water conditions.

The experiments were conducted on a series of commercial bronzes with dimensions of 1 cm x 2 cm and a thickness of about 0.5 cm (Fig. 39 and 40a). Commercial bronzes have different composition respect to archaeological artifacts (as example Zn is absent in archaeological bronzes while is present in modern alloy), therefore our study is direct to the possibility to remove chloride from bronze surface without changing the chemical compositions of patina and alloy. For this purpose, commercial bronze is ideal because we can simulate the disease patina and study the effect of laser ablation on alloy chemical composition without damaging precious artifacts.

Figure 39: bronze
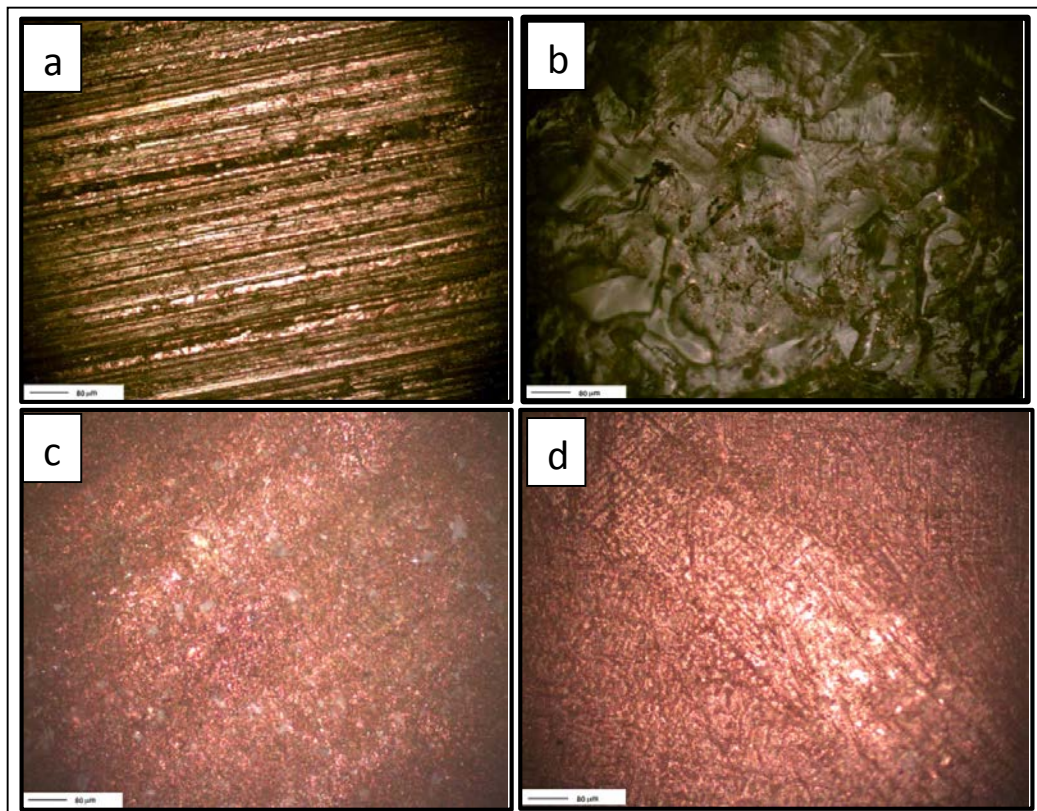
Figure 40: (a) Optical images of commercial bronze sample; (b) bronze disease patina obtained by HCl treatment; (c) samples after laser ablation in air and (d) marine water.

 To simulate the formation of chloride on bronze surface, we treat the bronze with HCl. The patina obtained in this way is different to natural patina because it is composed only by cupreous chloride while the natural patina constituents are copper-containing compounds but is the copper chloride the responsible of bronze degradation which must be eliminated in cleanness process.

Each sample was immersed in a solution of HCl 37% for 190 h. The samples as obtained are heated at about 120 °C to evaporate the residuals of HCl. On the sample we can observe the formation of a patina of bronze disease with a thickness of about 300 μm (Fig. 40b). Then each sample was submitted to cleaning procedure by laser ablation in air (sample B2) and in marine water (sample B3).

We also show, for comparison with laser ablation, the results achieved after the cleanness of as received bronze by ion bombardment in ultra-high vacuum chamber (sample B1).

The laser ablation procedure was performed irradiating for 2 h each sample by the output of the second harmonic (532 nm) of a Quanta-Giant series 710 Nd:YAG laser operating at 20 Hz. The spot size of the laser beam on the surface of the bronze plate is about of 4-5 mm and the power of laser is fixed at 300 mJ/pulse. The cleanness procedure in marine water was obtained placing vertically the B3 sample in a glass vessel (transparent to 532 nm) filled with a 40 mL of marine water (Fig. 41 for laser ablation experimental setup). Optical images of cleaned samples (Fig. 40c for B2 and Fig. 40d for B3) clearly show that the laser ablation strongly reduces the patina thickness until dimension of few microns as also demonstrated by XPS.
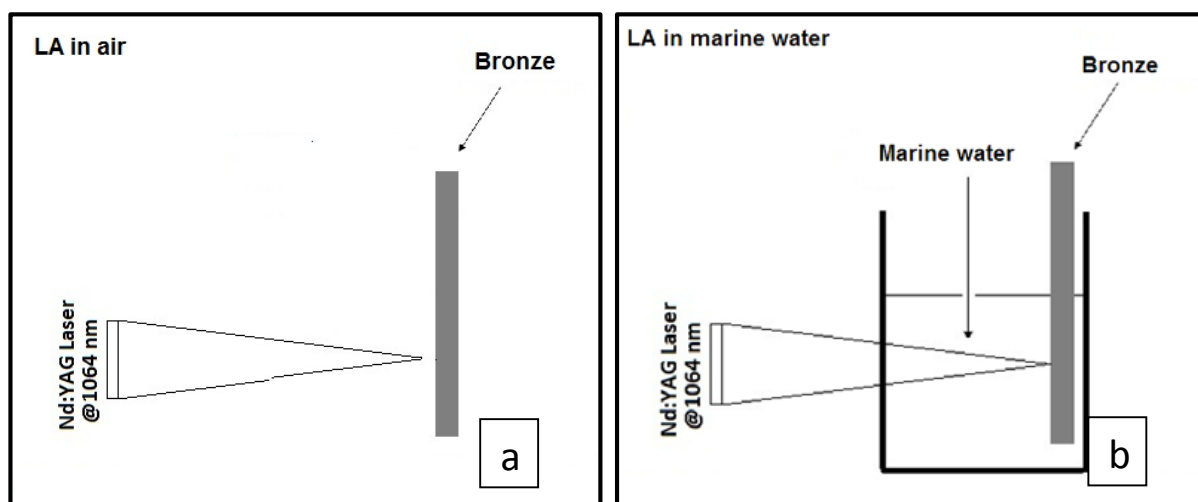
Figure 41: Experimental setup for laser ablation: (a) in air and (b) in marine water.

3.2.1.1.2.   XPS analysis on bronze

XPS measurements were conducted in an ultra-high vacuum (UHV) chamber equipped for standard surface analysis with a pressure in the range of 10^{-9} torr. Non-monochromatic Mg-Kα X-ray (hv=1,253.64 eV) was used as excitation source. The XPS spectra were calibrated with the C1s peak of a pure carbon sample (energy position 284.6 eV). All XPS spectra have been corrected by the analyser transmission factor and background subtracted using the straight-line subtraction mode. Moreover, the XPS data were fitted assuming a Gaussian distribution.

In the same UHV chamber was performed the cleanness procedure by ion beam using a 2 keV Ne$^+$ ion beam (spot size about 1 mm^2) produced in a differentially pumped Atomika ion source, and bombarding the sample over an area of 1 cm^2 for several hours. During the process the chemical

composition of sample surface was monitored with XPS measurements; the bombardment was stopped when the percentage of revealed elements do not change.

Sample images were taken by an Olympus microscope (Horiba-Jobyn Yvon) mounting objectives of 10 x, 50 x and 100 x magnification and interfaced with a colour camera.

3.2.1.1.3.   Results on bronze

The chemical composition information on our samples and information on the structure of chemical bonds are obtained with XPS analysis. Survey spectra on as received sample B1 (Fig. 42a) reveal the presence of Cu, Sn and Pb as constitutive elements of bronze and Zn, O and C as impurities (probably C and O are adsorbed from atmosphere while Zn presence is correlated to the bronze growth process). The position of the peaks for all elements is indicated in Table 5 and allows us to identify the chemical bonds between atoms on sample surfaces.

The C1s line on all samples can be described as superposition of two lines centered at about 284 eV (main line of C1s) and 285.6 eV indicating the presence on surface of C-O structures [36].

The Cu 3p3/2 line on B1 and LA cleaned B2 and B3 samples are typical of copper oxide (CuO) [36], while those on samples B2 and B3 treated with HCl are attributed to formation of $CuCl_2$ and Cu_2Cl_2 bonds [36]. Chloride formation is also confirmed by the Cl 2p line position that in the treated samples (before and after LA cleaning) is centered at about 198.2 eV, position that is attributed to Cl 2p in $CuCl_2$ composites [36]. Zn 3p lines are all compatible with the presence on sample surfaces of Zn oxide (ZnO), while the Sn 3d5/2 position is compatible only with the presence of atomic Sn [36]. The patina, as deduced by chemical bonds, occurred between Cu and Cl, is entirely formed by copper chloride $CuCl_2$ and $Cu2Cl_2$.

This patina, that is formed by HCl treatment, introduces on sample a strong presence of Cl, about 23%-24%, as visible in the spectra in Figs. 42c and 3e (for B2 and B3, respectively). In Table 6, we indicated the elements percentage on all samples. After cleaned procedure, the Cl presence is reduced at about 15% in both samples (Figs. 42d and 42f, Table 6).

The cleaning process by ion bombardment strongly reduces the impurities presence and the survey spectrum for B1 cleaned sample shows the constitutive elements Cu, Pb and Sn (Fig. 42b) and strongly reduced percentage of C and O impurities.

Table 5: Peak position for main lines of all elements presents on sample surfaces obtained by a Gaussian analysis of XPS data.

	B1		B2		B3	
	As received	Ion beam cleaned	HCl treated	LA cleaned	HCl treated	LA cleaned
Cu 3p3/2	74.08	74.58	75.03	75.68	75.41	75.61
Sn 3d3/2	482.02	482.58	484.86	484.71	485.16	485.11
Cl 2p	-	-	198.45	198.24	198.16	198.11
Pb 4f7/2	138.51	139.52	139.91	140.02	139.02	138.62
O 1s	529.33	530.91	530.67	529.16	529.12	529.25
C 1s	283.1	284	282.92	283.63	283.68	284.1
Zn 3p	88.78	-	90.52	90.27	89.14	89.42

Table 6: Percentage of each element on all sample surface obtained from XPS analysis

	B1		B2		B3	
	As received	Ion beam cleaned	HCl treated	LA cleaned	HCl treated	LA cleaned
Cu	25.89	75.43	15.88	19.11	17.21	23.55
Sn	0.42	0.61	1.59	1.21	1.47	1.25
Cl	-	-	23.5	15.10	24.52	15.80
Pb	7.19	3.07	1.03	2.18	1.21	2.63
O	7.13	4.9	7.68	8.62	7.06	6.89
C	47.22	14.29	46.89	1.59	38.16	1.47
Zn	12.13	1.68	11.86	6.82	11.61	11.71
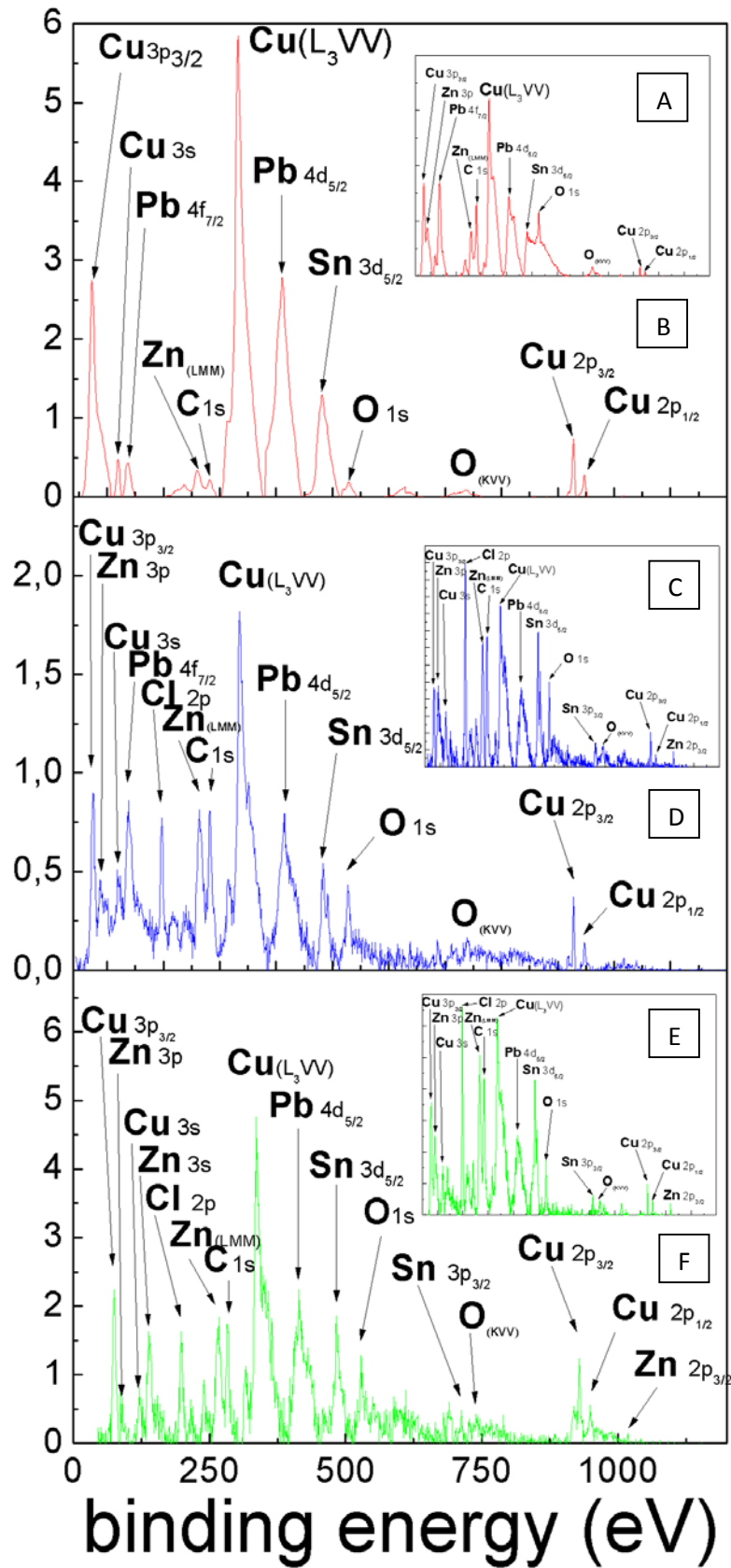
Figure 42: XPS survey spectra for ion bombardment cleaned sample (a), as received sample (b), B2 and B3 samples treated with HCl (c and e), B2 and B3 samples after laser ablation (d and f).

Histograms in Fig. 43 show the relative change of each element in B1, B2 and B3 after the different cleanness procedures. It is clear that the ionic bombardment on as produced sample remove a great percentage of the impurities (C, O, Zn and Pb).

The results obtained by laser ablation in air and in marine water are very different. In both situation laser ablation removes the bronze disease patina, as can be observed by decreases of Cl concentration, and Zn impurities. Moreover, optical images of HCl treated samples show as the presence of the gray patina of dimensions of about 300 μm disappears in cleaned samples (Figs. 40b-40d). Furthermore, the results reported in the histogram indicates that LA in air favorites the absorbance of carbon and oxygen from atmosphere and a progressive "carbonization" of surface with the formation of C-O patina on surface.
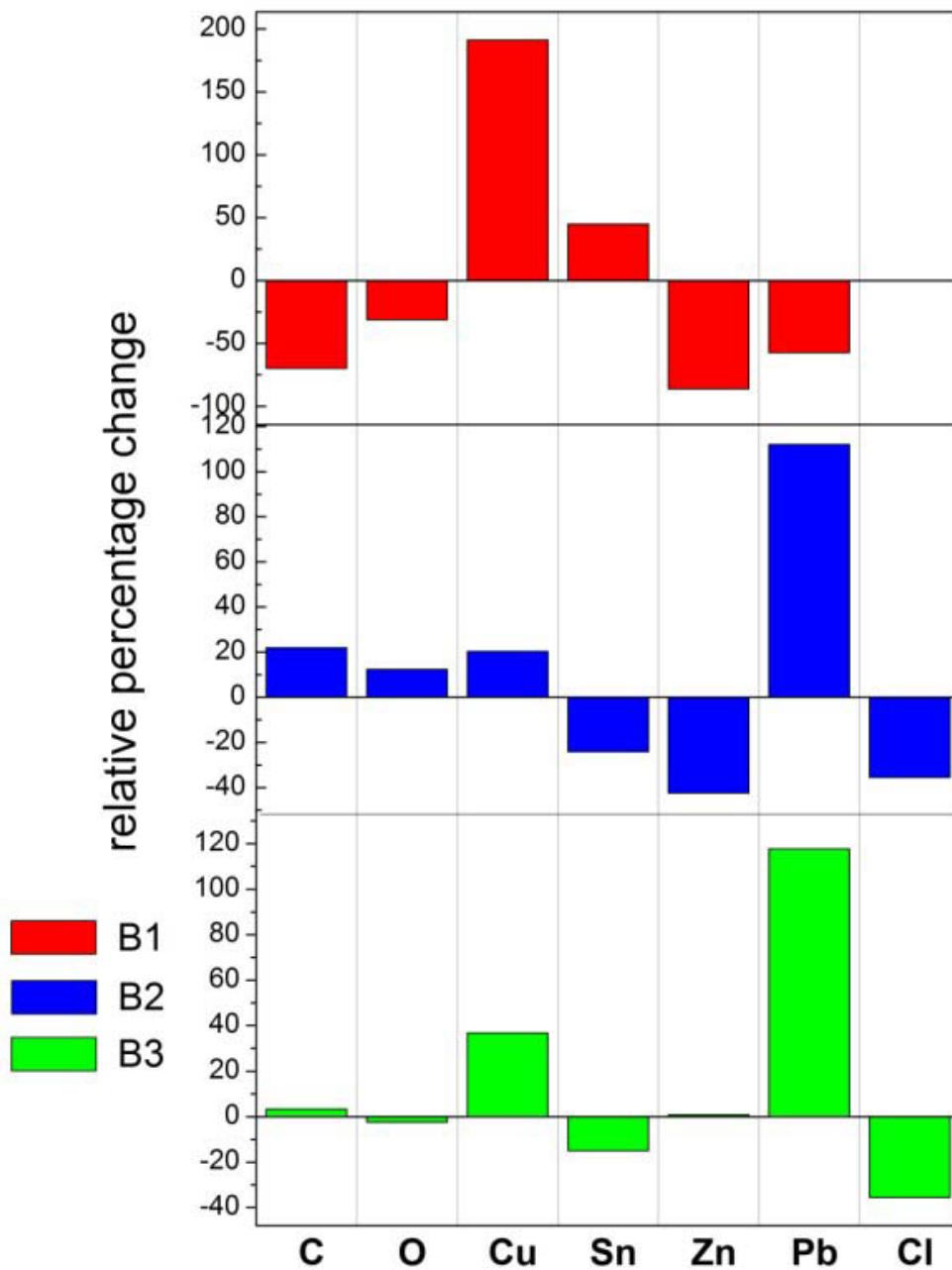
Figure 43: Relative changes for all elements in B1, B2 and B3 samples.

In marine water, besides, the laser ablation cleanness is most effective and we do not observe adsorption of oxygen or carbon. The formation of C-O patina in air can also, explain the different change of Zn impurities in B2 and B3 samples. In fact, ZnO impurities are removed from sample in air but remain unchanged in water. We hypothesize that in air, the progressive "carbonization" of surface absorbs the air oxygen and that present on sample, breaking the ZnO molecules, and so the Zn atoms are easier removed by LA. Pb impurities apparently increase in both B2 and B3 samples. We hypothesize that laser ablation is not able to eliminate Pb. The Pb visibility is increased in cleaned samples because of the patina reduction.

3.2.1.2.   Analysis on Quintilii's Villa bronzes

The aim of diagnostic tests is the study of artefact construction technique and execution, providing information about the original materials, their preservation state and on alteration products present on the artefact. Usually, the study of material surface is performed by different electron and/or photonic spectroscopies. The analysed object is "bombarded" with particles or electromagnetic radiation to obtain chemical and morphological information on the first monolayer or on the first surface layers (depth of few microns). The analysis of artefacts surface is important because it is the interface with the external environment and then it represents the border layer for the object (e.g., oxide film on a metallic material).

Moreover, the surface may affect the aesthetic appearance and can reveal the products of degradation (e.g., bronze disease). So, the surface characterization becomes crucial where the interaction phenomena with the external environment modify the artefacts. Moreover, the characterization of corroded layers is important to explain the causes of the degradation process.

Bronze patinas, in fact, are generally associated with the thin layer of products observed on ancient metals and alloys. They can result from corrosion due to exposure to atmospheric agents or to a prolonged burial in the soil (as in the case of the analysed artefacts). Furthermore, alterations and patinas are strongly dependent on environments so that even external small changes can affect patina formation [41].

For all these reasons, the studies of patinas are very important to estimate factors in bronze stabilization. Below, a detailed examination of alloy composition and corrosion of three Roman bronzes from Villa of the Quintilii excavation is described.

Historical "bronzes" are highly variable in composition; usually they contain a mixture of copper and tin as main components and traces of various elements as impurities (zinc, lead, nickel, iron, antimony, arsenic, and silver). We focus our attention exclusively on copper and its deterioration mechanism, because this element is the main component of bronze disease [41].

The samples analysis was obtained by SEM microscopy, EDX (Energy Dispersive X-ray spectroscopy), AES (Auger electron spectroscopy), FT-IR (Infrared Fourier transform), and Raman spectroscopies. All the performed investigations were non-destructive and non-invasive and have been taken on as received and cleaned samples.

The cleaning process was obtained by sulphuric acid treatment (H_2SO_4 aqueous solution 10%) for 10 minutes to dissolve copper carbonates.

3.2.1.2.1. Historical background

The samples have been found in an archaeological excavation at the Quintilii's Villa (Fig. 44). This villa is located south of Rome and it is considered the largest and most luxurious suburban villa of the second century after Christ. The area covers 24 hectares and is rich in monumental remains. The name derives from Quintilii brothers, noble roman consuls, during 151 BC. The site is so large and the ruins so extended that in the past it was thought to even be a city to which, for this reason, was given the name "Old Rome". The fragments show a bad state of conservation (Fig. 45), which is evident different processes of corrosion have caused material loss and chromatic alteration.
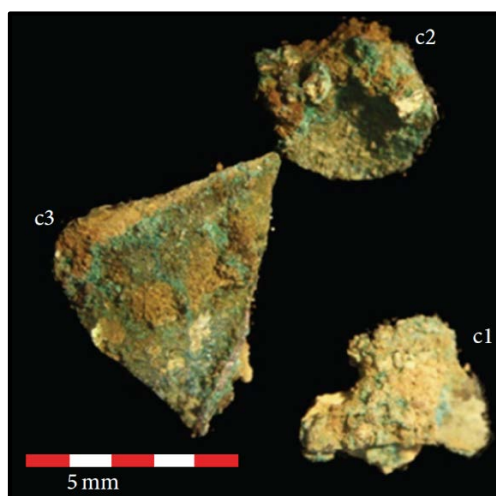

Figure 44: Quintilii's Villa

Figure 45: bronze samples

3.2.1.2.2. SEM-EDX analysis on Quintilii's Villa bronzes

Using non-invasive and non-destructive techniques, the fragments have been studied by surface analysis investigations to provide information on the chemical composition of the material and its alterations.

Morphological analysis was performed by SEM and optical microscopies. Optical images of the sample were obtained by a zoom Stereomicroscope, model SZH Olympus, mounting objectives from6x to 9x.The fragment dimensions range from 7 to 4 mm, with a thickness of about 3mm (Fig. 45). SEM analysis was performed on both faces of our bronze fragments. The samples, being metal alloy fragments, have not been metallized.

SEM images of the samples were acquired with a focused beam of electrons and magnification of about 500,000x. When a sample is bombarded by an electron beam, as already mentioned, it produces secondary electrons (SE), back-scattered electrons (BSE), and characteristic X-rays. The produced electrons interact with atoms in the samples generating electronic signals, which give us information about the sample's chemical composition (BSE and characteristic X-rays) and the surface topography (SE).

EDX analysis and SEM images have been obtained simultaneously with a 20 keV electron beam and a current of 200 pA (the best compromise for a good statistics in reasonable time and without saturate the detector EDX).Was chosen a magnification of 2500x (in most cases selecting a 500 μm × 500 μm frame) and integration time of 100 s. We acquired images using SEM microscope both in secondary electron mode (SE) and in back-scattered electron mode (BSE).

3.2.1.2.3. Auger Electron Spectroscopy (AES) on Quintilii's Villa bronzes

Chemical information was obtained also by Auger electron spectroscopy (AES). This analysis was performed in an ultrahigh vacuum (UHV) equipped for standard surface analysis with a pressure in the range of 10^{-9} torr, bombarding the bronze artefact by a 2500 eV electron beam to a single incidence angle with respect to the normal sample surface.

The electrons emitted as a result of the bombardment are detected by an electrostatic analyser (EA) fixed having acceptance to 80°.

AES is a spectroscopy used in the study of surfaces and gives chemical information on the first monolayers.

The Auger spectroscopy is not widely used in the field of cultural heritage, and in particular on bronzes. Indeed, since the middle of the 19th century, these materials have mostly been studied with "conventional" methods, such as optical microscopy, wet chemical analysis, atomic absorption spectrometry, and so forth. This spectroscopy is based on the analysis of energetic electrons emitted from an excited atom after a series of internal relaxation events (Auger effect) caused by an electron bombardment of sample surface [41].

3.2.1.2.4. FT-IR (Infrared Fourier transform) on Quintilii's Villa bronzes

To get the most useful information on degradation products and surface alteration and to discriminate the type of patina, we used two of the most accurate and sensitive molecular spectroscopic techniques. One of these is the Fourier Transform Infrared Spectroscopy (FT-IR). FTIR is a technique usually employed to obtain information about molecular structures, functional groups, and chemical compounds on sample. The technique is based on the irradiation of sample surfaces with an electromagnetic radiation, which ranges between 4000 and 400 cm−1 and then measuring the absorbed fraction to determine the vibrational transitions of the sample molecules [41]. The FT-IR is based on the possibility to realize a Fourier transform of emitted signals. The used device is a 100 FT-IR Perkin-Elmer spectrometer.

3.2.1.2.5. Raman analysis on Quintilii's Villa Bronzes

Another molecular spectroscopic technique in the Raman spectroscopy.
Raman microscopy is a spectroscopic technique used to observe vibrational, rotational, and other low-frequency modes in a system. It provides information on the atom vibrations in a crystal lattice studying the inelastic and Raman scattering of a monochromatic light (usually a laser in the visible range). The laser light interacts with molecular vibrations, phonons, or other excitations in the system, and the produced shift in energy gives information about the vibrational modes in the system [41]. The Raman system in this work is a DXR Raman Microscope from Thermo Scientific.

3.2.1.2.6. Results on Quintilii's Villa Bronzes

EDX analysis (Figure 46b) for all "as received" samples (SEM images in Figure 46a) indicates the following as chemical composition: silver, aluminium, gold, calcium, chlorine, copper, iron, potassium, magnesium, phosphorus, and silicon.

Table 7 summarizes all elements' percentage (excluding C) on the various areas of the samples subjected to EDX analysis.
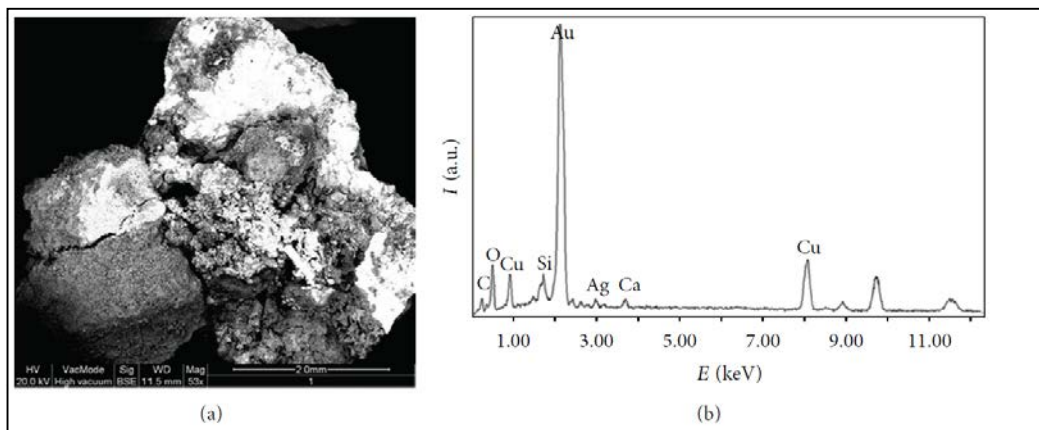
Figure 46: (a) BSE image of a bronze fragment and (b) bronze EDX spectrum.

	Ag	Au	O	Mg	Al	Cl	Si	P	K	Ca	Fe	Cu	tot
1 dx	—	—	53.69	0.91	7.26	—	12.60	1.56	0.66	7.61	1.96	13.75	100.00
1 sx	—	—	48.07	2.39	6.40	—	18.02	—	0.96	17.76	4.35	2.00	100.00
1 up	1.81	65.63	8.26	—	—	—	1.43	—	—	0.97	—	21.90	100.00
2 down	—	—	66.17	1.39	3.86	—	20.69	1.04	—	1.75	0.91	4.19	100.00
2 sx	—	—	56.66	—	3.15	—	16.59	1.50	—	1.75	1.14	19.21	100.00
2 up	1.72	57.28	13.69	—	0.32	3.63	1.02	—	—	0.36	—	21.98	100.00
3 rc	0.40	—	38.81	—	2.71	0.93	11.06	1.33	—	2.16	1.16	41.44	100.00
3 r	4.37	76.82	3.61	—	—	—	2.23	—	—	0.77	—	12.20	100.00

Table 7: Elements percentages in the sample for the different areas analysed.

Figure 47 shows the AES spectra for all elements on as received sample. In the spectrum in Figure 47(a) we observe the Au line centred at 69.80eV (the detail of Au line is shown in Figure 47b) and the C (271 eV) and O (503 eV) lines [42]. In Figure 47c we observe the characteristic lines of tin dioxide, respectively, at 421.5, 425.5, and 432.6 eV (Sn is one component in a bronze alloy) [42].
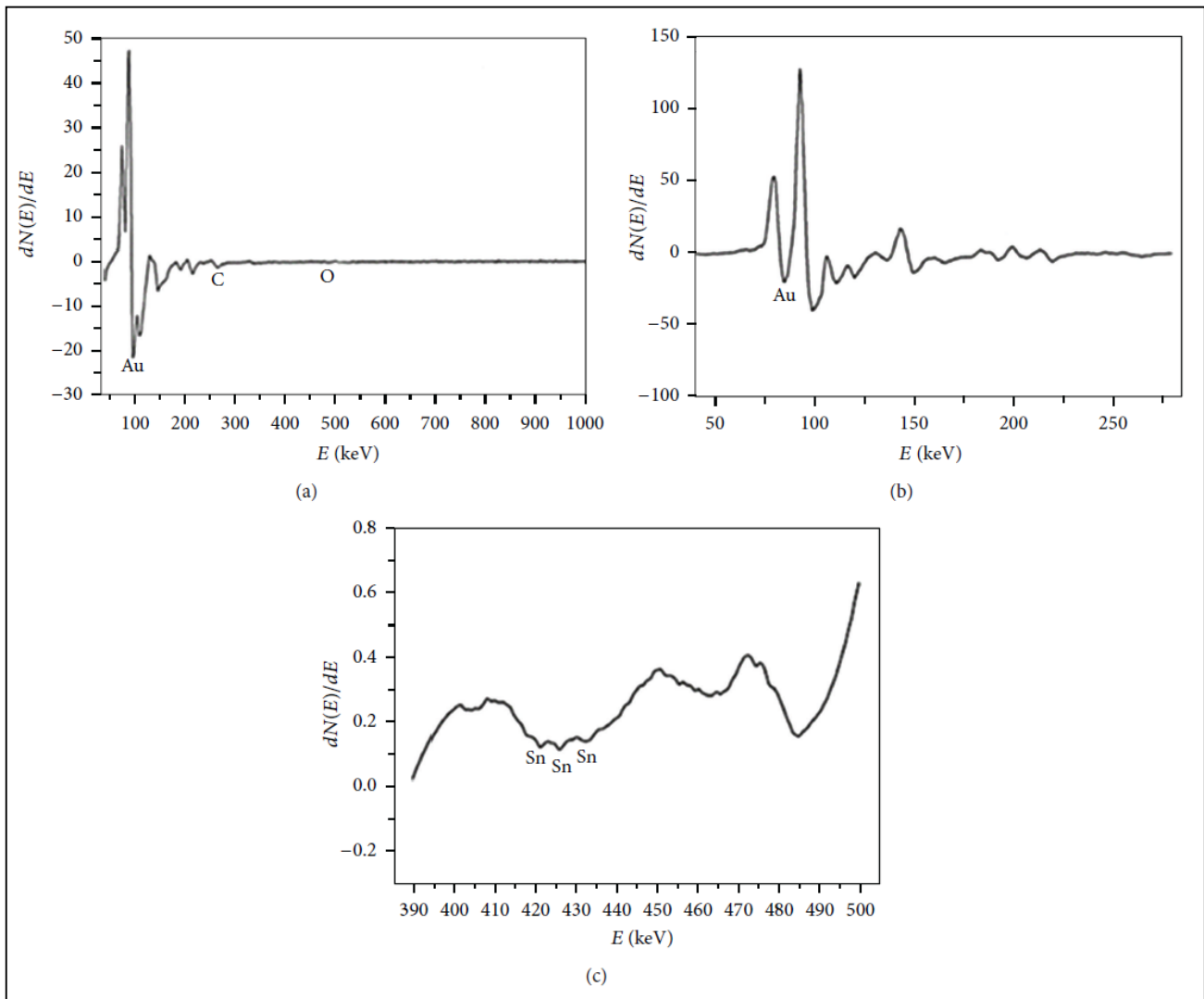
Figure 47:(a) Bronze Auger spectrum, (b) Au Auger spectrum, and (c) Sn Auger spectrum.

FT-IR spectrum in Figure 48a shows the malachite [Cu_2 (CO_3) $(OH)_2$] characteristic bands. The FT-IR absorption spectrum of malachite shows bands at 784, 818, 873, 1047, 1099, 1395, 1494, 3330, and 3406 cm^{-1} [43].The band at 3330 cm^{-1} is characteristic of stretching functional –OH group [43]. The bands at 1494 and 1395 cm^{-1} are characteristic of the stretching –CO_3 group [43]. We see that in the CO_3 group there is a double bond C=O. Probably the band at 1635cm^{-1} was due to stretching of the bond C=O [43]. The bands at 873, 818, 777, and 749 cm^{-1}, shown in Figure 48b, represent the malachite fingerprint region [43]. Instead, the band at 1003 cm^{-1} is related to the asymmetrical stretching of the Si–O–Si [43]. The band at 912 cm^{-1} is due to Si–O bond stretching [43].
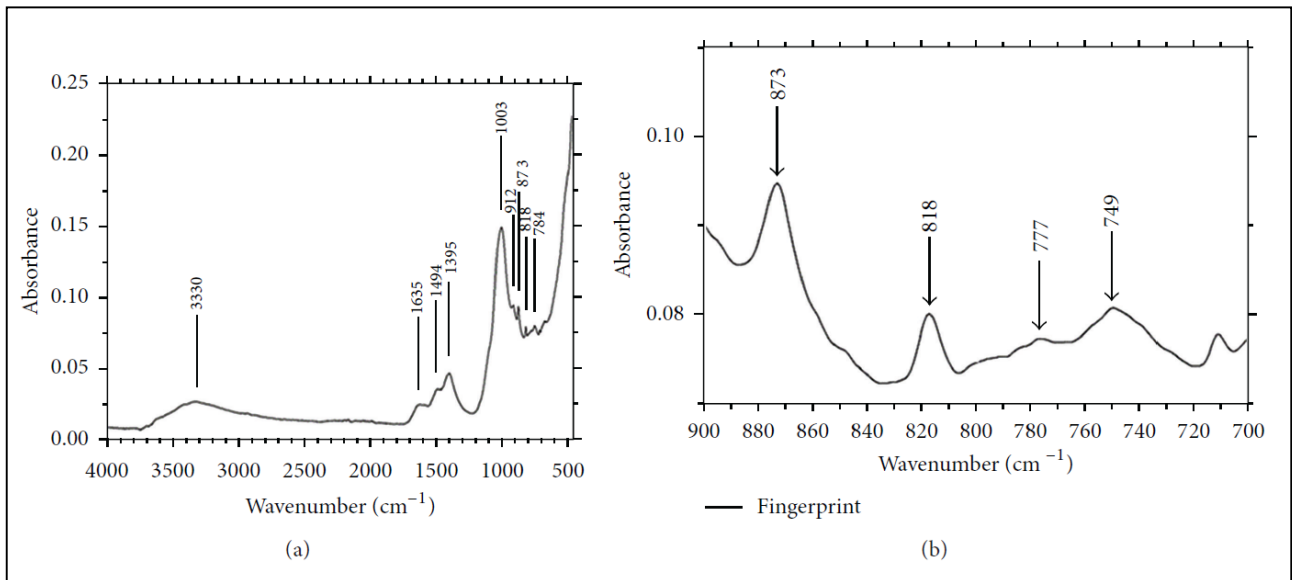
Figure 48: (a) Malachite FT-IR spectrum and (b) fingerprint region of malachite.

The Raman analysis confirmed the FTIR results. In fact, the spectral pattern is typical of malachite (Fig. 49a); the spectrum shows peaks at 177, 216, and 267 cm^{-1}, which are related to O−Cu−OH bond bending. The mode at 354 cm^{-1} is due to the Cu−O bending. Modes at 432 and 533 cm^{-1} are related to the Cu−O stretching [44].

The modes at 1060 and 3350 cm^{-1} are related to the OH bond stretching, while those at 1486 and 1087 cm^{-1} are related to the anion carbonate CO_3^{2-} stretching [44]. In a second spectrum taken from another region on the sample (Fig. 49b), it is possible to see the most intense bands at 130, 188, 230, 351, 404, and 984 cm^{-1}. These bands are characteristic of connellite $Cu_{19}Cl_4(SO_4)(OH)_{32}\cdot3(H_2O)$ [44].The connellite is a copper chlorosulphate that is very rare in nature, which should turn to blue. It comes in the form of tufts of acicular crystals very delicate and is often associated with other secondary copper compounds, such as cuprite and malachite. Connellite can be classified as one of the bronze diseases.
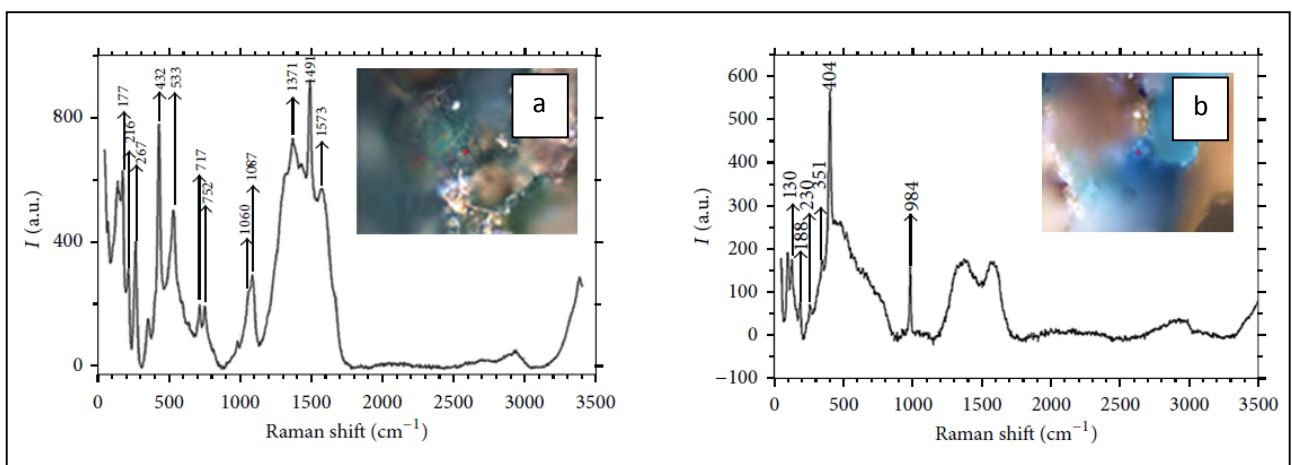
Figure 49: (a) Malachite Raman spectrum and (b) Connellite Raman spectrum.

The analysis on cleaned samples investigated the presence of gold on the alloy as suggested by the gilding visible, after patina removal (Fig. 50).

From the SEM images of sample c3, in Figure 51, we observe that gold is distributed on the surface to forma thin film separated from the bronze alloy. The film thickness varies from about 200 nm to 400 nm. In effect, in the Roman era, major bronze statues generally underwent a gilding process with application of thin gold film on the artefact [38]. Figure 52 shows the presence of cracks in the sample section caused by removal of carbonates (present in soil and in malachite) during acid treatment.

We can get more information about the sample's structure from the c2 cross section in Figure 51. There are four different structures, identified by the letters A, B, C, and D. As shown in Table 8, the different structures have a different chemical composition. In addition, the gold covers the entire alloy surface (A) with a small amount of Ag. On the gold coating (zone B), there is a patina formed predominantly of Cu, O, Cl, and S, while in the intermediate zone (C) the higher element is the copper with a small amount of O, S, and Cl which form a patina with a morphological structure clearly different with respect to other layers.

In the innermost zone, indicated with the letter D, the composition is predominantly similar to the B and C regions with contamination of Ca, Fe, and Si (the percentage values of all elements in all regions are given in Table 8).

The X-ray fluorescence analysis was conducted with a portable XRF model Artax 400 of Bruker and they were taken into different points of sample surfaces (as indicated in Figure 51)
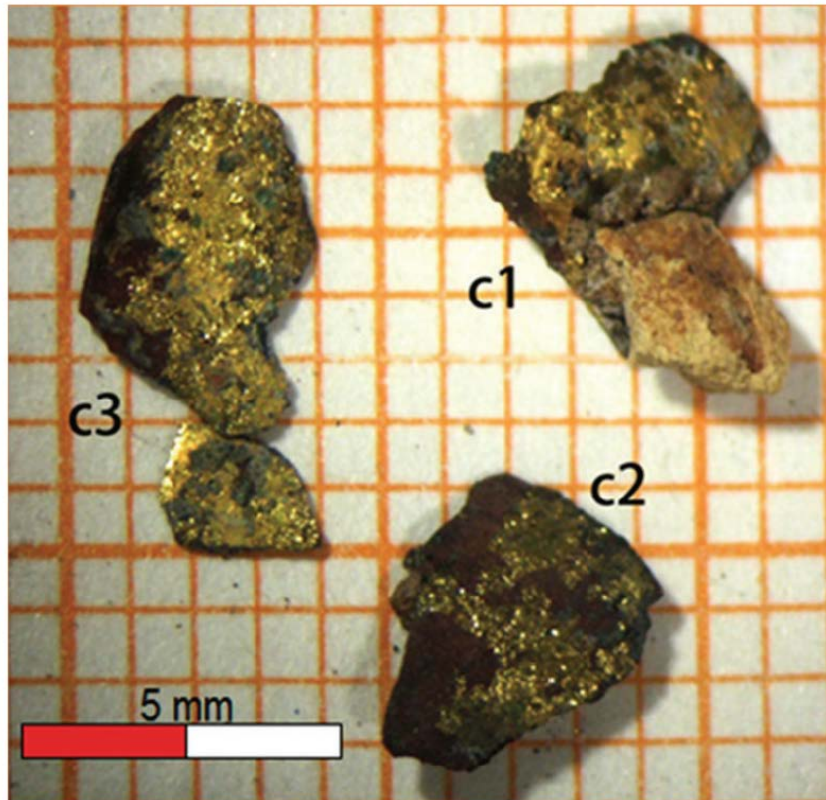
Figure 50: Bronzes after acid treatment.
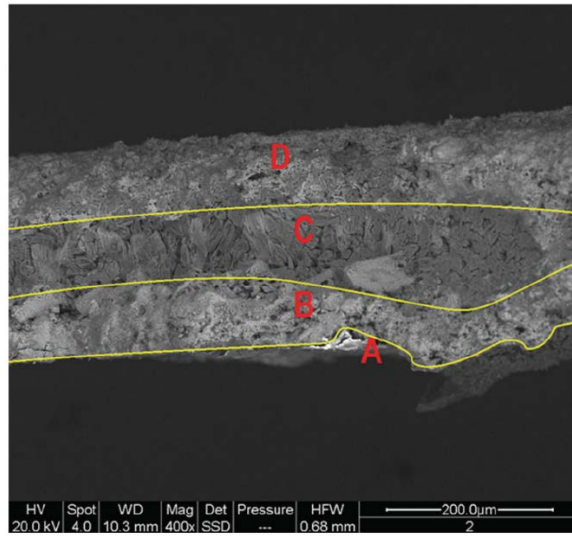
Figure 51: SEM image of bronze c2 cross section.
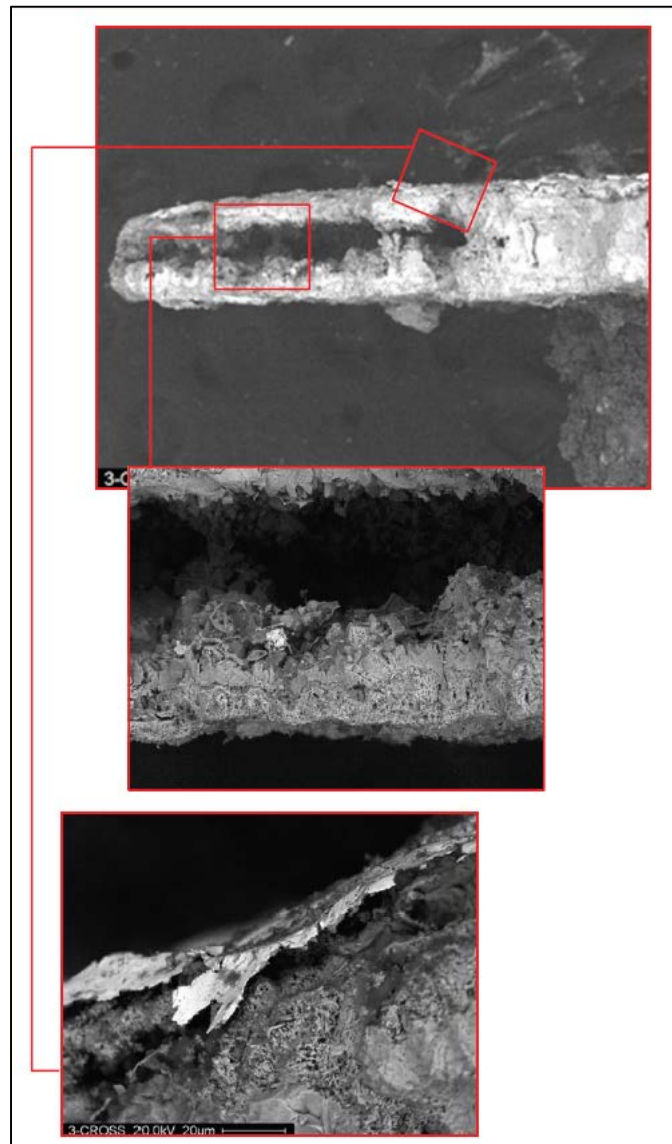
Figure 52: SEM image of bronze c3 cross section.

	Ag	Au	Ca	Cl	Cu	Fe	O	S	Si	tot
A	0.17	3.71	—	—	0.18	—	0.14	—	—	100.00
B	—	—	—	0.34	2.53	—	1.04	0.31	—	100.00
C	—	—	—	0.13	81.68	—	0.44	0.23	—	100.00
D	—	—	0.04	0.59	48.74	0.00	1.17	0.13	0.14	100.00

Table 8: Elements percentages in the sample c2 for the different zones analysed.

3.3. Artificial stone materials

In this thesis have been taken into account several artificial stone artefacts. In particular, attention has focused on ceramics.

3.3.1. Ceramics in cultural heritage

Archaeologists spend time trying to retrieve the fragments and testimonies of culture left behind by ancient societies. Some of these fragments may be particularly useful for reconstructing the history of the past. Ceramics can be used to determine a person's social rank, gender, or maybe even their relationship with others in the group. Archaeologists use ceramics and drawings placed on it to crack as they have been used in various areas of the site. For example, one would expect to find pottery in a food preparation or cooking, but you would not expect to find in a bedroom.

Archaeometry is useful for understand manufacture and origin of the ceramic artifact, thanks to the technique of thermoluminescence is possible to date the artifact.

It is well known that many archaeological finds come from terrestrial archaeological sites but many others come from underwater sites. Like on every archaeological artifacts is possible to find an infinite number of crusts and patinas of various kinds. Then, once again, a very important problem is the cleaning of the ceramic surface.

3.3.1.1.   Experiments on Carosello

In the last decades, the laser ablation (LA) techniques have shown an excellent alternative to organic solvent in the treatment of metallic surface and in conservation and restoration of cultural heritage [45]. The scientific investigations have focused on the efficiency, selectivity and efficacy of laser ablation, as well as on the possible advantages that it can provide with respect to traditional cleaning techniques.

3.3.1.1.1.   LA on Carosello

The main problem in the use of laser ablation cleaning on ceramic and stone is the possibility of removing protective layers, decorative elements and graffiti from stones. This problem can be solved varying the laser parameters during the ablation. In particular, we present in this work a study of ability to laser ablation to remove only the impurity patina without change the artifact surface. The laser ablation cleaning was applied on artifact "Carosello" and monitored by X-ray photoelectron spectroscopy (XPS) and Photoluminescence (PL).

The "Carosello" (Fig. 53a) is a structural hollow element made of clay, placed in arches, in domes or even in the walls of buildings such as churches and houses, with the function lighten the structures. The "Carosello" objects of this study come from a site in Calabria: the Sanctuary of "Madonna del Buonconsiglio" in san Giacomo di Cerzeto, Cosenza, Italy dated back to 1,844 ± 11 [46].

The experiments were conducted on a series of Carosello fragments with dimensions of about 1 cm × 2 cm and a thickness of about 1 cm. Fig. 53 shows the optical images of an as received (B) and an ablated fragments (C).
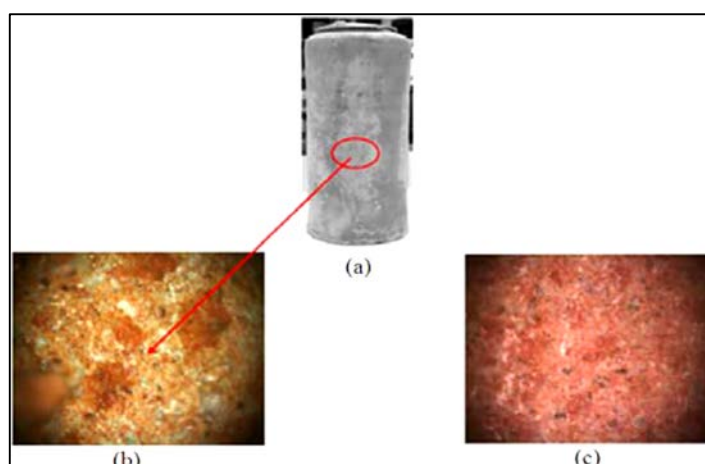
Figure 53: Images of Carosello (a) and optical images of fragments before (b) and after (c) laser ablation.

Each sample was subjected to cleaning procedure by laser ablation in air.

3.3.1.1.2. XPS and PL analysis on Carosello

XPS and PL measurements were taken following the same procedure and the same parameters as described in the experimental section

3.3.1.1.3. Results on Carosello

Optical images of sample surfaces in Fig. 53b clearly indicate that the as received "Carosello" is covered by an impurity patina non homogeneous for structure and compositions which disappears after ablation (Fig. 53c), as also indicated by the results of XPS and PL characterization.

The chemical composition information on our samples and information on the structure of chemical bonds are obtained with XPS analysis. Survey spectra on as received sample (Fig. 54 top) relives the presence on sample surface of Si, Al, Mg, S, P, Cl, C, Ca, O and F.

After LA process, the spectra (Fig. 54 bottom) indicate the absence of Mg and P and a substantial decreases in percentage of O and F.
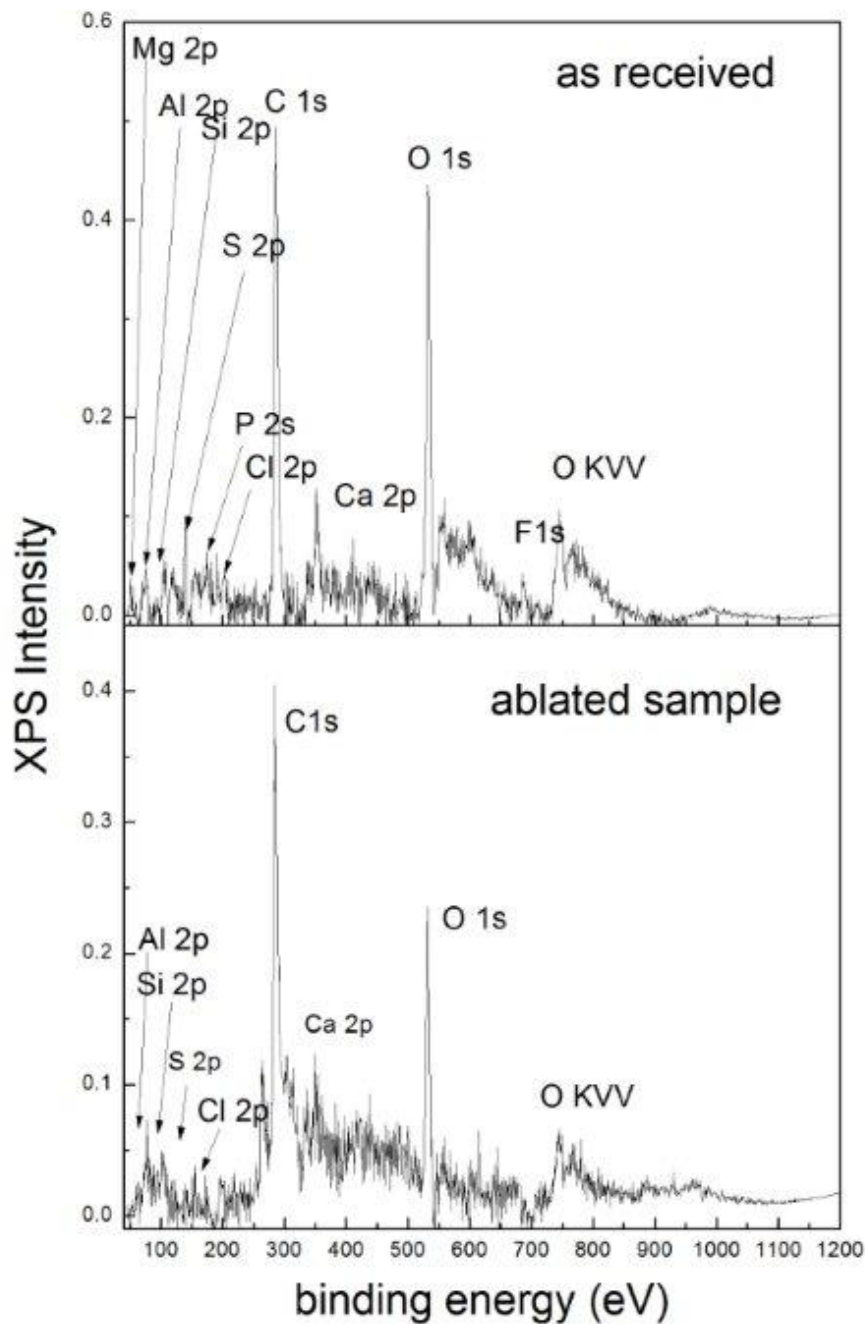
Figure 54: XPS survey spectra of as (a) received and (b) ablated fragments.

Histogram of Fig. 55 shows the relative change of each elements in fragments. It is clear that laser ablation remove completely the impurities of Mg, P and F allowing a most effective XPS visibility of constitutive elements (Al, Si, S and Cl) and causing a decrease in oxygen percentage. The hypothesis is that LA remove the oxygen adsorbed from atmosphere without destroying the constitutive oxygen in SiO_2 bonds. The amounts of C and Ca is almost unchanged indicating the inability of LA to remove those elements that are probably inserted in the bulk during the growth process.
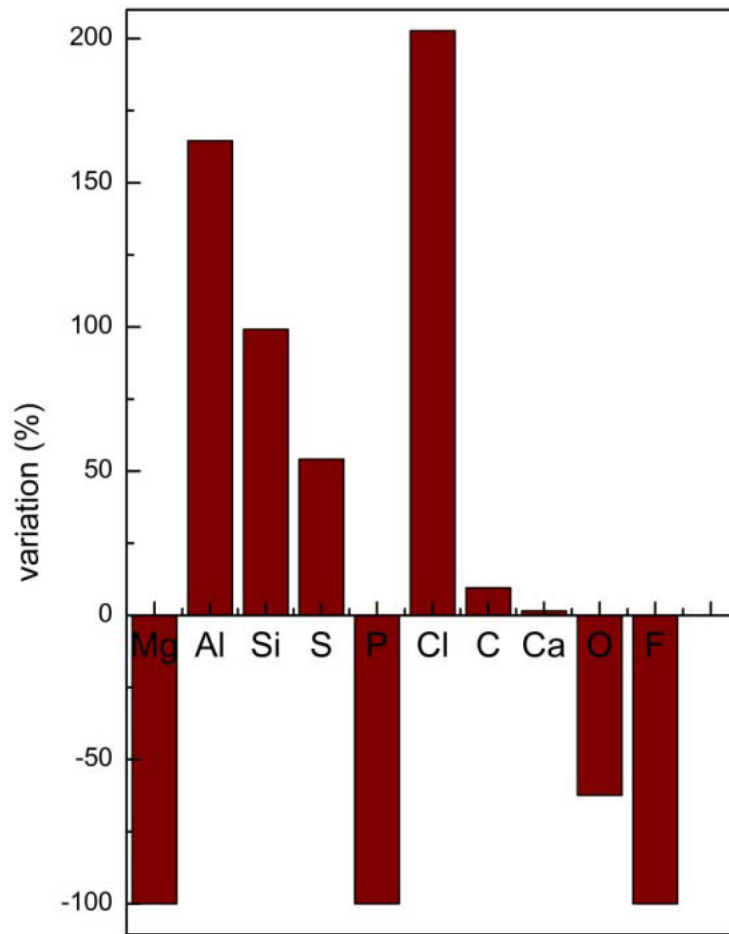
Figure 55: Relative changes for all elements in ablated fragment.

The position of main lines for each elements, indicated in Table 9, specifies the formation, on sample surface, of different oxides and composites [34].

	As recevied sample	Ablated sample
Al 2p	75.6	75.4
C 1s	285.84	285.65
Ca 2p	351.99	351.14
Cl 2p	199.79	199.43
F 1s	688.36	
Mg 2p	51.56	
O 1s	533.01	533.08
P 2s	191.6	
S 2p	173.8	172.6
Si 2p	199.8	199.43

Table 9: XPS main line positions (eV) for all elements on sample surface.

Si 2p and O 1s lines are very close to these associated to SiO₂ confirming that the quartz is the main components of "Carosello". Almost all the impurities are aggregated in oxides (Al_2O_3, CaO, P_2O_5 and MgO) while Cl and F are aggregated in composites with Al (AlF and AlCl) [36]. The carbon absorbed on sample surface is primarily bonded with oxygen to form C-O bonds, as suggested by the only presence of lines at about 285 eV [36]. The LA processes do not change the chemical bonds between elements; in fact, we observed an unchanged line position after LA. This confirms the ability of LA to remove the impurities without changes the chemical composition (elements and their bonds) which can lead important historical and artisitical information on ceramic artifact (grown techniques, place of origin, storage conditions, colors and decorations). The information on LA effectiveness on surface cleaning is also indicated by the PL results. PL spectra taken from as received and ablated samples (Fig. 56) indicated an increases of PL intensity in ablated sample of about 96% while the signal shape is unchanged (see normalized spectra in the inset in Fig. 56).
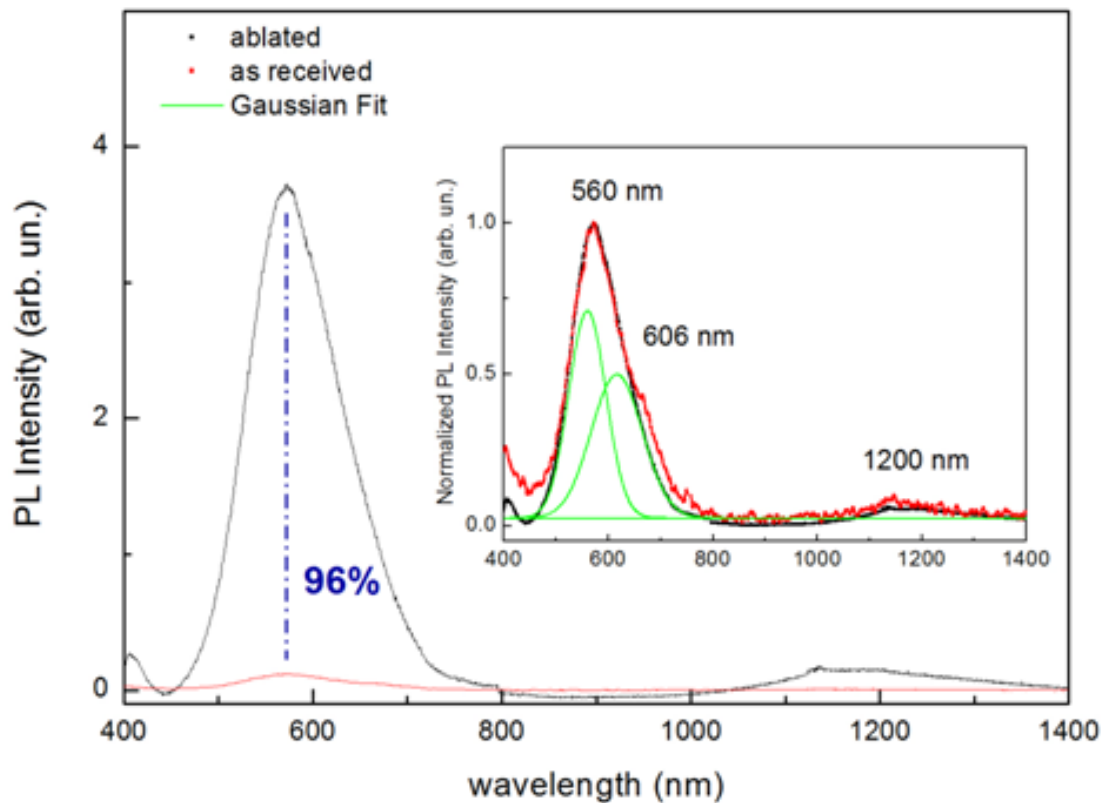
Figure 56: Photoluminescence spectra from Carosello surface before and after LA. Inset: Gaussian analysis of normalized PL spectra.

Both as received and ablated sample are characterized by a luminescence signal that, after a Gaussian analysis reveals three main bands at 560, 606 and 1200 nm. All these lines can be attributed to quartz (SiO₂) in "Carosello". In particular, the bands at 560 and 606 nm are both typical of quartz and are intrinsic of bulk structure [47], while the 1200 nm band is related to the presence of defects of interstitial oxygen in SiO2 bulk [47]. The lowest intensities of as received samples is caused by the impurities presence that covered the surface limiting the interaction by UV light and quartz in the

bulk. LA, removing the surface patina of impurities consents an optimal interaction between UV-laser light and quartz causing an exponential increases of PL intensity. The absence of changes in PL shape indicates, also, that the LA effects are limited to remove the impurities without to change the sample surfaces.

Moreover, the removal of shallow impurities and the absence of changes in chemical structures as indicated by PL and XPS results, point out that the LA process is limited to the ceramic surfaces. The bulk of artifacts is so unchanged and can be used to the other diagnostic process (chemical, physical and artistic analysis). Furthermore, LA cleaning process do not causes heating of samples that can affect the thermo-luminescence dating process. The temperature registered on sample surface during laser ablation over the entire surface of the carousel is less minus than 120 °C (about 115 °C on the surface exposed to laser beam and 65 °C on these opposite) so that the bulk quartzes can be used in dating process without introducing mistakes.

3.3.1.2.   Experiments on Neolithic Ceramics

Conventional methods in conservation are based on mechanical and chemical compound treatments. Mechanical cleaning is the most controllable method without introduction of chemical impurities into the artifact. However, this technique is applicable only in few cases because of damages that it can produce on artifacts. In fact, the mechanical removal of encrustation by mechanical instruments and abrasive particles can scratch the surface artifacts [48]. In recent years, scientific investigation has led to the study of new technologies applied to cultural heritage [48].

In this framework contactless methods, that do not damage the objects integrity, assume a strong importance. Among them, the laser methods are dominant.

Neolithic Sample (TOR, Figure 57) is found in the archeological excavation, "Piana di Curinga" (Lamezia Terme, CZ, South Italy), dating back to the IV millennium B. C. [48]. The Neolithic finding is an impressed ceramic and, in the first analysis, it appears made by a dark brown mixture and by a clay with several impurities; it belongs to the artistic culture of "Stentinello".

The "Stentinello" culture represents an evolution peculiar of the Neolithic culture of decorative techniques, during the diffusion of the Neolithic in the Southern Italy [48]. As well known, ceramic is a material composed by sedimentary rocks, clay and debris of variable mineralogical composition (as quartz, feldspar, calcium carbonates, oxides and hydroxides of iron and other minors as well as in organic matter and other various random materials) [48].

Figure 57: Neolithic sample (TOR).

3.3.1.2.1. LA on Neolithic Ceramics

The objective of this work is the study of the LA effects on the TL dating by monitoring the temperature of ceramic samples during the entire irradiation process and by the dating of the ceramic before and after LA.
The cleaning process of all pottery surface was obtained by LA, in order to detect the possible influence of LA on the intensity of the natural thermoluminescence (NTL) signal. In fact, LA was conducted in dark conditions and the TL measurement was taken before and after cleaning process.
The LA was conducted with an irradiation time of 30 minutes. The possible influence of the LA on the intensity natural of the thermoluminescence was verified monitoring the temperature of ceramic samples during the entire irradiation with the laser beam. The temperature was measured by a J-type thermocouple installed in a cavity in the ceramics (Figure 58) obtained in the front of laser beam and at a depth usually used for TL sample taking (few millimeters over ceramic surfaces).
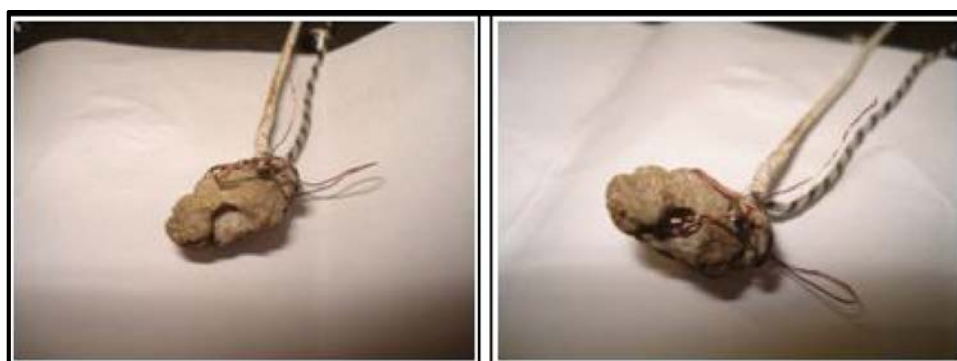
Figure 58: J-type thermocouple installed in the cavity of material recovery for TL.

3.3.1.2.2. Thermoluminescence (TL) on Neolithic Ceramics

The LA techniques has a serious inconvenience that laser irradiation heats locally the surface artifacts and this can cause the impossibility of thermoluminescence (TL) dating after restoration. TL is, in fact, a technique, which date materials starting from a heating at about 300˚C [48]. Indeed, TL allows dating pottery or terracotta from the study of luminescence signals emitted by their crystalline components, such as quartz or feldspars, therefore this luminescence emission is quenched by a heating at temperature greater than 250˚C (temperature of bleaching of metastable traps in minerals) [48].
TL is a technique that allows us to dating pottery or terracotta, by analyzing the luminescence signals obtained heating the quartz and/or feldspar content in the samples. The artefact, after the last heating in the oven, begins again to accumulate a certain amount of absorbed dose ("*Equivalent dose*") due to the natural radiation coming from the ceramic itself (U, Th, K-40) and from the surrounding environmental gamma rays plus cosmic

radiation. The subsequent heating to high temperatures in laboratory, results in the release of the light corresponding to the dose accumulated over time.

From light emitted study, it is possible to calculate the time elapsed since the original heating in the oven, according to the equation age expressed in years:

$$Age = \frac{Equivalent\ Dose(Gy)}{Annual\ Dose(Gy\ year)}$$

Where, the "Annual dose (AD)" (Gy per years) is the annual natural radiation and "Equivalent dose (ED)" is the dose adsorbed by crystal in Gray (Gy).

The Neolithic artifact (see Figure 57) is dated by a Single Aliquot Regenerative-dose protocol, SAR [48], and the obtained results will be compared with the historical data, to confirm the authenticity and to classify the findings [48]. In the SAR protocol are monitored, and corrected sensitivity changes caused by heat, optical stimulation and laboratory beta irradiation [49]. The procedure based on a SAR has the advantage, over the traditional methods (Multiple Aliquot Additive Dose, MAAD), of avoiding standardization or sensitivity problems and reduces the effort required in sample preparation.

In fact, the single-aliquot procedures is preferred over multiple-aliquot procedures in light of their higher accuracy and mostly for the absence of any need for normalisation.

Nowadays, for quartz the single-aliquot regenerative-dose (SAR) protocol is a standard procedure for equivalent dose determination.

In a regenerative-dose procedure, the equivalent dose is determined using a range of regenerative doses, which encompass the natural dose. The sample is bleached completely during measurement of the luminescence signal. By taking the ratio of the natural and regenerative IRSL responses to the subsequent test dose IRSL responses, a sensitivity corrected measure of the IRSL response is obtained. Usually, in the protocol proposed here the IRSL signal is measured during stimulation for 100 s at 50°C. The signal used is the IRSL detected in the initial 0.8 s of measurement. From this, a background signal is subtracted based on the average IRSL observed in the last 10 s of stimulation. For the test dose measurement, the background signal based on the signal over the last 10 s of the previous measurement is subtracted from the initial signal [49].

Sample preparation took place in condition of darkness with the aid of a single soft red light (>600 nm). We have chosen the Quartz inclusion technique, since with this method we obtain grains of larger size that can then be submitted to acid solution to eliminate surface carbonates.

The first step of preparation involved sampling (using a low speed drill) in the sample bulk, in order to avoid external contamination, such as, sources of light mostly, heat or radiation to which the sample surfaces may have been exposed after the discovery.

Grain size 63 - 125 μm was sieved and treated with 10% HCl to eliminate any present carbonates and bath with 30% H_2O_2 to eliminate organic material. The so obtained different crystalline fractions were separated by using a heavy liquid solution.

The quartz grains were then extracted, dried and used for the dating process. These grains were fixed with silicone oil on stainless steel discs of 9.7 mm in diameter and then loaded on the spectrometer [48].

The dating has been obtained via thermoluminescence measurements using a TL reader from Risø TL/OSLDA-20, by applying the SAR protocol. For the artificial doses we use a beta source (90Sr) characterized by a dose rate of 0.1 Gy/sec. Generally, we used a heating rate of 5°C/s up to a temperature of 450°C and the samples were irradiated with ten regeneration doses.

The standard Photo Multiplier Tube (PMT) in the Risø TL/OSL reader is a bialkali EMI 9235QB PMT, which has maximum detection efficiency between 200 and 400 nm, making it suitable for detection of luminescence from both quartz and feldspar. The Risø TL/OSL reader used with the following detection filter: Hoya U-340 (7.5 mm thick, diameter Ø = 45 mm).

3.3.1.2.3. Results on Neolithic Ceramics

The determined Equivalent doses (ED) of the Neolithic sample is reported in Table 10. In particular, the table shows the results obtained before and after treatment with LA.

The value of the ED is the mean value over all the measurements for which the sensitivity correction has been successful.

The correction for sensitivity changes was made by monitoring the luminescence response of the sample to a subsequent test dose of 1 Gy, given to the sample after measuring the natural dose and after each regeneration step, as resumed in Table 10. The correction procedure consists in normalizing each measurement to the intensity of the relative test dose. Because the first regeneration dose equals to the last regeneration, the TL normalized intensities for these two regeneration doses should be identical if the correction is successful [48].

Figure 59 and Figure 60 show examples of the sensitivity-corrected TL signal versus radiation dose. The data of the growth curve, corrected for sensitivity, were fitted by a linear function. The ED was calculated from the growth curve extracting its value at the corrected NTL.

The AD has been determined by measuring the natural radiation coming from the ceramic itself due to their content in radioactive elements (U, Th, K-40), adding then gamma and cosmic radiation from the surrounding [48]. The data on radioactive content of K, Th and U are obtained by Laser Ablation-Inductively Coupled Plasma-Mass Spectrometry (LA-ICP-MS) and converted to infinite matrix dose using the conversion factors by Adamiec and Aitken [48]. Contributions from cosmic rays were included using the equations given by Prescott and Hutton. The contribute of cosmic rays is in agreement with that obtained by Bianca et al. for the same geographical area. The AD has been corrected using, for the moisture rate (W), the water content attenuation factor given by Zimmerman and the size attenuation factors of Mejdahl (i.e. 1.25 for beta and 1.14 for gamma contributions) [48]. The results of the dating obtained show the compatibility of the results both before and after treatment with LA.

The temperature of the sample rises (as visible in Figure 61) during the first minutes of ablation reaches a value of saturation that remains unchanged during the entire process of ablation. The temperature achieves a saturation value of about 100˚C, value very far from what necessary to empty metastable traps, which are above 270˚C.

"TOR" sample	N°	ED (gy)	AD (mGy/a)	Age (a)	TL Dating	Site historical dating
BEFORE LA	3	12.2	2.3±0.1	5300±400	3300±400 BC	"Stentinello" Culture-IV millennium B.C.
AFTER LA	3	11.8	2.3±0.1	5100±800	3100±800 BC	"Stentinello" Culture-IV millennium B.C.

Table 10: Equivalent Dose (ED) and TL dating of the samples as obtained using TL data based on the S.A.R. protocol. The label "N°" indicates the number of measurements for which the sensitivity correction has been successful. The table shows the results obtained before and after treatment with Laser Ablation.

Table 11: Sequence illustrating an example of the procedure for S.A.R. measurements adopted in this study.

Step	Sequence		Label
1	NTL 450°C, 5°C/s		NTL
2	Irrβ 1Gy + TL	Test dose	Test NTL
3	Irrβ 2Gy + TL	First Regenerative dose	First TL 2Gy
4	Irrβ 1Gy + TL	Test dose	Test TL 2Gy
-	-	-	-
x	Irrβ x Gy + TL	"x" Regenerative dose	TL "x" Gy
-	Irrβ 1Gy + TL	Test dose	Test TL "x" Gy
-	-	-	-
-	Irrβ 2Gy + TL	Last Regenerative dose	Last TL 2Gy
-	Irrβ 1Gy + TL	Test dose	Test TL 2Gy

Figure 59: Determination of the Equivalent Dose, ED, of Neolithic sample, before Laser Ablation, based on the Single Aliquot Regenerative-dose (SAR) protocol. The experimental points are fitted by a linear function.
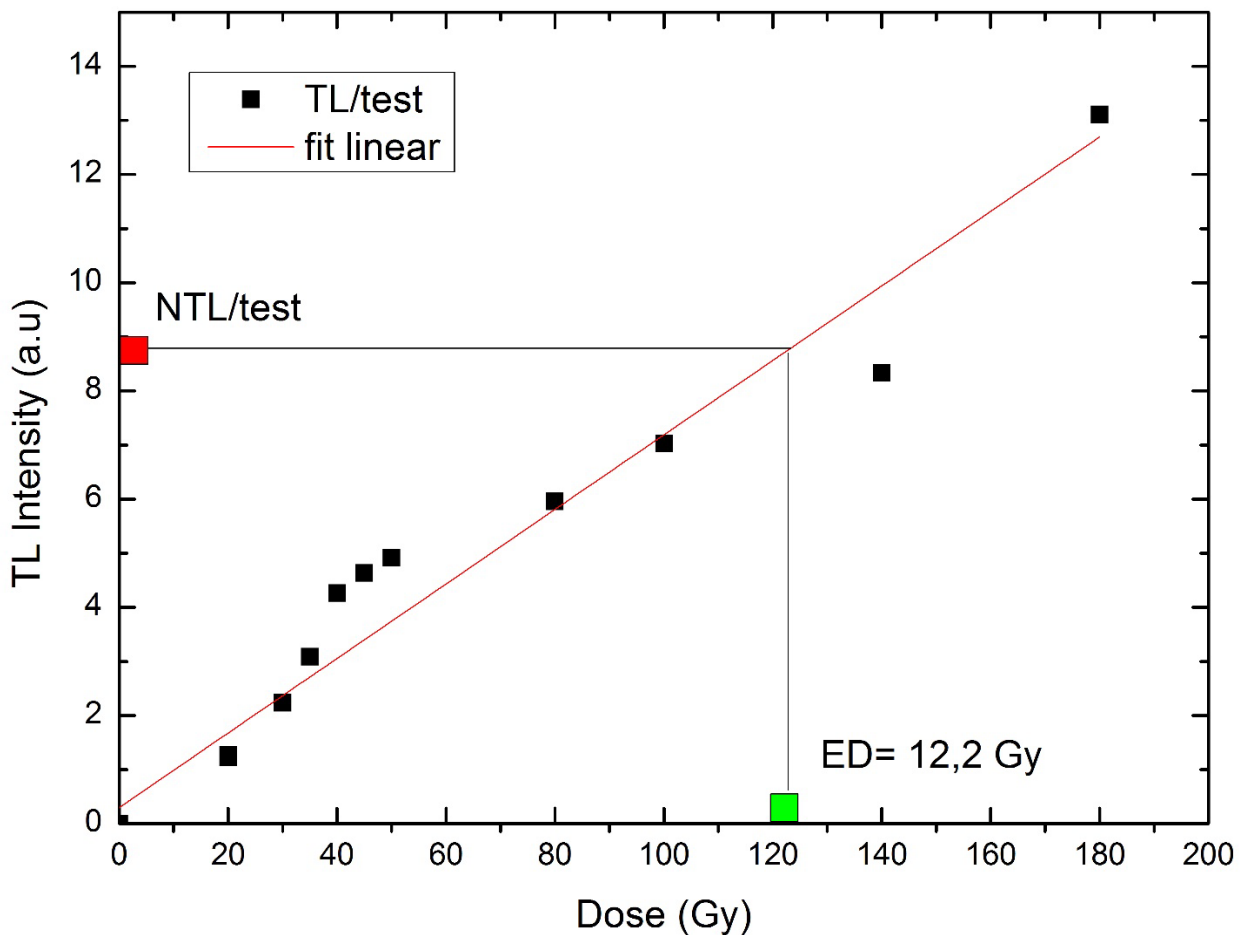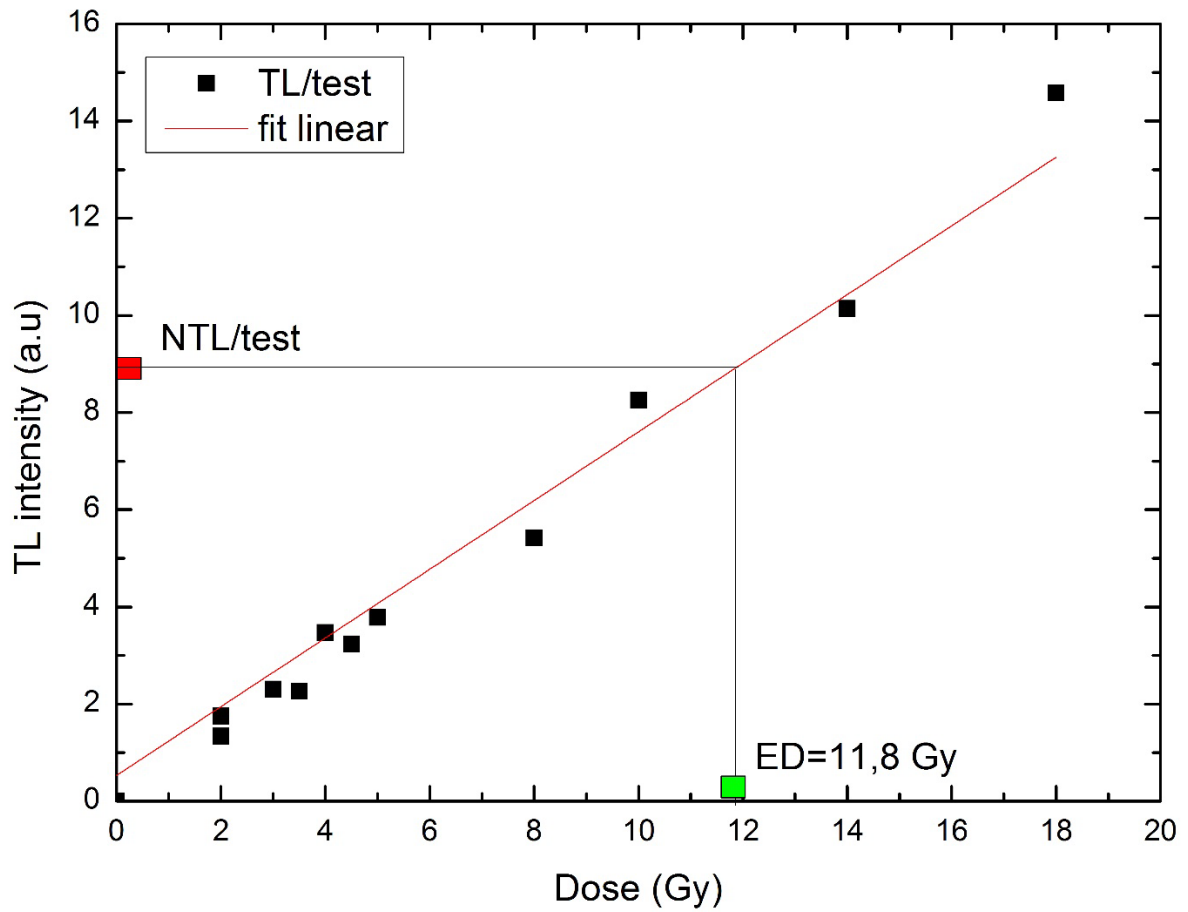
Figure 60: Determination of the Equivalent Dose, ED, of Neolithic sample, after Laser Ablation, based on the Single Aliquot Regenerative-dose (SAR) protocol. The experimental points are fitted by a linear function.
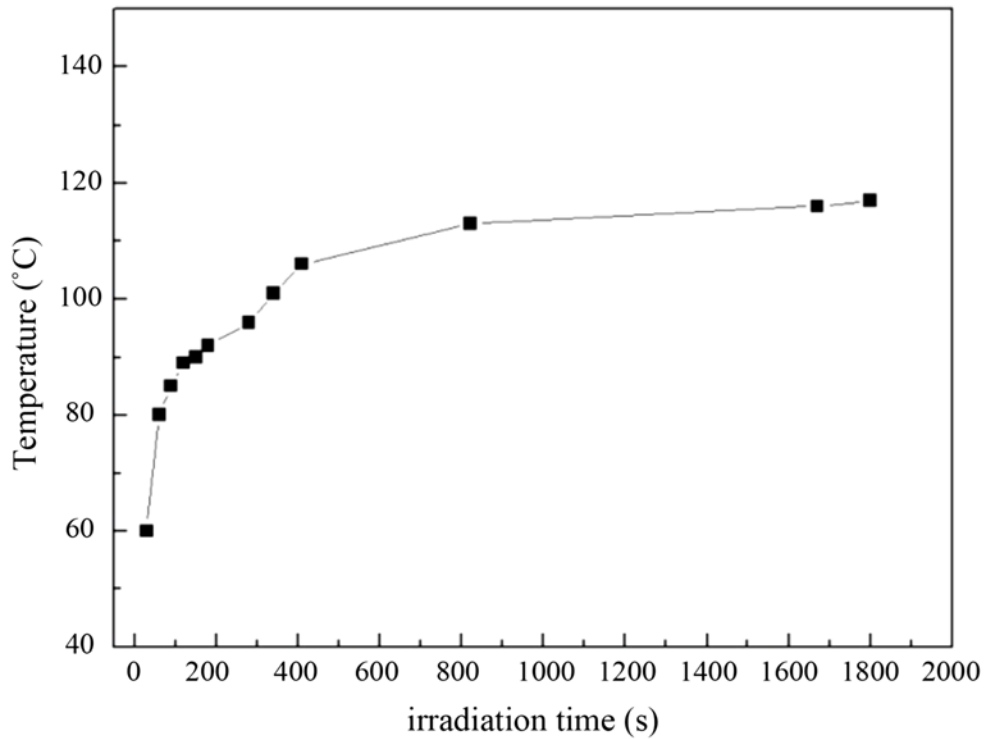

Figure 61: Monitoring of the temperature during the ablation process.

4. Recovery of by-products generated from LA

Conservation science is a multifaceted discipline that deals with the restoration and preservation of a large variety of materials constituting our cultural heritage. Science, art, and humanities seem disconnected disciplines. However, our way of thinking and behaving depends strongly on the legacy of physical artifacts and intangible attributes of a society, inherited from past generations, maintained in the present, and possibly bestowed for the benefit of future generations [49].

Since of the complexity of artistic and historical substrates, conservation science has explored different routes, developing several approaches for solving conservation issues. For instance, new resins that are more stable than natural ones, while exhibiting similar optical properties have been developed and applied as varnishes for retouching paintings [49].

Furthermore, the analysis of materials is often considered a preliminary step for suggesting treatments for works of art: in the conservation of matte paintings, as example, the analysis of the physical and optical properties of the painted layers is the key to choosing the best materials for their consolidation.

Colloid science has been providing an increasingly important contribution to the development of restoration tools. Among the systems specifically tailored for conservation issues, nanoparticulate inorganic sols (nanosols) and colloidal silica play an important role in stone and wood conservation. In particular, because of their high surface-to-volume ratio, nanosols are metastable and usually hydrolysing to form a network that improve the mechanical properties and resistance to water, fire, and microbial attack of artifacts [49].

A very simple way to generate this type of colloid is the recovery of the material generated from LA cleaning to create a protective thin layer or film on surface.

In addition to studying the effect of cleaning for LA, we have performed a study on the using of nanoparticles produced by LA for growing thin films for consolidation and restoration of artifacts and for defining new high-tech devices for many technological applications (as photovoltaic and opto-electronics

4.1. LA for conservation and consolidation of Cultural Heritage assets

As often happens, artifacts are exposed to humidity and to harsh environmental chemical and biological conditions. This results in the formation of a corrosive patina on surfaces which irremediable damages to the artifacts (as in the case of the bronze, where the formation of a bronze disease can damage the artifacts until its complete destruction).

Usually the restoration and conservation process consists in the removal of the corrosive patina, the consolidation with mortar (for artificial stone materials) and resins (for stone and metals) in the coating with a hydrophobic and bactericidal film [50].

Therefore, the materials used for this purpose strongly modify the artifacts surfaces, covering decoration and pigments, and the process is often irreversible.

In recent years, the use of nanotechnology in restoration and consolidation of cultural artifacts has become more popular because these methods can ensure versatility, green chemistry and low impact on chemical compositions of materials. Great interest has been devoted to consolidation of artifacts with thin films and nanoparticles to consolidate and to realize transparent hydrophobic and bactericidal protective layer on surfaces [50]. In this context, TiO_2 is as one of the most fascinating materials characterized by chemical stability, non-toxicity, high photo-reactivity, broad-spectrum antibiosis and cheapness, and it has been used extensively as biocide against various microorganisms: bacteria, fungi and viruses [50]. Moreover, TiO_2 has very different behavior when exposed to electromagnetic irradiation. Under ultraviolet irradiation, titanium dioxide develops super-hydrophilic features. This propriety allows to increase water contact angle and to form a uniform protective water film on surfaces treated with TIO_2. While under visible irradiation, titanium dioxide became hydrophobic with a contact angle of about 60-70 degree [51].

In the other hands, since hierarchical roughness of a surface greatly increases its hydrophobicity [50], the research will also aim to grow, on the surface to be protected, a hierarchically-structured transparent film NPs stabilized by an elastomeric matrix based on hydrophobic components such as, for example, poly (dimethylsiloxane) [50].

4.1.1. TiO_2 and SiO_2 nanoparticles films as protective layers for cultural heritage

The main idea of this work is to realize highly roughness film on artifact surface using TiO_2 and SiO_2 NPs without causing chemical, morphological or aesthetical changes on artifacts. The NPs were prepared as colloidal solution and then deposed on ceramic artifact. We study the influence of nanoparticle deposition on artifacts evaluating the penetration depth of particles into porous materials with EDX and XPS spectroscopies, the hydrophobicity of deposited film with contact angle measurements, and the influence on natural luminescence emission in order to evaluate the influence of restoration on dating and diagnostic processes.

TiO_2 and SiO_2 nanoparticles were produced by a laser ablation in solution (LASiS) method.

4.1.1.1. Growth of TiO_2 and SiO_2 NPs by LASiS

250 mg of TiO_2 grains, or a wafer of SiO_2 (both purchased from Goodfellow with a purity greater than 90%), were deposed on the bottom of a cuvette, filled with 10 ml of acetone, and then irradiated with the first harmonic (1064 nm) of a Laser Nd:YAG (fluence of 500 mJ/cm2, pulse of 7 ns and a frequency of 20 Hz). Shape and dimensions of produced nanoparticles were controlled measuring the optical absorption of solution during irradiation and comparing the measured extinction cross section with that expected from electrodynamics theory [13] (a sketch of experimental setup is showed in fig. 1). Theoretical data for TiO_2 and SiO_2 NP were evaluated implementing the exact algorithm of Mie-Gans theory and using as chemical parameter for both materials the data in Palik Handbook [52]. Two different amounts of colloidal solutions (5 ml and 50 ml), were collected in the first 30 s of laser irradiation and spry-dried on several fragments of ceramic artifact (extracted from the altar of the "Sotterra" church, south of Italy, fig. 1B), while a droplet of 50 μl of colloidal solution was deposed on a silicon wafer for morphological and chemical analysis.

4.1.1.2.   Analysis of NP optical properties

Measurements of optical absorption during laser irradiation were obtained irradiating the solution by a white lamp (Energetiq LDLS, Laser Driven Light Source), and taken the transmitted spectra by a Triax 320 (Horiba-Jobyn–Yvon) spectrometer working in the 300-800 nm range. The extinction cross-section and optical absorption was then evaluated using the standard equations:

$$\in (\lambda) = -Log\ \frac{I_t(\lambda)}{I_0(\lambda)}$$

$$a\ (\lambda) = 1 - \frac{I_t(\lambda)}{I_0(\lambda)}$$

Where I_t, I_0, a, and $\in$ are, respectively, the transmitted and source intensity, the absorption coefficient and the extinction cross-section at each wavelength.

Particle concentration in solution was evaluated from optical absorption of colloidal solution using the Lambert and Beer law:

$$a = c * \sigma * l$$

Where c is the particle concentration, σ the molar extinction cross section (obtained from chemistry handbook [53]) and l the optical path length in our experimental setup (1 cm).

Analysis of extinction cross-section during irradiation (fig.s 62A and 62B) and of temporal evolution of particle concentration (fig.s 62C and 62D) indicate the formation of particle with radius of 10 nm for SiO_2 and 15 nm for TiO_2 NP in the first 25 s of irradiation. After that time, an aggregation between NP starts and particles with greater dimensions nucleate in solution. In the first 25 s the extinction cross-section increases in intensity while the plasmonic peak is fixed at position 397 nm for SiO_2 and 410 nm for TiO_2, indicating that particles with well-defined dimensions are present in solution and their concentration increases linearly (as visible in concentration evolution in fig. 62C and 62 D). We can conclude that in this time only the primary particles produced by laser irradiation are present in solution. For irradiation time greater than 25 s, the solution became dark, the plasmonic peak red-shift, and the concentration of primary particles reach a saturation level, we can, then, conclude that at 25-30 s a process of particle aggregation starts in solution. Only the particles produced in the first 25 s were deposed on artifact surface and characterized by AFM and SEM microscopies.
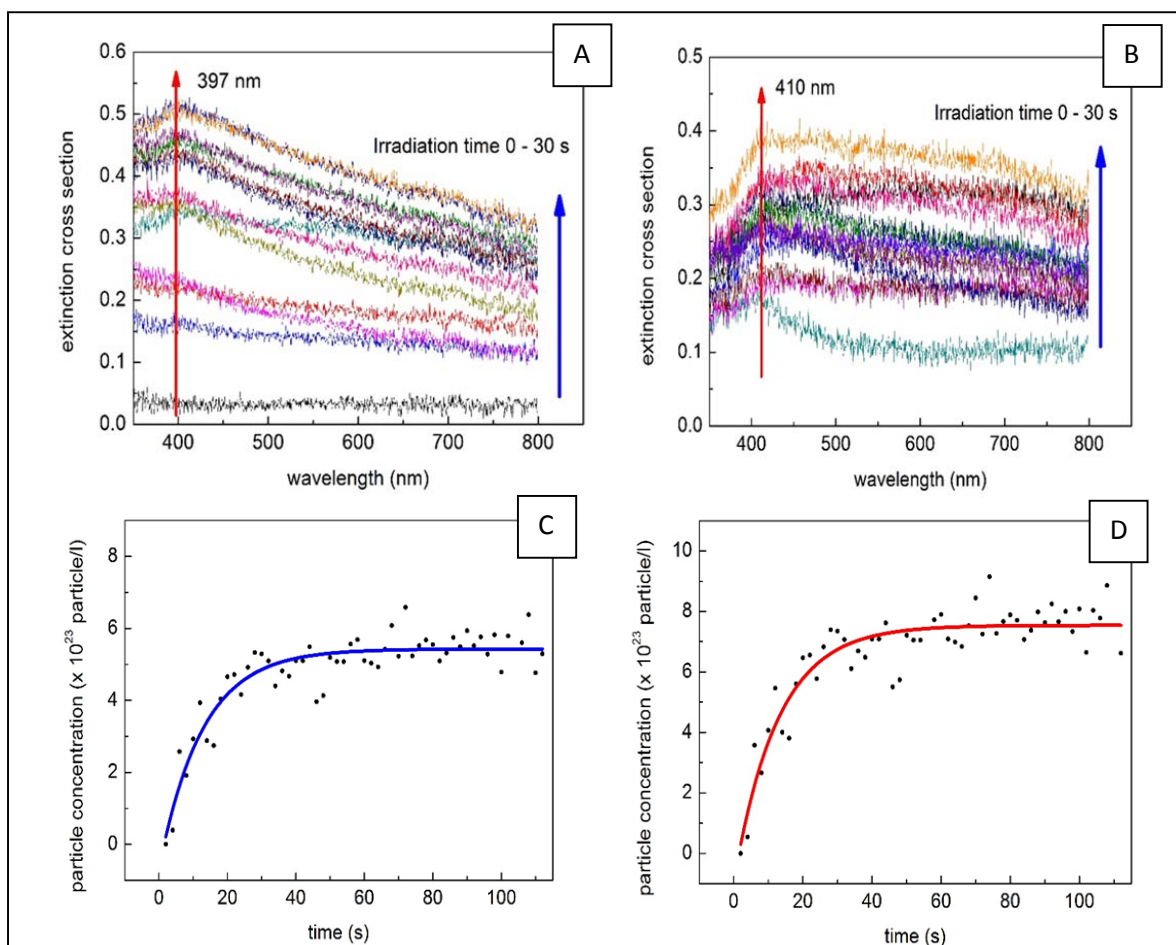
Figure 62: Extinction cross section in the first 30 s of irradiation for SiO$_2$ (A) and TiO$_2$ (B) NP. Particle concentration evolution during LASiS for SiO$_2$ (C) and TiO$_2$ (D).

4.1.1.3. Morphological analysis: AFM and SEM analysis on NPs

Morphological analysis of both NPs were conducted by AFM microscopies, while SEM microscopy was used to study the morphology of particle layer deposed on ceramic artifact.

AFM images were obtained by the ICON AFM microscope from Bruker working in contact mode. Each image was taken with a resolution of 512 x 512 pixels and a frequency of about 1 Hz. Shape and dimensions of NPs were analyzed conducting a statistical analysis on many nanoparticles collected in several AFM images. For each sample, we scanned several areas in window of 500 nm x 500 nm, 1 μm x 1 μm and 5 μm x 5 μm. The images were, then, elaborated by the Nanoscope software (1.40 version from Bruker) to obtain 3D structure and to measure dimensions.

The radius of each nanoparticles was evaluated assuming that a spherical NPs rests on Si surface forming a spherical cap-like structure, the radius r_i of each NP can, then, calculate assuming that the volume of spherical particle is conserved on the deposition process. SEM images were taken under a STEREOSCAN SEM microscope working with energy of 20 keV. AFM and SEM images (fig.s from 63 A, B, D, E, G, I) confirm the previsions of extinction cross section analysis showing the presence of

particles with dimension distributed as a LogNorm distribution [13] (see Histograms in fig.s 63 C and F), whit averages at 9.82 nm and 14.83 nm for SiO$_2$ and TiO$_2$ NPs respectively and very low standard deviations (in the range of 0.02 nm for both particles species). EDX measurements (fig. 63 H and L) conducted on a series of NPs indicated the only presence on particle of titanium, oxygen, and silicon, without presence of external impurities introduced during the growth process.
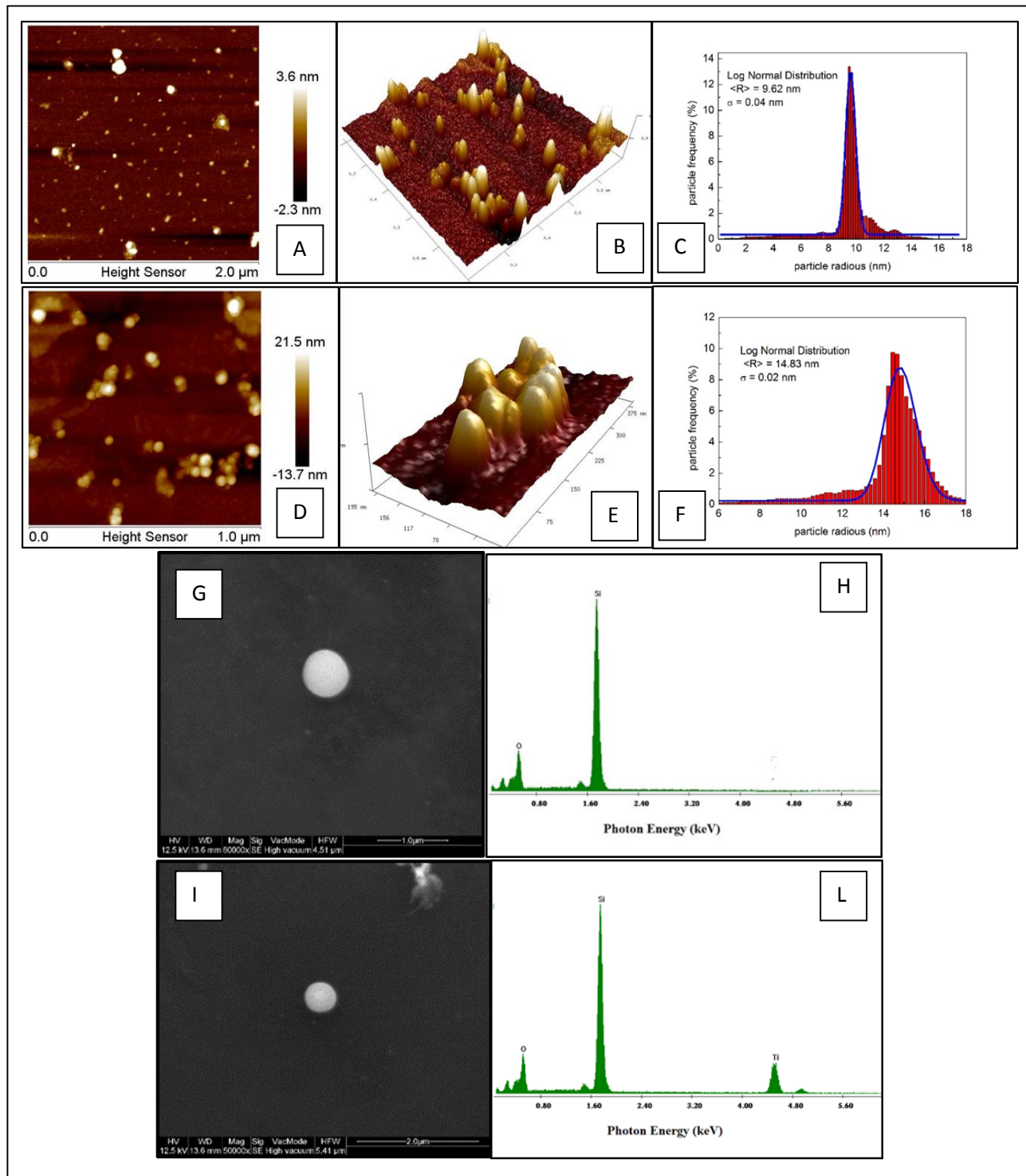

Figure 63: AFM and SEM images for SiO$_2$ (A B G) and TiO$_2$ (D E I). Distribution of particle radius for SiO$_2$ (C) and TiO$_2$ (F). EDX measurements taken on a single NP for SiO$_2$ (H) and TiO$_2$ (L)

SEM and EDX analysis conducted on ceramic artifacts with deposed NP layer (50 ml of colloidal solution, fig.s 64A and 64B for the deposition of TiO$_2$ NPs as example for both species of NPs), indicate the formation on sample surface of a uniform layer of NPs, without introduction of external impurities or damage on surface, moreover the layer is perfectly transparent. The results of depth profile analysis, taken on a fragment with a deposition of 5 ml of solution, are summarized on fig. 65 and table 12. The XPS spectra, as EDX, shows the only presence on surface of constituting elements of ceramic and of NPs, confirming the absence of external impurities. Ti 2p and Si 2p lines are centered at positions typical of corresponding dioxide [36], indicating the absence of chemical bonds between NPs and chemical elements in artifacts and the physisorption nature of NPs adsorption. The depth profile, taken for Ti 2p photoelectron, indicating that, after a deposition of a small amount of colloidal solution (5 ml), the NP are prevalently concentrated in the less layer of surface. This suggest that NP penetrate the pore of ceramic consolidating the material's surface.
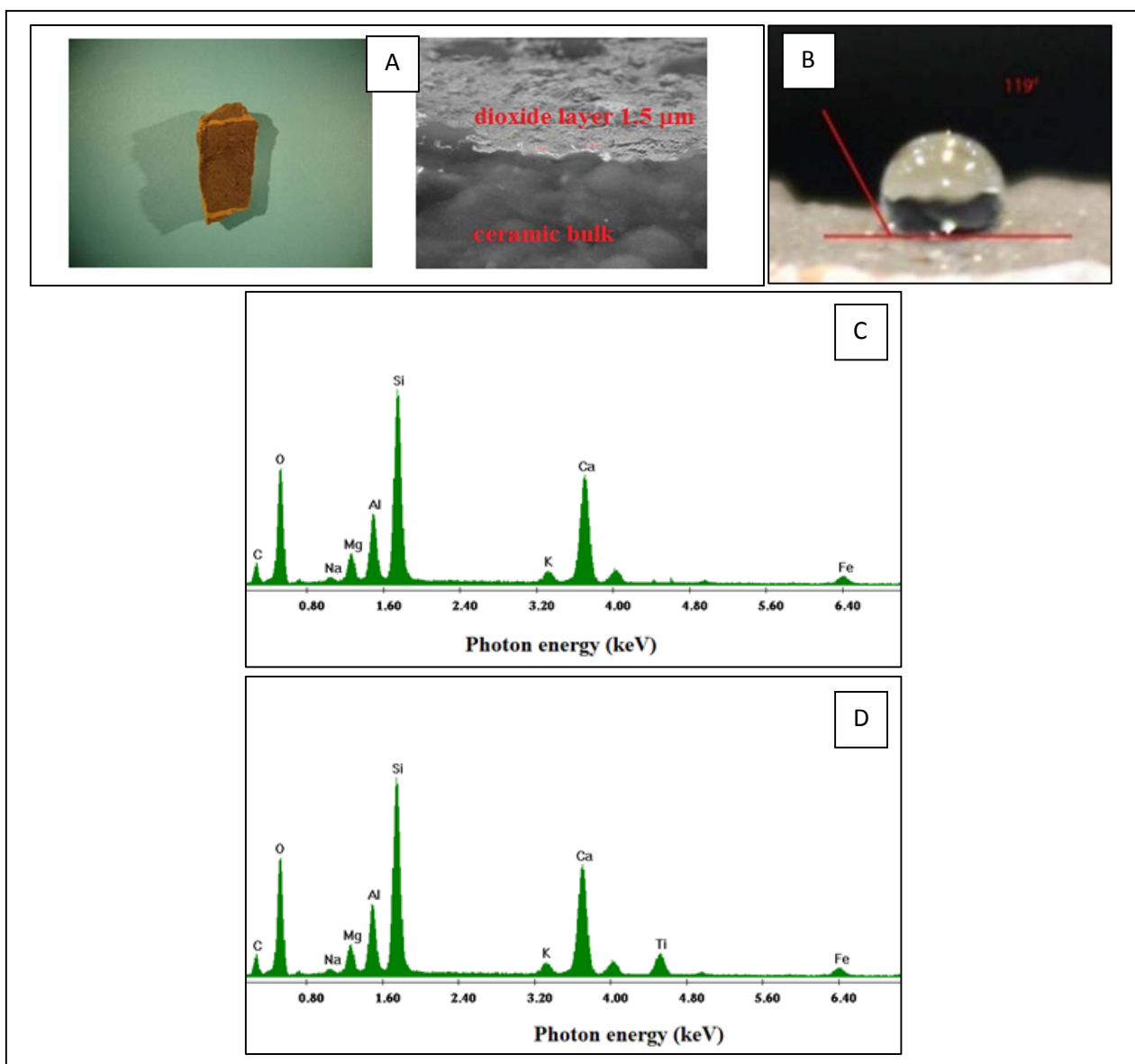
Figure 64: SEM and optical images (A) of TiO$_2$ layer on ceramic surface, contact angle on layer (B) and EDX measurements before (C) and after (D) NP deposition
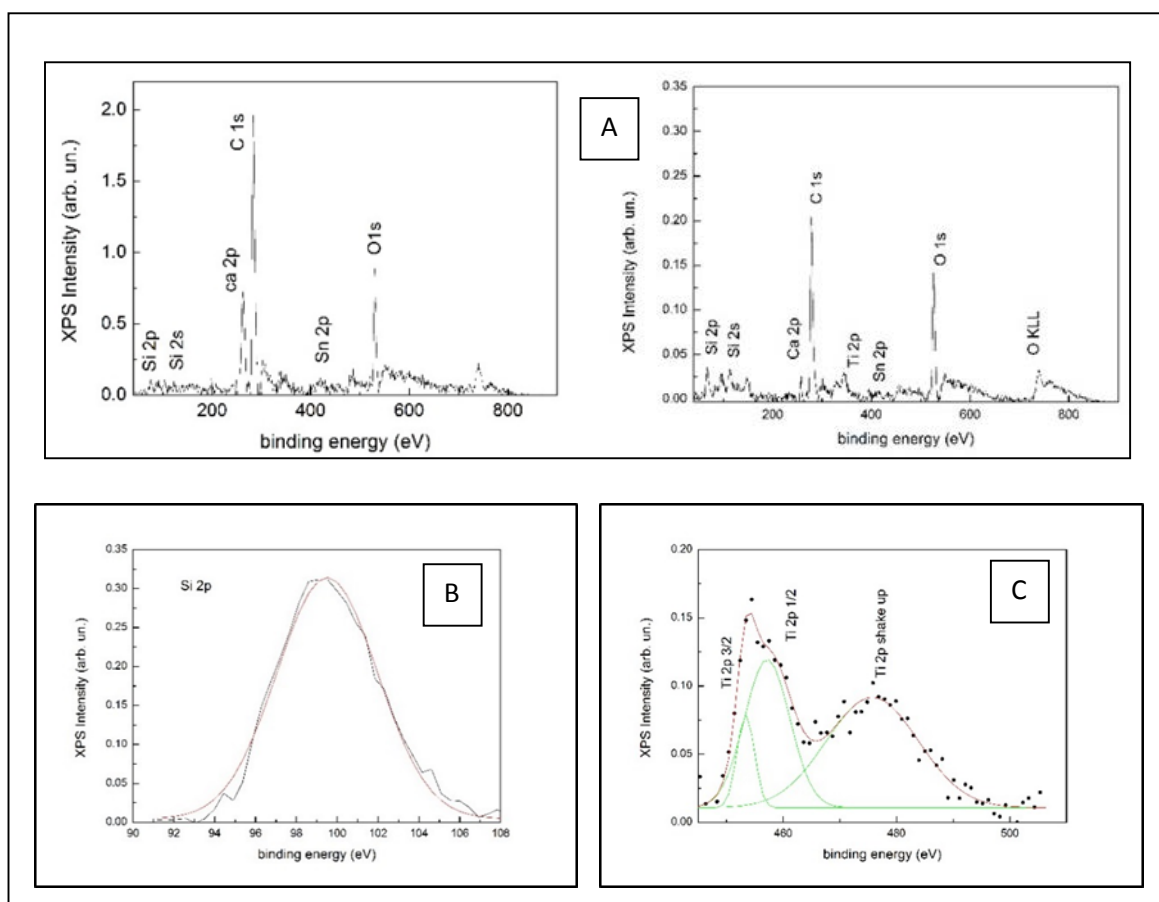
Figure 65: XPS survey spectrum (A), Si 2p (B) and TiO₂ (C) details

	1.4 nm	1 nm	0.17 nm
Si	9.69	9.82	4.6
C	64.6	66.4	8.02
Ca	8.12	4.1	2.8
O	15.4	17.9	11.9
Ti	1.67	0.88	0.36
Sn	0.44	0.84	-

Table 12: Element's percentage as function of depth

111

4.1.1.4. Chemical analysis: EDX and XPS analysis on NPs

Chemical information on all samples were obtained from Electron Dispersion X-ray (EDX) spectroscopy, under SEM conditions (realized simultaneously to images acquisition), and X-ray photoelectron spectroscopy (XPS).

XPS experiments were conducted in a UHV chamber equipped for standard surface analysis with a pressure in the range of 10^{-9} torr. Non-monochromatic Mg-Kα X-ray (hv=1253.64 eV) was used as excitation source while XPS spectra were calibrated with the C1s peak of a pure carbon sample (energy position 284.6 eV). All XPS spectra have been corrected for analyzer transmission and the background has been subtracted using the straight-line subtraction mode. In order to evaluate the penetration depth of NP on surface we evaluate the depth profile of TiO_2. The measurements were taken using data acquired in an angular dependent XPS experiment [32], we measure photoemission at three different photoemission angles (45°, 60° and 80°) evaluating the penetration length with the Hill method [54]:

$$t = -\lambda \, \cos\theta \, \ln\left(1 + \frac{I_0/s_0}{I_s/s_s}\right)$$

Where t is the penetration length and λ the mean free path of photoelectron. We assume that the ceramic matrix is mainly constituted by amorphous Silicon Dioxide and assume that the mean free path of Ti 2p photoelectron in this network is 2.04 nm [55].

4.1.1.5. PL measurements

In order to verify the influence of NP introduction on natural luminescence emission and, then, on thermoluminescence dating process, Photoluminescence (PL) measurements were taken. PL spectroscopy was performed by an Olympus microscope (Horiba-Jobyn Yvon) mounting objectives of 10X, 50X and 100X magnifications. The microscope is equipped by a 375 nm-laser source with a power of 15 mW, for PL, and by a Triax 320 (Horiba-Jobyn–Yvon) spectrometer working in the 200-1500 nm range.

PL measurements (fig. 66) indicate a decrease in natural luminescence emission of about 27% after deposition of both NPs without shift in band position which keep these typical of ceramic artifacts and ascribed amorphous silicon dioxide [47] [56]. The shift absence in PL bands confirm the absence

of chemical bonds obtained by XPS measurements while the decreases of PL intensity is caused by the reconstruction of ceramic pores which can change the network structure (PL intensity is strongly related to the network configuration of a material). These results suggest a strong influence of insertion of NP on the possibility of dating by thermoluminescence measurements.
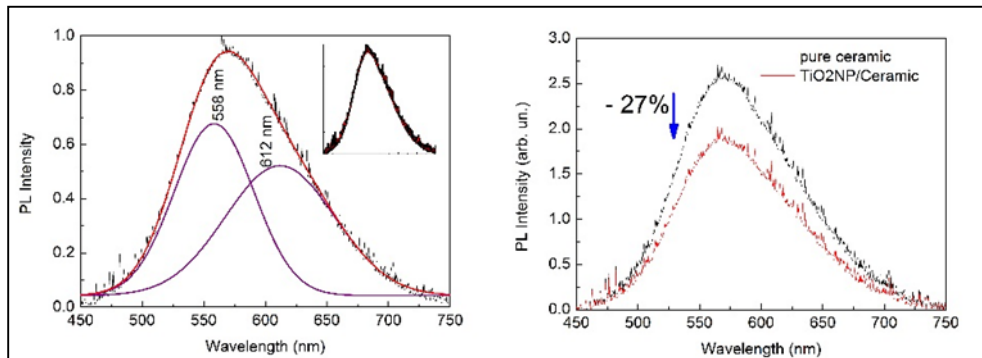
Figure 66: Photoluminescence spectra

4.1.1.6.   Contact angle measurements on protective layer

Finally, the hydrophobic properties of artifact was measured by contact angle measurements obtained deposing a droplet of 2 µl on artifact surface.

Contact angle measurements (fig. 64B) indicate that only the formation of NP layer on surface can ensure the hydrophobicity; in fact, only the fragments with a deposition of 50 ml and a formation of NP layer show a great contact angle.

4.2. LA for realization of nanocomposites for photovoltaic applications

We have previously described as the NPs generated by LA cleaning, can be retrieved to generate hydrophobic layer on the surface of the product, and to consolidate the artifact itself. These NPs can be used not only in the cultural heritage field, but can be used for the production of nanocomposites. Nowadays, NPs, but more often nanocomposites, are very often used in photovoltaic applications. A composite is a multiphase solid material. Two or more individual materials incorporate it through physical or chemical methods. The performance of different materials to complement each other will produce synergistic effects. The overall property of composite materials is better than that of each original material to meet different requirements [57].

A nanocomposite also includes the material where the structures between the different phases that make up the material are in nano-scale. In the broadest sense, nanocomposites can also include porous media, colloids, gels and polymers, because in these materials the particles or structures are in nano scale. One nanometer is equivalent to the length to tightly line up 10~100 atoms. Nano-materials include nano-powders, nano-fibers, nano-particles and nano thin films. Their structures are between atom (molecular) size and macro size. Materials in

nano-scale have special effects such as quantum size effect, surface effect, small-size effect and macroscopic quantum tunneling effect etc. [57].

Therefore, the strategy to incorporate in a single matrix two different nanostructures with specific properties is a versatile method to transfer and to integrate in a single material the different properties of two materials, enabling to realize multifunctional composites, for using in advanced applications like catalysis, energy storage, nanobiotecnology, optoelectronics, etc. [6].

In our case, we have grown metal NPs to realize two type of nanocomposites. They are compounds by metal NPs / graphite and metal NPs / carbon nanotubes.

4.2.1. <u>Carbon Nanotubes/Metal Nanoparticle Based Nanocomposites</u>

A particular and widely used approach, in growth of nanocomposites, is given by the combination of carbon nanotubes (in both configuration multi walled and single walled) and metals, semiconductors or insulators. In effect, carbon nanotubes (CNT) are one of the most attractive nanomaterials because their unique physicochemical properties and wide potential applications in nanoelectronics, nanolithography and photovoltaic. Two approaches are commonly used to decorate CNT with organic and inorganic compounds: covalent and non-covalent bonds formation. The first, include mainly oxidation and formation of amide bonds, while non-covalent approaches utilize van der Waals interactions between functional compounds and CNT [6].

Recently, non-covalent approach has attracted more attention because permit to obtain nanocomposites with new properties, preserving all the properties of the nanotubes.

The combination between CNT and metal nanoparticles is much interesting because metal exhibits very important optical and electronic properties that can be improved by the mix with CNT. In particular metal, decorated CNT (as example Ag/CNT composites) have gained extensive attention due to their potential applications as catalyst, optical limiters, advanced materials, etc. [6].

The possibility to obtain composites with large visible photoluminescence for optoelectronic devices becomes particularly interesting. The study of optical properties of CNT based heterostructures in this framework assume considerable importance to try improve the luminescence properties of carbon nanotubes in the visible range (pure carbon nanotube not exhibit visible luminescence emission). For this purpose, were made different studies on cathodeluminescence and photoluminescence emission from CNT macroscopic samples [6].

We observed a luminescence signal in the visible region and showed that such emissions are extrinsic to nanotube structures. In fact, it originates from impurities (Ni, Al, Zn, gases) which are residual of materials used in the growing process or subsequently adsorbed in the sample. While for the heterostructures samples growth with carbon nanotubes and insulators or semiconductors component (indicated by X component) shows a strong luminescence signal centered in visible or UV region [6]. Here, we demonstrate the possibility to growth nanocomposites heterostructures based on carbon nanotubes and metal (transition or noble) nanoparticles which exhibits a luminescence emission in all visible region.

4.2.1.1. Growth of metal nanoparticles and realization of metallic NP/carbon nanotube (CNT) nanocomposites

There are several methods of preparing metal/CNT materials including vapor depositions, surface chemical reduction and gamma irradiation. However, all these methods cannot get satisfactory results because, in most cases, the metal nanoparticles can form micro agglomerates that cause problems in samples homogeneity.

For this reason, we used a simple method to produce metal/CNT composites. The method is a sequence of mixing, evaporation and drying processes that lead to the formation of composites where a uniform network of metal nanoparticles is weaved on a CNT matrix. The metal nanoparticles are produced from pure metal by laser ablation. We use both noble (Au and Ag) and transition (Al, Co, Cu, Fe, Ni, Ti) metals to investigate the different interaction between tube and metals and the possible formation of chemical or van deer Waals interaction between tube and nanoparticles. The obtained nanocomposites were characterized by SEM and AFM microscopy, X-ray photoelectron spectroscopy and by measurements of contact angle and surface roughness. Moreover photoluminescence measurements demonstrate the realization of materials with luminescence emission in all visible region the entire journals, and not as an in- dependent document. Please do not revise any of the current designations.

The multi wall carbon nanotubes (MWCNTs) buckypaper sample was purchased from Nanolab Co., with a nominal purity greater than 95%, a diameter of about 30 nm, and a length of 5 - 20 MWCNT is showed in Figure 67(A). The sheet used for nanocomposites growth had a thickness of 0.1 mm and its dimension was 10×10 mm^2.

Metal nanoparticles were produced by laser ablation (LA) of a metal plate in acetone (aqueous solution 99.5%). The metal plate (>99.99%) was vertically placed in a glass vessel filled with a 25 ml of acetone and irradiated for several minutes by the first harmonic (1064 nm) of a Quanta-Giant series 710 Nd:YAG laser operating at 10 Hz. The spot size of the laser beam on the surface of the metal plate is about 7 - 8 mm and the power of laser is fixed at 600 mJ/pulse. During irradiation of the laser beam, the solution, initially transparent, gradually turns colored, indicating the formation of nanoparticles in solution [6].

After LA, the solution is sonicated for 30 minutes to prevent the self-aggregation of the nanoparticles suspended in acetone and the formation of macrocluster. When the solution is sonicated immediately after laser ablation, the dimensions of the deposited particles are identical to those produced in solution during LA (about 40 nm). In fact, the particle dimensions during LA were controlled monitoring the optical absorbance following the Kelly plasmonic theory [58] and subsequently verified by SEM and AFM microscopy (a drop of nanoparticles solution was deposed on a pure copper sheet (pure NP sample) and observed by microscopes.

Figure 67(B) (AFM images) shows, as example, aluminium nanoparticles deposed on copper foil, the particles have dimensions of 40 nm and are perfectly diluted and dispersed on substrate without sign of aggregation.

Metal nanoparticles-carbon nanotubes composites (MNP/MWNT) were obtained positioning the MWCNT sheet in the vessel glass containing the solution after sonication, then the solution was heated up to complete solvent evaporation on a hot plate at 180°C.
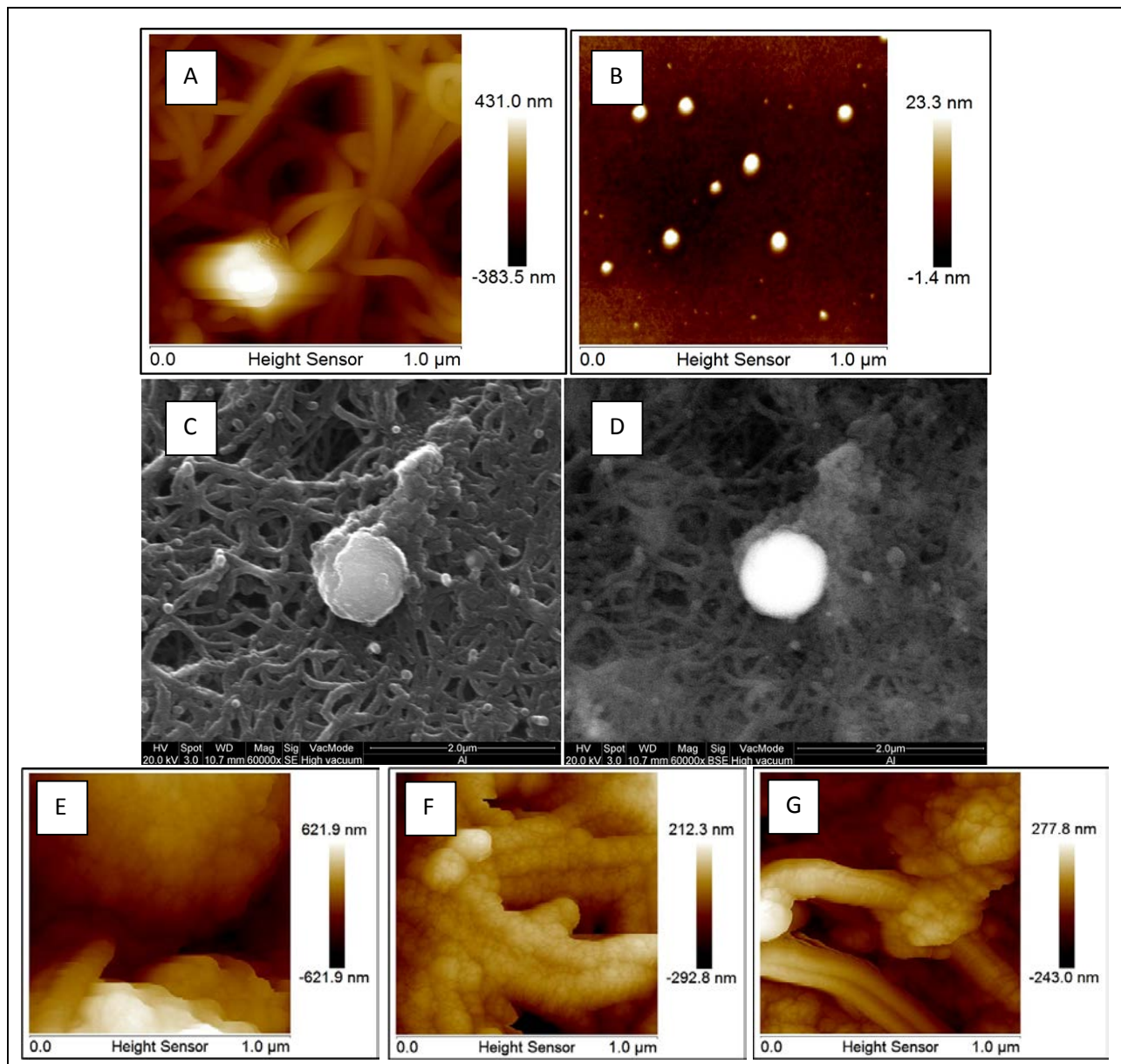

Figure 67: AFM images of (A) pure MWCNT; (B) pure nanoparticle deposed on a pure copper surface. SE-SEM; (C) and BSE-SEM (D) Al/MWNT nanocomposites as example of all transition metals nanocomposites. AFM images of silver/MWNT nanocomposites.

4.2.1.2. Analysis of NP optical properties

The transmitted spectrum, during LA, was obtained by a Horiba VS-140 VIS-NIR spectrometer working in the 350 - 1200 nm range. A white led has been used as light source to enlighten the samples (the vessel glass surface is completely transparent to white light). Transmittance (t (l)) and absorbance (a (l)) as function of wavelength are obtained with the well known relations:

$$t\,(\lambda) = \frac{I_t\,(\lambda)}{I_s(\lambda)}$$

$$a(\lambda) = -\ln t\,(t(\lambda))$$

where I_t is the intensity of light transmitted across the solution and the I_s is the intensity of light source.

The transmitted spectrum was monitored during the whole laser ablation process, taking spectra at regular intervals of 5 seconds. The integrated absorbance $A(t)$ of each spectral transition was obtained by numerical integration, assuming a Gaussian distribution of the spectral bands.

Conventionally, metal nanoparticles are characterized by their extinction spectra (absorption and/or scattering spectra). Peaks observed in absorption or scattering spectra of particles under light excitation reveal resonant wavelengths of plasmon eigenmodes (called dipole plasmon resonance) of the particles as demonstrated in [58]. Secondary oscillations, called quadrupole plasmon resonances, appear at lower energy for larger particles. The plasmon oscillation frequency is determined by four factors: the density of electrons, the effective electron masses and size and shape of charge distribution (i.e. by shape and size of nanoparticles) [58].

We take the absorbance spectrum of acetone-nanoparticles solution during LA at regular time intervals of 5 seconds and observe the changes in its intensity and line shape for 700 seconds.

Figure 68 shows the absorbance spectra acquired after 500 s of irradiation (as an example of typical measured spectra) for all used metals. We observe that all nanoparticles exhibit three bands, with center and Full Width at Half Maximum (FWHM) depending on particles chemical nature and dimensions. The three bands are centered, for all metals, in the region of 300 - 500 nm (P1 bands), 500 - 700 nm (P2 bands) and 930 nm (P3 bands). During the first 100 seconds, the spectra, for all metals, exhibits only the P1 band and P3 with a FWHM of about 30 nm and 60 nm respectively while after the first 100 seconds the P2 band appears. The center and the FWHM of three bands are substantially unchanged during LA, while their intensities increase causing a rapidly increase of total absorption, which, after the first 150 s, is almost linear with LA time (see the Inset in Figure 68).
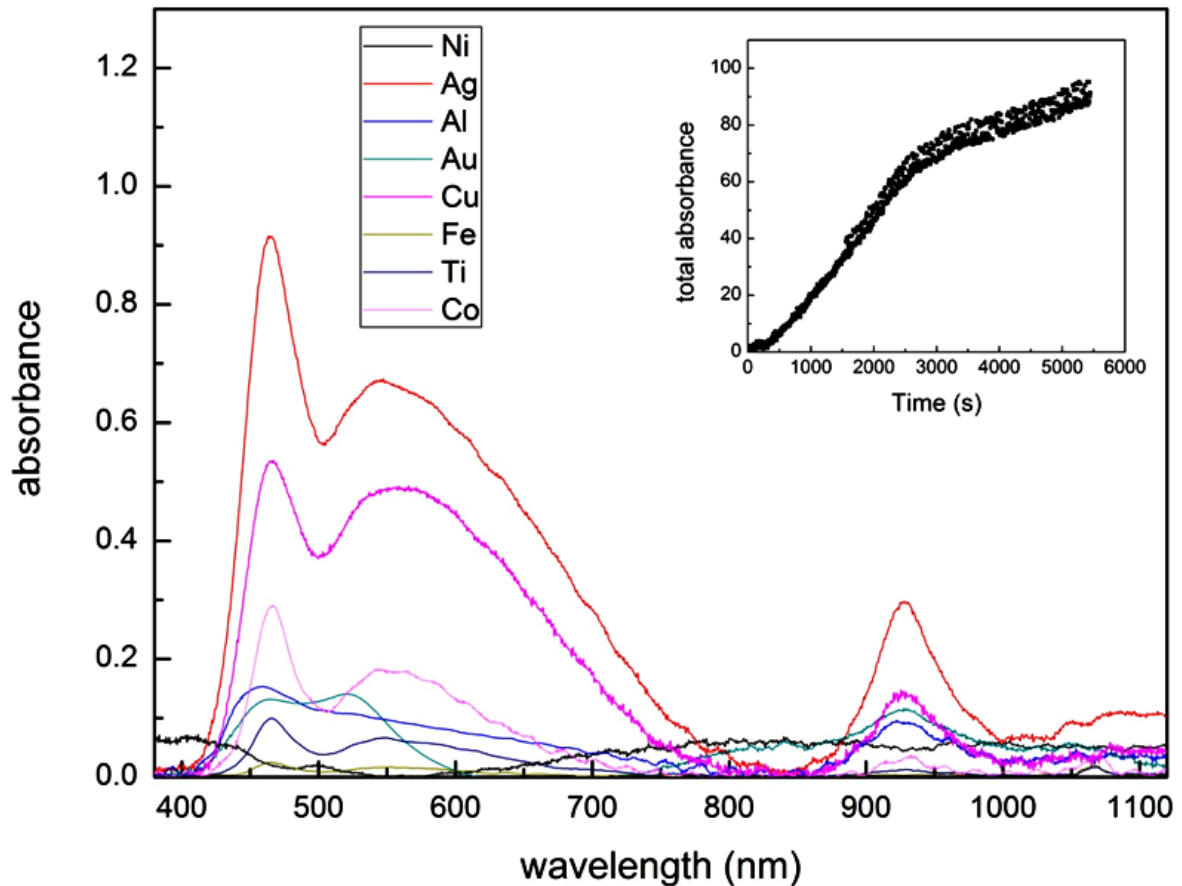
Figure 68: Absorbance spectra of nanoparticles/acetone solutions taken during laser ablation (500 s from LA starting). Inset: total absorbance as function of irradiation time for Al/MWCNT as example for all nanocomposites

All the three bands can be associated to oscillating of surface plasmon in spherical or spheroid nanoparticles. Kelly et al. in their theoretical work [58] calculated, for silver nanoparticles, the plasmon absorption wavelength for both spherical and spheroid nanoparticles as function of particles dimensions. They demonstrated that spherical particles present two absorption bands centered at about 350 nm (dipole resonance) and at 440 - 450 nm (quadrupole resonance) for particles with dimensions of 60 nm. These positions change strongly with particles dimensions and shape. If the sphere diameter increases the bands red-shift and can reach the NIR region if the particles are large spheroids.

Therefore, our absorption spectra (with three resonance bands) can be interpreted as superposition of signals from particles of different sizes in solution. In the first 100 seconds, LA produces spherical particles with low dimensions, which generate the P1 resonance. The dimensions of these particles, from the comparison with numerical data in [58], range between 50 - 70 nm. Moreover, in the first phases, a little amount of spheroid particles are also present (P3 resonance). After the first 100 seconds, the particle concentration in solutions increases and several nanoparticles aggregates to form spherical particles with larger dimensions causing the P2 band appearance. As the LA time increases, several particles aggregate forming larger spheres (shift of both P1 and P2), while spheroid particles increase their concentration without changing size.

119

4.2.1.3. Morphological analysis: AFM and SEM analysis on nanocomposites

SEM and AFM images of nanoparticles (produced in the first 100 s of LA) deposed on a pure copper surface confirm the prevision obtained by Kelly theories [58]. Figure 67(b) shows an AFM images of nanoparticles with dimensions of 50 - 60 nm while SEM images shows also the presence of bigger particles (100 nm in diameter) also visible in SEM images of composites in Figure 67.

All MNP/MWNT composites at SEM images, at zoom level of then of microns, appears as a bulk of carbon nanotubes with random insertions of metal nanoparticles of dimensions of about 100 - 150 nm, as visible in SE-SEM and BSE-SEM of Figure 67(c) and (d) (the figure shows the images for Al/MWCNT as example for all composites). While details, taken by AFM (at zoom level of 500 nm), show a very different situation for noble and transitions metals. Transitions metal nanoparticle, as visible in fig. 67(e) and (f) (for Co as example for all transition metals), are arranged either to form bigger particles (as visible in SEM images) or to cover the single tubes with little particles of 40 - 50 nm indicating the formation of a strictly bond between tubes and particles which don't correspond to a simple MWCNT doping but at a growth of new materials. Noble metal particles, be- sides, show only the formation of bigger particles (Figure 67(g) for silver) randomly distributed on a sheet surface indicating a simple doping mechanism without new materials formation.

Absorbance spectra for these three elements indicate a greater presence of bigger particles (P2 band most intense respect those of other elements) which cannot intercalate in the sheet (covering the tubes in secondary layers) staying on surface.

4.2.1.4. PL measurements

Photoluminescence measurements indicate a strong visible luminescence for all composites with a great effectiveness for samples obtained with copper; gold and titanium (see Figure 69). All the PL spectra (except Ag and Al whose intensity is too low to allow analysis Gaussian) present two main bands centered at about 2.2 eV and 2 eV (see Table 13 and inset in Figure 69 for Gaussian analysis) indicated that the interaction between tubes and metal nanoparticles causes changes in CNT electronics bands reducing the optical bands and favoring the visible transitions absent in pure CNT. We have demonstrated the effectiveness in optical changes for metal doping of CNT, now we can confirm that and extend the results to transitions metals indicating, moreover, the formation of

composites with hydrophobic properties and roughness reduced compared to pure carbon nanotubes.
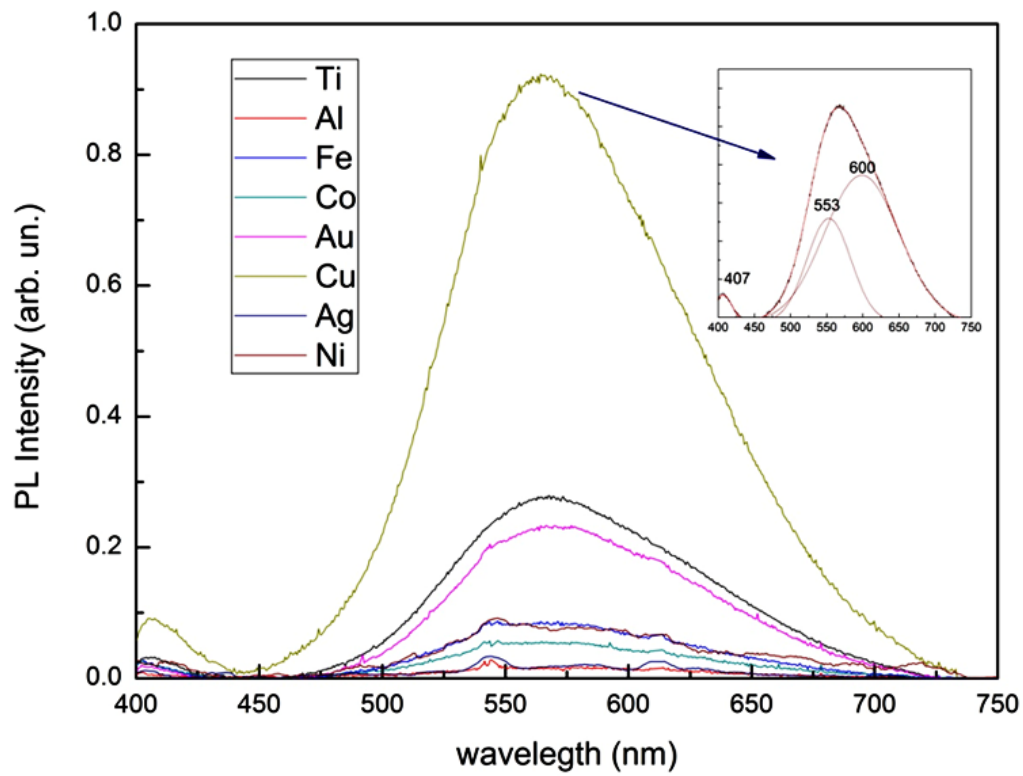

Figure 69: Photoluminescence spectra for all nanocomposites. Inset: example of Gaussian analysis.

Table 13: PL peach position for each nanocomposites (each nanocomposite is identified by its metal nanoparticle for Ag and Au the signal is too less for Gaussian analysis).

	P1 position (eV)	P2 position (eV)
Ag		
Al		
Au	2.24	2.04
Co	2.25	2.05
Cu	2.25	2.09
Fe	2.25	2.05
Ni	2.23	2.02
Ti	2.24	2.06

4.2.1.5. Chemical analysis: XPS analysis on nanocomposites

XPS measurements, taken on the pure NP sample (drop deposed on Cu), were conducted in a UHV chamber equipped for standard surface analysis with a pressure in the range of 10^{-9} torr. Non monochromatic Mg-Kα X-ray (hv = 1253.64 eV) was used as excitation source. The XPS spectra were calibrated with the C1s peak of a pure carbon sample (energy position 284.6 eV). All XPS spectra have been corrected for analyzer transmission and the background has been subtracted using the straight line subtraction mode. Moreover, the XPS data were fitted assuming a Gaussian distribution.

For all samples, XPS data indicate the absence of chemical bonds between carbon nanotubes and metals specifying the van deer Waals nature of bonding between particle and tubes and the phsysorption character of particle absorption on sheet surface. In fact, the survey spectra indicated in all sample the only presence of Carbon, Oxygen (carbon nanotubes are rich in oxygen which can be eliminate only after heating at very high temperatures) and metal particles without presence of surface impurities. The main XPS lines for all elements, showed in Table 14, are these typical of carbon nanotubes (the C1s line exhibits three line at 284 eV (C main line), 287 eV (C-O bonds) and 303 eV which is due to plasma loss in carbon nanotubes) and of used metals, all the metals exhibits the main atomic lines [36] without chemical shifts related to formation of chemical bonds between metal and C or O (excluding so also the presence of metal oxide formation) [36]. The elements percentage evaluated by XPS data (see Table 14) indicates very different behavior for different metals indicating a great presence on surface only for Al, Cu and Au.

	Main line poistion (eV)	Elements amount on surface (%)
C	284.3 (1s)	
O	531.4 (1s)	
Ag	365.3 (3d 5/2)	1.77
Al	76.3 (2p)	21.81
Au	84.1 (4f)	11.77
Co	781.2 (2p)	2.34
Cu	120.6 (3s)	4.20
Fe	109.6 (2p)	0.06
Ni		0.01
Ti	453.6 (2p 3/2)	1.02

Table 14: XPS main line position for each element in composites (C 1s and O 1s are indicated for pure MWNT) and metal percentage on nanocomposites surface evaluated from XPS data

4.2.1.6.   Contact angle measurements on nanocomposites

The contact angle images was obtained placing a small drop of distilled water (5 ml) on the sample surface and the equilibrium contact angle was determined by drop shape analysis, while sample roughness was measured under AFM conditions.

The substantial changes on sample surfaces, observed in AFM images, are confirmed also by measurements of contact angle (Figure 70) and roughness, both showed in Table 15. These indicate, in all cases, a great improvement respect to pure MWCNT sheet. The composites are, in fact, hydrophobic with contact angle varying from about 40° for Cu to 77° for Ag and Ti, and exhibit a decreases in roughness of about 50%. Only for silver particles the roughness decreases is limited to 30%, confirming the different behavior of these metal observed in sample images.

Table 15: Roughness and contact angle for nanocomposites (each nanocomposite is identified by its metal nanoparticle).

	Roughness (nm)	Roughness variation (%)	Contact angle (°)
Pure CNT	120		
Ag	82	31.67	76.68
Al	65	45.83	64.87
Au	62	48.33	46.72
Co	53	55.83	44.14
Cu	41	65.83	41.14
Fe	66	45.00	39.00
Ni	58	51.67	76.34
Ti	58	51.67	67.83
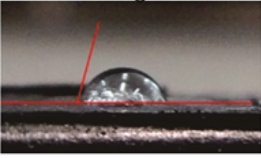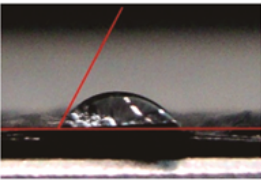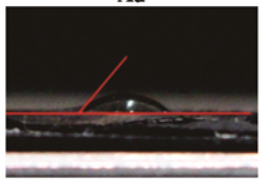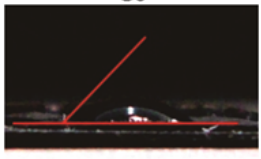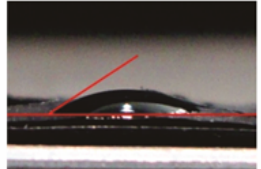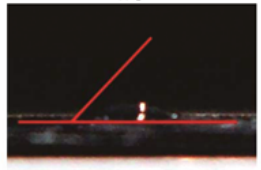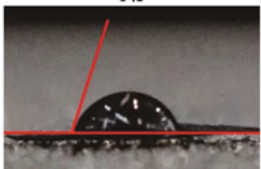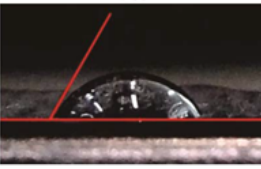
Ag		
		76.68
Al		
		64.87
Au		
		46.72
Co		
		44.14
Cu		
		41.14
Fe		
		39
Ni		
		76.34
Ti		
		67.83

Figure 70: Contact angles for all nanocomposites

4.2.2. <u>Metal Nanoparticles/Graphite nanocomposites</u>

The study of interfacial properties and coatings geometry between different carbon surfaces and metals is so fundamental. Various experiments have been carried out to investigate the contact between different metals and carbon structures [60].

Coating of metals such as Ti, Pd, and Ni lead to the formation of continuous or quasicontinuous layers on the CNT indicating firmadsorption and low contact resistance, while metals such as Fe, Al, and Au lead to the construction of isolated clusters indicating weak interaction and large contact resistance [59]. Studies based on density functional theory attribute the metallic coating properties to the metal-carbon binding energy [59], while study on traditional nucleation and wetting theories indicate in the different metal wetting of carbon surfaces the different coating geometries [60].

Moreover, the combination between a carbon nanostructure and metal nanoparticles is much interesting because metal nanoparticles exhibit very important properties that can be improved by the mix with carbon based nanomaterials [59]. In our previous work [6], we demonstrate that metal nanoparticles (growth by laser ablation techniques and afterwards inserted in carbon nanotubes networks) are distributed on carbon surface to forming coatings geometries that are uniquely related to wetting between carbon and metals. We do not observe formation of chemical bonds between tubes and nanoparticles but the introduction of several local defects on CNT structures, which causes strong changes in morphology, and the appearance of a strong photoluminescence signal in visible region [6].

Here we extend the study of interaction between metal nanoparticles (both noble and transitions metals—Au, Ag, and Co) and carbon surfaces (amorphous graphite and highly oriented pyrolytic graphite (HOPG)). Metal nanoparticles were grown dimensionally controlled and inserted on carbon structures with the same process used for metal/carbon nanotubes nanocomposites in [6]. The obtained samples were characterized morphologically, chemically, and optically using AFM microscopy, X-ray photoelectron spectroscopy, photoluminescence spectroscopy, and optical absorptions measurements in visible regions. The obtained results are identical for both amorphous and oriented graphite (in the following will be showed only the results for HOPG).

Amorphous graphite and high oriented pyrolytic graphite (HOPG) were purchased from Goodfellow and they have a nominal purity greater than 99%. AFM images in Figure 71 for pristine sheets indicate that the samples are smooth and without presence of external impurities. Moreover, the amorphous graphite appears as a random superposition of separate foils while in HOPG carbon foils are uniformly disposed.

4.2.2.1. Growth of metal nanoparticles and realization of metallic NPs/graphite nanocomposites

Metal nanoparticles were produced by laser ablation (LA) used the same parameters for NPs in paragraph 4.2.1.1.

4.2.2.2. Morphological analysis: AFM analysis on nanocomposites

The AFM images of composites in Figure 71 and the particle dimensions histograms in Figure 72 (showed only for HOPG sample) show a very different morphology of nanocomposites obtained by noble or transitions NPs in either amorphous or oriented graphite.

The sample with silver nanoparticles shows the formation of big aggregates randomly distributed on sheet surface and with average dimensions of about 77 nm. Gold nanoparticles, with dimensions of about 25 nm, cover randomly all the sheet surface while cobalt nanoparticles are arranged either to form big aggregates or isolated particle with little particles of about 22 nm. As visible in the left panel of Figure 71, Co nanoparticles with dimensions of about 22 nm are randomly disposed on HOPG surface, while only one isolated aggregate (with dimensions of about 200 nm) is visible. These results are in agreement with those obtained for interaction between metal nanoparticle and carbon nanotubes in our previous work [6] and based on theoretical calculations of He et al. [60], confirming the different behaviour of noble and transitions metals on carbon surfaces. Therefore, we can definitively conclude that the different behaviour of metals is determinate by their different wetting properties on carbon structures, in agreement with the theoretical work in [60]. He et al., in fact, have recently theoretically demonstrated [60] that the metal surface energies (defined as the difference between the total energy of a metal slab and the total number of atoms with energy per atom) and the metal-carbon interfacial energies are of critical importance to determine the nanoparticle arrangement on carbon surfaces. In their work, He et al. calculated the above energies for metals atoms on single wall carbon nanotube surfaces. Therefore, we can extend their theoretical results on interactions between metal's atoms and SWNT also at atom aggregates (nanoparticles) on different carbon surfaces (multiwalled carbon nanotubes [6], amorphous graphite, and HOPG). He et al. suggest that for low cohesion energy, the metal atoms have the tendency to pile up and form isolated clusters. While for low interfacial energy the metal can be adsorbed on the carbon, surface and tend to spread over. The wetting property of metals is so determined by their combination action. Theoretical data in [60] indicated that noble metal (Au and Ag) have the high cohesion energy and low interfacial energy with tube suggesting that these metals rapidly diffuse on surface forming

126

isolated cluster or covering the entire surface. For all transition metals, instead, the interfacial energy is high indicating that the interaction between tube and metal is stronger than metal-metal bulk interaction so the NPs can uniformly disperse on tube surface.
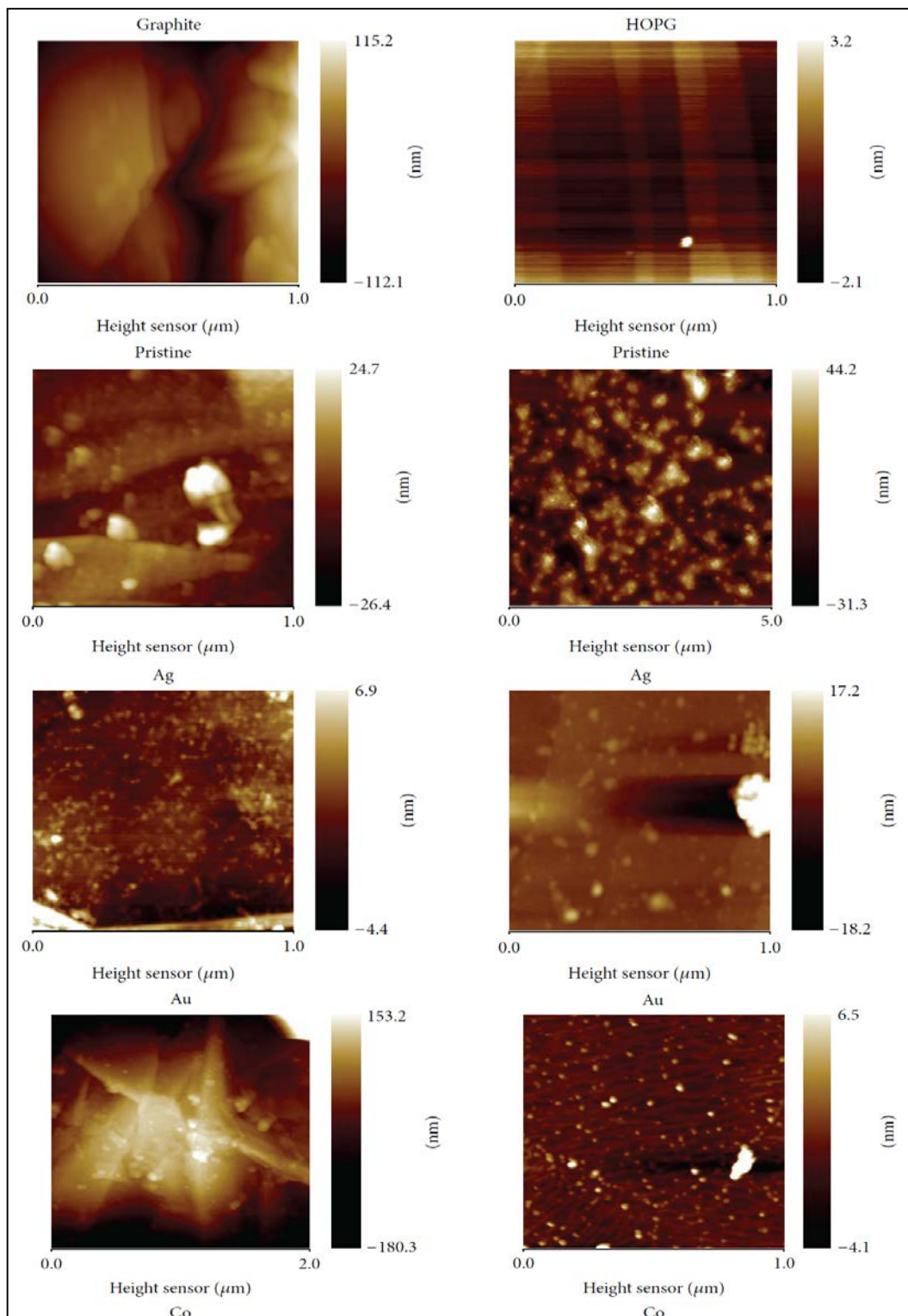

Figure 71: AFM images for pristine amorphous and orientated graphite. The label under each image indicates the metal nanoparticle.
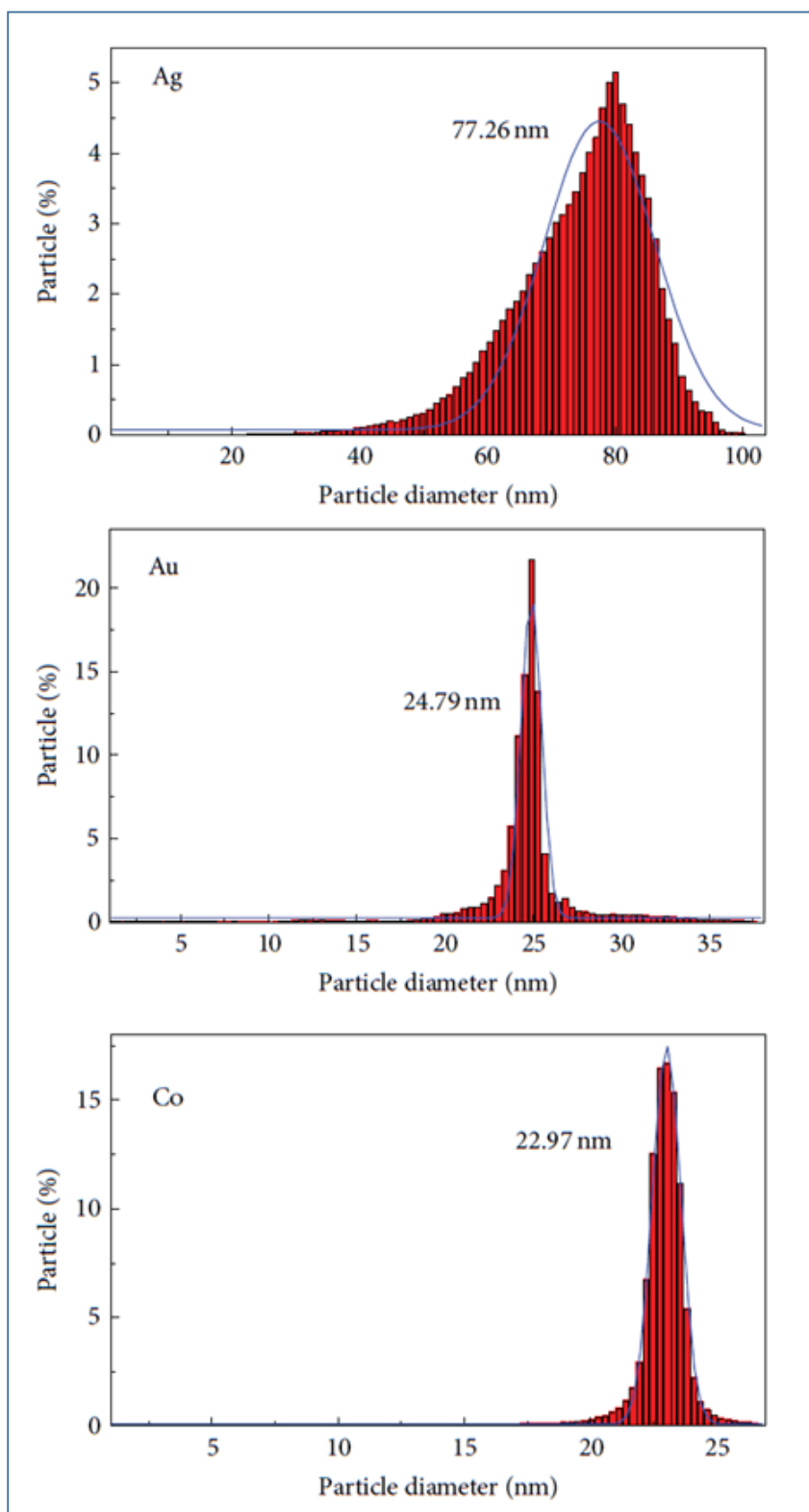
Figure 72: Histograms of particle dimensions distribution for each nanoparticle on HOPG surfaces obtained processing the AFM images by Nanoscope software (Bruker).

4.2.2.3. Analysis of nanocomposite optical properties

Even in this case, the measurements of the optical properties were acquired with the same equipment and the same parameters of the previous measures.

Optical absorption measurements in Figure 74 indicated a decrease of absorption of about 10% in all visible regions for all samples, indicating the progressive metallization of sample caused by the uniform coverage of nanoparticles on surfaces.

4.2.2.4. PL measurements

Photoluminescence measurements in Figure 73 indicate the origin of a strong visible luminescence for all composites with a great effectiveness for samples obtained with gold and silver. All the PL spectra present two main bands centered at about 560 and 620 nm (2.2 and 1.99 eV) and a loss intense band at 670 nm (1.84 eV). These structures indicate that the interaction between carbon surface and metal nanoparticles causes changes in graphite electronic band opening locally a band gap (caused by the defect introduced by nanoparticles in graphite structure) and favoring the visible transitions absent in pure graphite, as already observed in our previous work for carbon nanotube [6].
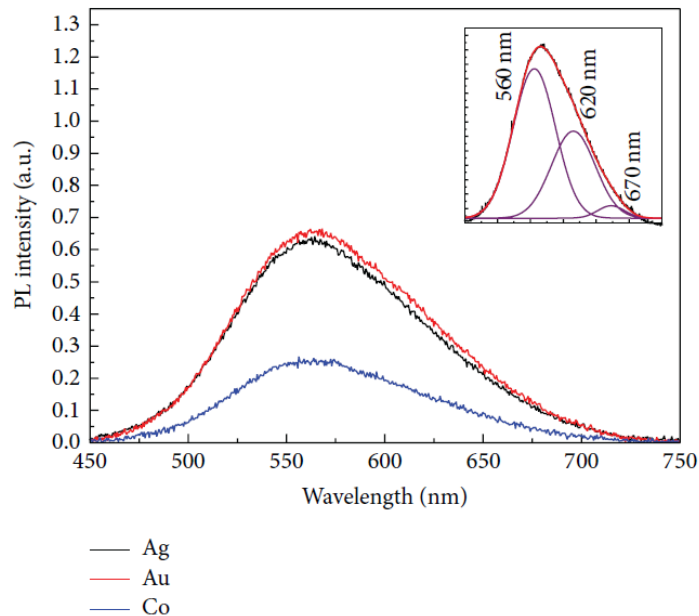

Figure 73: PL spectra for nanoparticle/HOPG composites. Inset: Gaussian spectrum deconvolution.
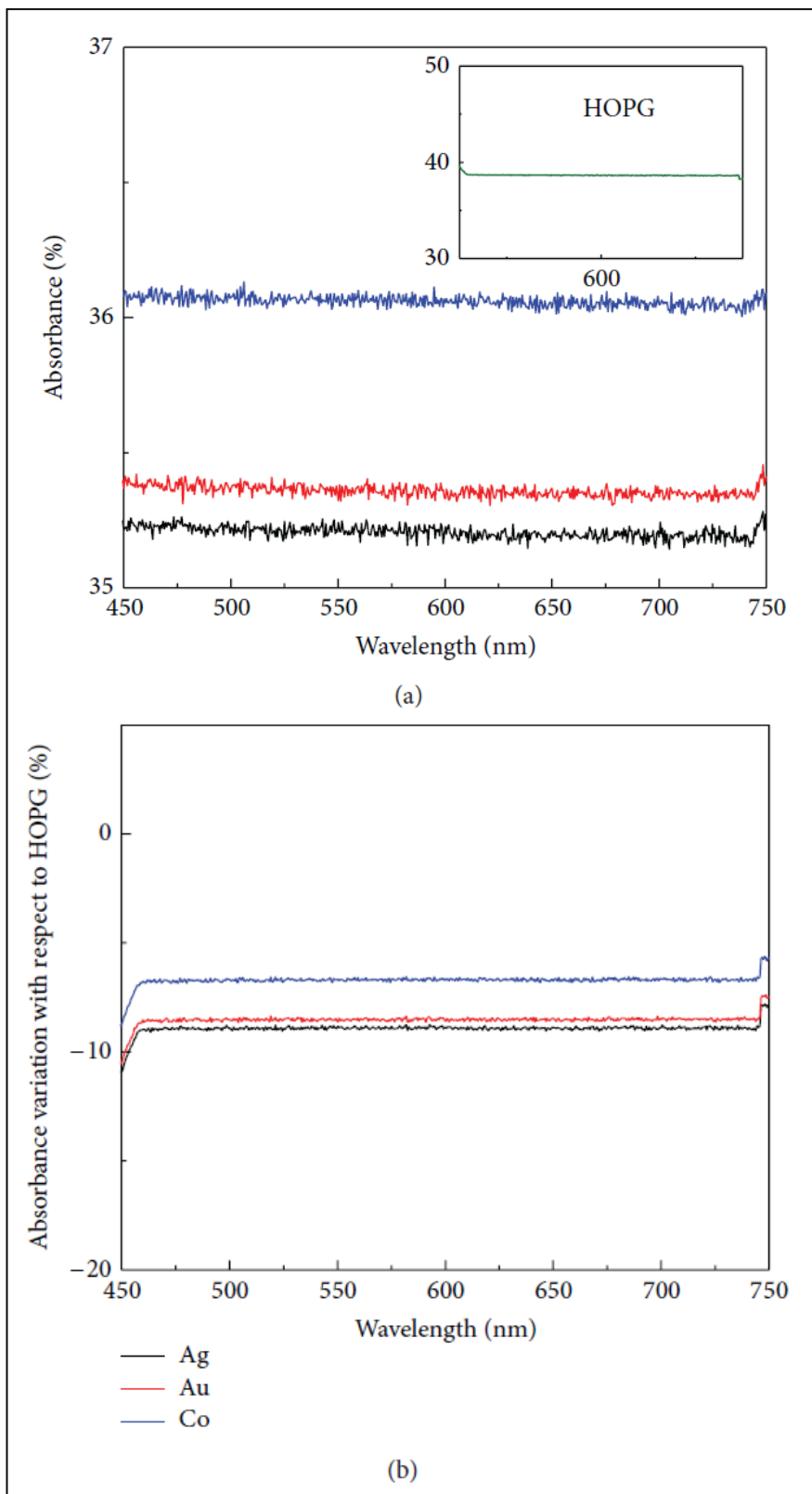
Figure 74: Optical absorption in visible region for nanoparticle/HOPG composites (a) and HOPG (inset in (a)). Variation of optical absorption with respect to pure HOPG (b).

4.2.2.5. Chemical analysis: XPS analysis on nanocomposites

For all samples XPS spectra indicate the only presence of carbon, oxygen, and NP on sample surface (Figure 75), confirming the cleanness of surface and the absence of chemical impurities incorporated in growth process.

The XPS main position of all elements on sample surfaces (summarized in Table 16 for only HOPG) indicates the absence of chemical bonds between carbon nanotubes and metals specifying the van deer Waals nature of bonding between particle and carbon and the physisorption character of particle absorption on sheet surface. The C1s line exhibits two lines at about 284 eV (C main line indicating C–C bonding) and 287 eV (indicating the presence of C–O bonds) [36].

The O1s line is, everywhere, symmetric and centered at about 531 eV confirming the presence of C-O bonding on surfaces [36]. All the metals exhibit the main atomic lines [36] without chemical shifts related to formation of chemical bonds between metal and C but indicating the presence of metal oxide formation. In particular, the position of main metallic XPS line indicates the formation of Ag–O and Co–O chemical bonds (suggesting the presence of both AgO and Ag_2O_3 oxides for silver and CoO for cobalt).
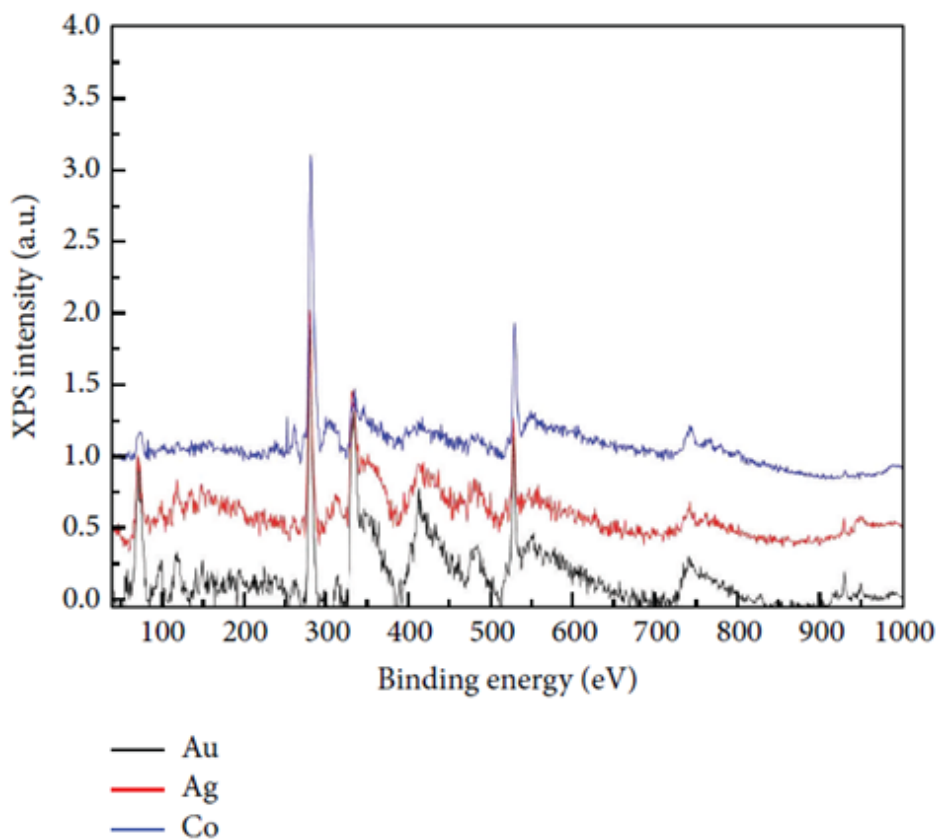
Figure 75: XPS spectra for nanoparticle/HOPG composites

131

Table 16: Element's amount on sample surface and XPS main line position evaluated from XPS data.

	Element's amount (%)		XPS main line position (eV)
Ag/HOPG			
Carbon	91.87	C 1s	284.5/287.2
Oxygen	7.26	O 1s	531.5
Silver	0.87	Ag 3d 3/2	374.3
Au/HOPG			
Carbon	87.52	C 1s	284.2/286.7
Oxygen	11.80	O 1s	530.9
Golden	0.67	Au 4f 7/2	83.62
Co/HOPG			
Carbon	91.4	C 1s	284.3/286.9
Oxygen	6.22	O 1s	531.2
Cobalt	2.34	Co 2p	778.1

4.2.3. <u>Innovative methods for protection and conservation of Cultural Heritage Assets: Deposition of Transparent, Hydrophobic TiO$_2$ Film on artifacts</u>

In recent decades, several scientific efforts have been made to fabricate superhydrophobic surfaces by using numerous techniques and methods, for example, plasma treatment [56], photolithography and sol-gel. Water repellent coatings can be important in many applications including, for example, the prevention of icing in cold weather, the promotion of self-cleaning process induced by rainwater on outdoor surfaces, the prevention of clotting in artificial blood vessels, the decrease of corona activity developed in conductors of transmission lines under rainy conditions, the production of waterproof and stain resistant textiles, and the reduction of friction in water [56]. One of the applications of the superhydrophobic coatings is their use as surface protective barriers for the preservations and conservation of ceramic and stone monuments. The most important degradation factor of outdoor, immovable cultural heritage is the rainwater, which can causes stone deterioration through cycles of freezing and thawing inside the pores of the stones or by intraporous crystallization of the salts transferred by the water [56]. For this reason, the application of hydrophobic coatings has been suggested for the surface protection of outdoor cultural heritage assets [56]. Moreover, several monuments are collocated in marine sites and cannot be removed from seabed, in these conditions the corrosion caused by marine water and microorganism can causes serious problems to conservation. Recently Manoudis et al. [61] described a simple method that can be used to impart superhydrophobicity to different stones surfaces (used in restoration of the castle of Prague). This method is based on the dispersion of nanoparticle in a polymeric solution that can be sprayed on the substrate. The resulting composite polymer-nanoparticle film exhibits superhydrophobic properties. However, this method cannot be applied in marine archeological sites (in underwater conditions the spray process is impossible and the dispersed particles can create environmental pollution). Moreover, in marine archeological sites the coverage of ceramic and stone must have an antibacterial action to inhibit the deterioration caused by the attack of marine microorganisms.

In this optics, a surface coverage by TiO$_2$ substrate, with its phocatalytic oxidation properties [56], can solve both the problems: idrophobicity and antibacterial activity.

Here we describe two simple methods to obtain TiO$_2$ coverage applicable in air and in marine water conditions. The obtained coverages are transparent (so it do not modify the artistic properties of monument) and hydrophobic, do not damage the ceramic surface and are easily removable by a simple cleaning process of laser ablation [33].

All the experiments were conducted on several ceramic fragments obtained from a "Carosello" [62], a structural hollow element made of clay, placed in arches, in domes or even and in the walls of buildings such as churches and houses, with the function lighten the structures (the specific "Carosello" used in these experiments come from a site in Calabria: the Sanctuary of "Madonna del Buonconsiglio" in San Giacomo di Cerzeto, Cosenza, Italy dated back to 1844 ± 11). The fragments have dimensions of about 1 cm × 2 cm and a thickness of about 2 cm.

We implement two different TiO_2 coverage process. One, applicable to little fragments of ceramic artifacts, contemplates a titanium evaporation in ultra high vacuum (UHV) chamber, while the second, applicable either in laboratory or in marine water, is a process of deposition of TiO_2 layer, previously evaporated on a salt, on ceramic surface.

4.2.3.1. TiO₂ evaporation in ultra-high vacuum (UHV)

The direct evaporation process was conducted in an ultra-high vacuum chamber with a base pressure of 1×10^{-9} mbarr. Ti was evaporated, in a controlled oxygen atmosphere (the partial pressure of oxygen in UHV chamber is fixed at 5×10^{-6} mbar), by heating an outgassed Mo boat filled with Ti crystal through a current of 60 A. The evaporation time ranged from 1 h to 7 h. The Titanium and oxygen atoms react on ceramic surfaces forming a TiO₂ layer (the formation of dioxide was confirmed by XPS data) with a thickness that increases with exposure time. Figure 76 shows samples obtained with exposure times of 1, 2, 3 and 4 hours, the sample coloration is unchanged after 1 h of exposure while becomes darker with time evaporation, clearly indicating the formation of TiO₂ layers with a thickness greater than 30 mm (the dioxide coloration is strictly related to layer thickness and only for dimensions greater than 30 microns the layer is colored and visible to the naked eye).
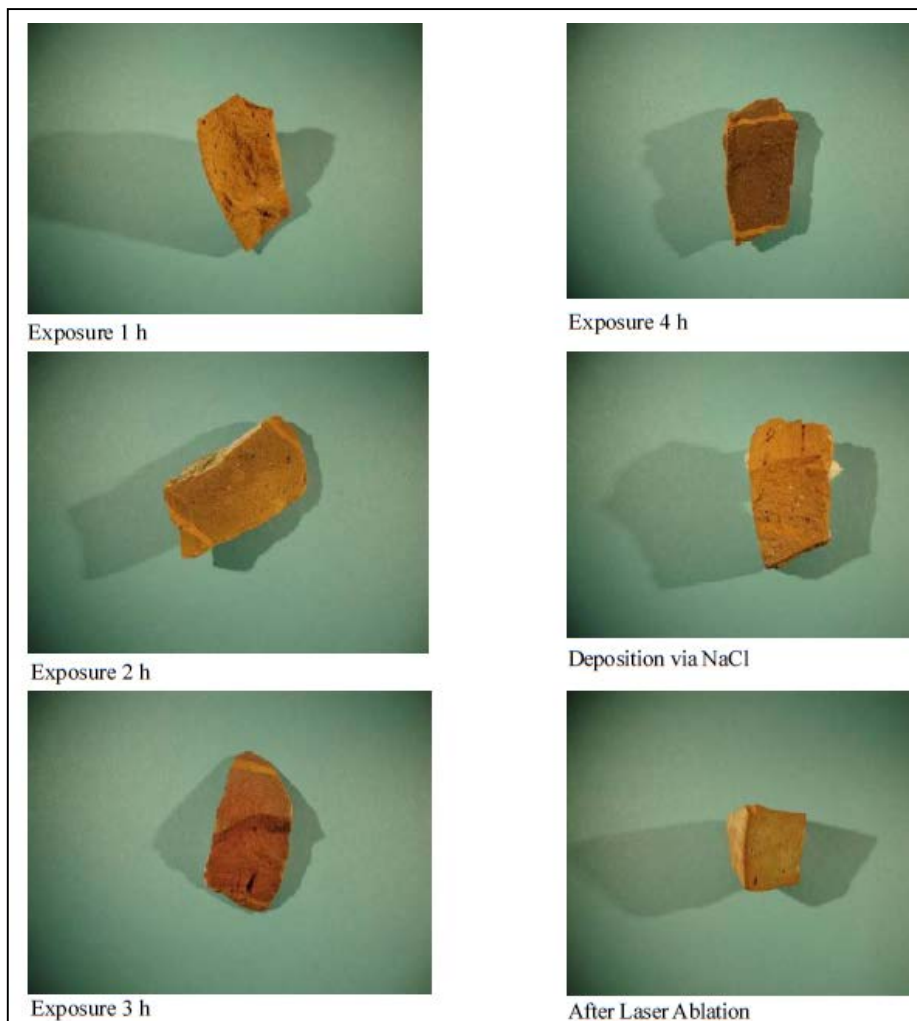

Figure 76: Images of "Carosello" fragments after Ti evaporation, after TiO₂ evaporation via NaCl and after laser ablation.

4.2.3.2. Deposition of TiO$_2$ layer in laboratory and in marine water

The deposition process includes two phases: a direct evaporation on a water-soluble salt surface (NaCl as example) using the process in UHV previous described and then the deposition of TiO$_2$ layer on ceramic surface on archaeological site (air or marine water). The salt was deposed on Aluminum foil and then inserted in UHV chamber where an evaporation process of 1 h deposes a TiO$_2$ transparent layer. Following the TiO$_2$ layer is covered by a silicon adhesive layer (to favourite the ceramic adhesion) and then sealed by aluminum foil to the application on ceramic. The salt surface and the aluminium foil were eliminated after deposition simply dissolving the salt with water. In this work we use as soluble salt the NaCl and the Na$_2$B$_4$O$_7\cdot$10H$_2$O obtaining the same results.

This process consent to prepare TiO$_2$ layer with desired dimensions in a laboratory and the application on ceramic surface directly in situ. Figure 76 shows the ceramic covered by TiO$_2$ deposed via NaCl salt; the dioxide layer is transparent and not modifies the sample coloration.

4.2.3.3. XPS measurements

XPS data in Figure 77 indicated that both process (direct evaporation and deposition) induce the only presence of Titanium and oxygen on ceramic sample without alter the sample composition or introducing impurities (Mo from evaporator boat, Al, Na or Cl from salt and deposition support foil). In particular in both process the Ti 2p lines are centered at 458.5 eV clearly indicated the only presence of TiO$_2$ structures on surface (without presence of isolated Ti atoms) [36].
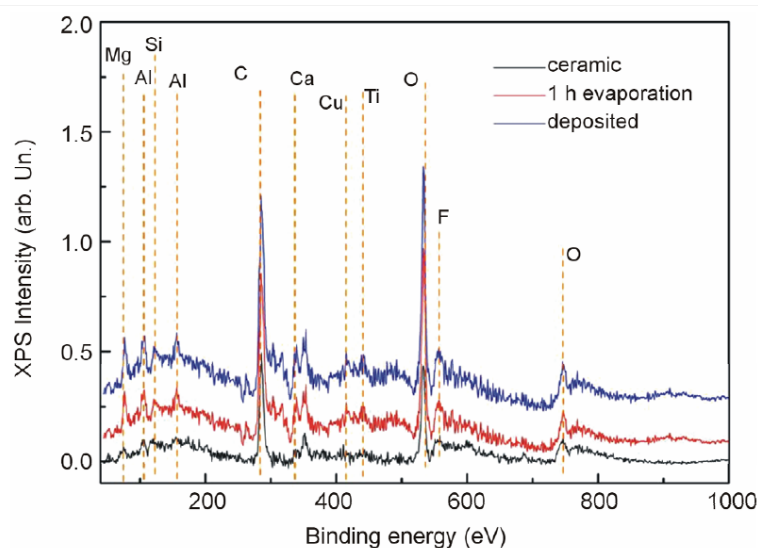

Figure 77: XPS survey spectra for samples treated with different deposition process.

4.2.3.4.   XRF measurements

XRF data in Figure 78(A) indicated that the amount of TiO_2 increases with evaporation times indicating the formation of layer with thickness gradually larger. Data in Figure 78(B) indicates, moreover, the composition of deposed layer of TiO_2 on salt (curve A for NaCl and B for Na2B4O7), it is clear that only TiO_2 is present on salt surface without any presence of impurities.

Curve c and d in Figure 78(B) indicates the surface composition after LA cleaning process (15' curve c and 30' curve d) it is clear that the Ti present on surface is completely removed and the sample spectrum is identical at this of pure ceramic (curve e).
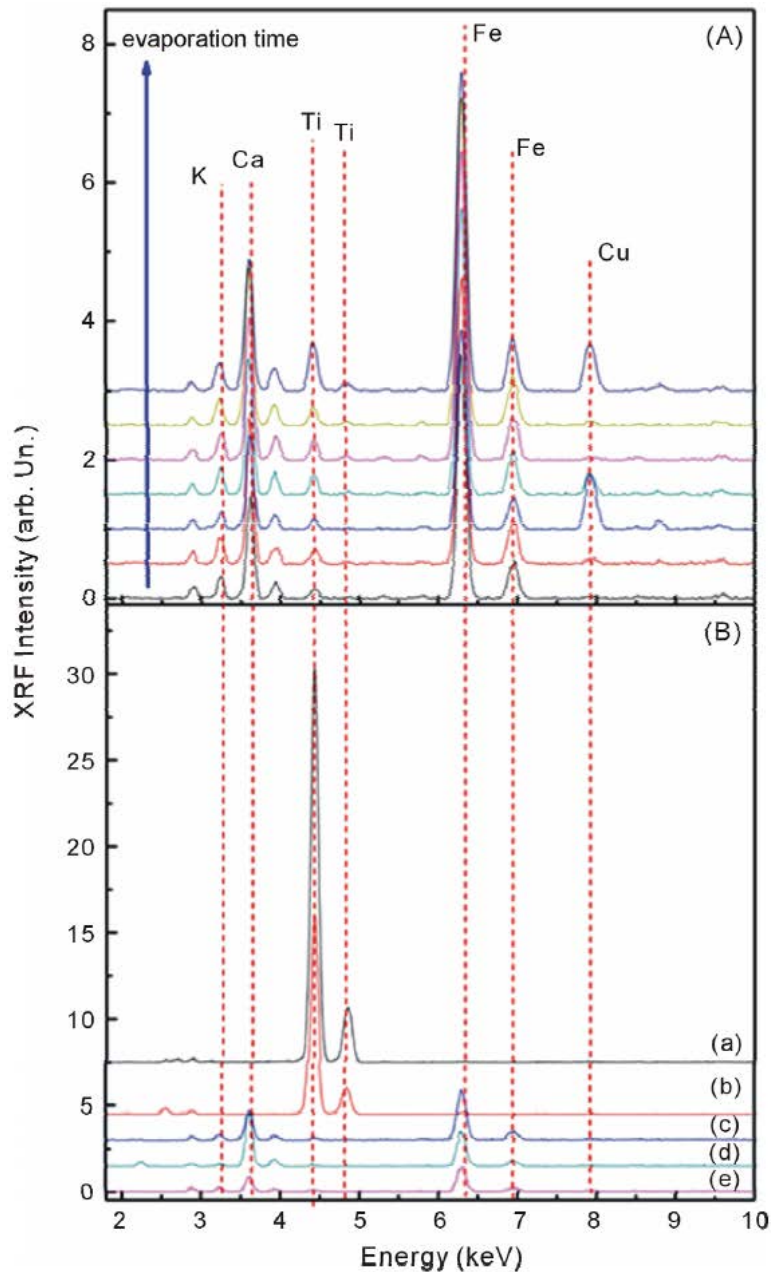

Figure 78: XRF spectra for sample s treated with different deposition process

4.2.3.5.   Contact angle measurements

The static water contact angle was analyzed to qualitatively assess the effectiveness of the surface coverage process and their influence on surface wetting. The sessile drop technique was employed. Indeed, the simple observation of a small liquid drop on a solid substrate provides useful information concerning the liquid-solid interaction and the hydrophobicity. The obtained results for both processes are summarized in Figure 79.

The ceramic surface is completely hydrophilic and the water drop is completely adsorbed. These properties of ceramic is the origin of surface degradation in marine water or after exposure to atmospheric wet. Therefore, the coverage with hydrophobic layer ensure the conservation of artifacts. However, the coverage must be transparent to not change the artistic and historic value of artifacts. For this we realize TiO_2 coverage with different thickness (and different coloration) verifying the hydrophobicity for each obtained layer. Figure 79 shows that the contact angle, and then the hydrophobicity, increases with evaporation time indicating for all samples an angle greater than 90° (hydrophobicity limit). In particular, we obtain a contact angle of about 110° for transparent layer obtained by 1 h evaporation and an angle of 96° for transparent layer deposed via NaCl.

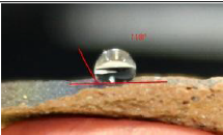These clearly indicate that in both process it is possible to obtain hydrophobic and transparent coverages.
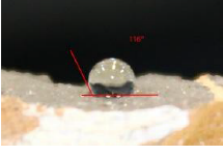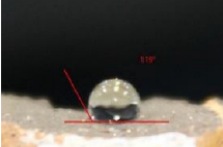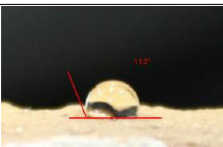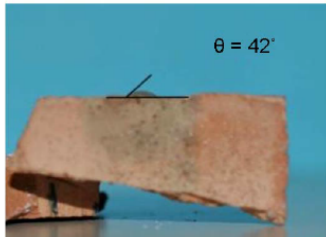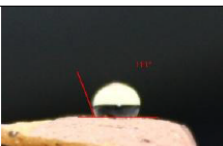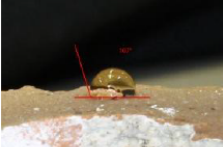
TiO₂ directly evaporated on ceramic (evaporation times (h))	Contact angle Θ (°)	TiO₂ deposited with NaCl salt on ceramic	Contact angle Θ (°)
(7 h)	118	θ = 96° After TiO₂ deposition	96
(6 h)	116		
(5 h)	119		
(4 h)	112	θ = 42° After 15' LA	42
(3 h)	111		
(2 h)	107		
(1 h)	110	After 30' LA	0

Figure 79: Contact angle after all treatments

139

4.2.3.6.   LA cleaning

After characterization all the samples was subjected to a Laser Ablation (LA) cleaning process to verify the reversibility of dioxide coverage and the possibility of future restoration on covered artifacts. The laser ablation procedure was performed irradiating for several minutes (15' or 30') each sample, immersed in an acetone solution, by the output of the first harmonic (1064 nm) of a Quanta-Giant series 710 Nd:YAG laser operating at 10 Hz. The spot size of the laser beam on the surface of Carosello is about of (7 - 8) mm and the power of laser is fixed at 500 mJ/pulse. The immersion in acetone is necessary to prevent the oxidation and carbonization of surface induced by LA in air [45]. Figure 76 shows the images of ablated artifacts, it is clear that the TiO_2 layer is completely removed as also confirmed by the results of XPS, XRF and contact angle measurements.

LA process remove the TiO_2 layer and the surface goes back to being hydrophilic. The contact angle, in fact, decreases to 40° after 15' of LA and until get to 0 after 30' of ablation. All these results was also confirmed by XRF and XPS analysis.

Both process are, so, able to cover the ceramic surface giving to ceramic an hydrophobic characteristic which can protect the artifact from corrosion caused by marine water or atmospheric wet. The obtained substrate are moreover completely transparent and can be removed simply by laser ablation process without change the ceramic properties.

5.   Conclusions

The research activity that conducted in this Ph. D. thesis have been solved problems related to LA cleaning and recovery of by-products generated from LA. We improved the method of LA cleaning on findings of a different nature.

Furthermore, using different diagnostic techniques, I answered to the questions raised by archaeologists or by *Italian Superintendence of Cultural Heritage*. I also demonstrated through practical examples on treated finds, how it is necessary an interdisciplinary approach between the different scientific disciplines in diagnostics of Cultural Heritage.

The following are the achievements for each of works discussed on different materials (such as alloys, metals and artificial stone) and the use of particulate matter that is generated by LA.

Concerning the study of materials, and in particular the experiments on silver, we studied the effect of laser ablation, in different medium, on Ag surface:

- The Ag samples were previous treated with HCl 37% solutions to simulate the formation of AgCl patina on marine archaeological silver artifacts. Cleanness procedure with laser ablation removes the chlorine formation but is enabling to remove constitutional impurities as C and O. In oxygen reach conditions (air and water); LA induces the absorption of ambient oxygen and the formation of a thin layer of AgO that modify the optical reflectance of sample. The shape of reflected signal is unchanged respect to the pure Ag sample but the intensity is more or less indicating a progressive tarnishing of surface during LA ablation, typical of oxide formation. The tarnishing is visible also on samples ablated without HCl treatment indicating that the problems not can be linked to the presence of AgCl residuals. Moreover, ablation of HCl treated and non-treated samples in oxygen absence (UHV conditions) not lead to formation of white patina while remove completely the chloride residuals (as indicated by XPS results). The ablation in vacuum condition is, so, the most indicated for silver artifacts because it leads to a complete cleanness of surface without changes the optical properties of silver.

Regarding the study of alloys, we analysed various commercial bronzes, to obtain information about the effect of LA cleaning; also, we investigated very famous archaeological bronzes, like the Riace bronzes, the charging bull of Sybaris, different helmets of the archaeological museum of Vibo Valentia and three fragments from the archaeological site of Quintilii's Villa.

In the experiments on commercial bronze, we have presented a comparison between the results of laser ablation cleanness process on bronze in two different medium: air and marine water.

- We obtain the bronze disease on commercial samples treating the samples with HCl 37%. XPS results on treated samples show the formation of a patina of $CuCl_2$ while optical images indicating that the thickness of patina is about 300 μm. Laser ablation process for 2 h in both marine water and air reduces the patina at few microns. The process is most effective in marine water. Cleanness in air, in fact, leads to adsorption of air oxygen and carbon corresponding to a progressive "carbonization" of sample. The greater cleanliness obtained in marine water opens the possibility to clean the bronzes directly in marine archeological sites without being moved, which may be damaged.

Instead, we can remark that the used analytical techniques are very effective for a qualitative and quantitative identification of the alloy composition and alteration products of fragments from Quintilii's Villa archaeological site.

- In fact, the investigation by SEM microscopy and AES and EDX spectroscopies allows us to identify the elemental composition of incrusted areas of "as received" samples revealing elements such as Cu, Sn, Si, Al, Ca, Fe, Mg, and P. The metal foil covering the samples (identifiable through the SE images and BSE) is formed by gold. Furthermore, from SE and BSE sample images (treated with H_2SO_4) we have obtained the thickness of the gold foil, which has an average thickness of 300 nm. The artefacts appear to be composed of different layers. A metal sheet that covers the alloy, consisting mostly of Au and a low percentage of Ag, forms a first zone. Alloy and its alteration products (chlorides, sulphides, and sulphates) compose an area below the gold sheet. Cu mainly forms an intermediate zone, and finally an inner area is composed of Cu, Cl, and S, with the presence of some contaminants such as Fe, Ca, and Si. Molecular spectroscopy FT-IR and Raman identified several alteration products from the study of patina mineral phases. In particular FT-IR spectroscopy indicates that the main surface alteration is the malachite $[Cu_2(CO_3)(OH)_2]$ while Raman spectroscopy reveals in addition to malachite the existence of connellite $[Cu_{19}Cl_4(SO_4)(OH)_{32} \cdot 3(H_2O)]$, which is one of the products classified as bronze diseases.

We know that the ceramic in archaeology is an important material for archaeologists due to its ability in providing information on many aspects of the past, including chronology by TL dating. Our study has demonstrated that LA cleaning does not affect this measure.
We considered two types of ceramics: a "Carosello" and Neolithic ceramics.

- The results on Carosello show the effectiveness of LA cleaning process on ceramic surface. The XPS measurements on the as received and ablated Carosello indicate that the LA is able to eliminate the surface impurities without change the chemical composition of samples (the main element on samples and their chemical bonds are unchanged). Moreover, the typical photoluminescence of quartzes (main components of ceramic artifacts) increases of about 96% after LA cleaning clearly indicating the removal of almost the entire surface patina. Finally, during the laser ablation process the temperature on entire artifact is less than 120 °C and this allows the possibility to use the bulk quartz to luminescence dating process.

- In the study of Neolithic ceramics, we also demonstrated that LA cleaning process do not affect the possibility to date a ceramic artifact after restoration process. We date a Neolithic ceramics before and after LA, obtaining results perfectly compatible. In fact, the samples were dated at 3300 B.C. when the sample for TL is taken before LA and at 3100 B.C. after LA; the difference of 200 years is below the limits of experimental errors. Moreover, we monitoring during all laser ablation cleaning process the sample temperature in the cavity for TL sample taking. The results show that temperature increases in the first minutes of irradiation reaching a saturation value of about 100°C while the metastable traps are empties only at temperature greater than 270°C.

Then, we have conducted a study on particulate generated by LA cleaning for application in the consolidation of the ceramic itself and high tech (photovoltaic and optoelectronic applications).

- We presented a study of growth of TiO_2 and SiO_2 nanoparticles for application to restoration and consolidation in archaeological artifacts, in a manner to explore the possibility of using as consolidating materials NPs without introducing chemical, physical or esthetical changes in artifacts. We grow by LASiS NPs with dimensions of about 10 and 15 nm, for SiO_2 and TiO_2 respectively, and spry-dried the colloidal solution on ceramic artifact surface. Chemical analysis show the physisorption nature of NP adsorption without formation of chemical bonds between NP and constitutive elements of ceramics or introduction of external impurities. Morphological analysis, conducted by SEM microscopy, shows the formation, for deposition of 50 ml of colloidal solution, of a thin layer of NPs on artifacts surface. This layer is perfectly transparent, uniform, and hydrophobic. In the other hands, XPS depth profile study indicate that NPs penetrate in the pore of artifacts consolidating the materials. The introduction of NPs is, then, a good strategy for restoration, consolidation and conservation.

Regarding the recovery of NP for realization of nanocomposites for photovoltaic applications, we performed two works; the first describes the implementation of nanocomposites formed by carbon nanotube (CNT) / metal nanoparticles (MNPs) and the second formed by metal nanoparticles (MNPs) / graphite.

- In the first work, we show the possibility to obtain new nanocomposites by carbon nanotubes and transition metal nanoparticles. The nanoparticles, obtained by laser ablation, are been physisorbed on multiwalled carbon nano-tubes sheet in acetone solution. The AFM and SEM images of nanocomposites show a network of carbon nanotubes where each tube is completely covered by nanoparticle with dimensions of about 40 - 50 nm, while bigger particle (about 100 nm) is randomly dispersed on sheet surface. Noble metals show a different behaviour, the nanoparticle is aggregated in sphere with diameter of 100 nm dispersed on a sheet but the single tubes are not covered by nanoparticle indicating only a CNT doping.
  The obtained nanocomposites show very different electronical and optical properties respect to pure carbon nanotubes. They are hydrophobic while CNT are hydrophilic, exhibit a strong

visible photoluminescence that is completely quenched in carbon nanotubes and shows a decrease on surface roughness of about 50%. Besides, many efforts are necessary to understand the different behaviour of transition and noble metals.

- Instead, in the second work we present the results of a study of interaction between nanoparticle and carbon surfaces that extend and conclude our previous study of interaction of metal nanoparticle and carbon nanotubes [6]. The metal nanoparticles (gold, silver, and cobalt) were obtained by laser ablation in acetone solution and their dimensions were controlled before the inclusion on carbon surfaces with Kelly scattering theory and AFM characterization as described in [6]. The experiment was conducted on both oriented and amorphous graphite layers. The results confirm what has been achieved between carbon and metals. Furthermore, the interfacial interaction between particles and carbon layers (due to only van deer Waals interactions) causes local defects in graphite structure indicated by the presence of a strong photoluminescence signal for all composites. Moreover, we note a decrease of about 10% in visible optical absorption indicating the progressive metallization of carbon surface.

In addition, we have studied new methods of protection and conservation of Cultural Heritage Assets through deposition of transparent, hydrophobic TiO_2 film on artifacts.

We have presented a method to prepare carbon nanotubes/titanium dioxide ($CNTs/TiO_2$) nanocomposites with a simple metal vaporization technique. We obtain a composite with a uniform layer of $Ti/TiO2$ on the CNT structure and we can evaluate exactly the ratio between Ti and its dioxide in the film by X-ray Photoemission Spectroscopy (XPS). The TiO2 layer do not change the structures of carbon nanotubes, as visible from TEM images, but it is perfectly super imposed to CNT buckypaper. The crystallinity of TiO2 substrate, obtained by FTIR measurements, clearly indicate the formation of anatase structure.

Finally, the growth mechanism of evaporation leads to formation of TiO2 molecules by bonds between evaporated Ti atoms and oxygen on surface, preventing the formation of oxygen vacancies on TiO2 bulk and quenching the luminescence emission typical of these structures. The prevention of luminescence emission in TiO_2 films is very important because it is cause of electron loss in photo electrochemical cells. Further effort will be dedicated in a subsequent work to the possibility of controlling this ratio between the composites in order to obtain films of different composition and finally a uniform TiO_2 film on the nanostructure.

Moreover, it will be interesting to investigate the electrical and optical properties of the so prepared CNT/TiO_2 samples especially in relation to the TiO_2 film uniformity.

Publications on Peer Reviewed International Journals

1. <u>F. Stranges</u> , M. La Russa, A. Oliva and G. Galli,
   ANALYSIS OF THE QUINTILII'S VILLA BRONZES BY SPECTROSCOPY TECHNIQUES
   Journal of Archaeology Volume 2014, Article ID 312981, 7 pages

2. M. Barberio, V. Pingitore, P. Barone, M. Davoli, <u>F. Stranges</u>, F. Xu, A. Bonanno,
   SYNTHESIS OF CARBON NANOTUBE/TiO_2 COMPOSITES BY TITANIUM EVAPORATION IN
   ULTRA HIGH VACUUM AMBIENT
   Microelectronics Engineering 108, 213 (2013)

3. <u>F. Stranges</u>, M. Barberio, P. Barone, V. Pingitore, F. Xu, A. Bonanno,
   LASER ABLATION OF SILVER ARTIFACTS IN VACUUM: SOLUTION TO SILVER TARNISHING
   PROBLEM,
   Journal of Earth Science and Engineering, 2, 693 (2013)

4. M. Barberio, <u>F. Stranges</u>, D. Renzelli, P. Barone, F. Xu, A. Bonanno,
   EFFECT OF LASER ABLATION CLEANING PROCESS ON CERAMIC ARTIFACTS
   Journal of Physical Science and Application 3 (4) (2013) 224-228

5. M. Barberio, P. Barone, <u>F. Stranges</u>, R. A. Romano, F. Xu, A. Bonanno,
   ADSORPTION OF MOLECULAR GASES ON SILVER/CARBON NANOTUBE COMPOSITES AT LOW
   TEMPERATURES AND LOW PRESSURES,
   Journal of Chemistry, 2014 Article ID 816193 (2014)

6. <u>F. Stranges</u>, M. Barberio, P. Barone, A. Abenante, A. Leuzzi, P. Sapia, F. Xu, and A. Bonanno,
   DEPOSITION OF TRANSPARENT, HYDROPHOBIC TiO_2 FILM FOR THE PROTECTION OF
   OUTDOOR AND MARINE CULTURAL HERITAGE ASSETS,
   Journal of Cultural Heritage Vol.1 No.2, October 2013
   http://dx.doi.org/10.4236/ad.2013.12002

7. M. Barberio, P. Barone, <u>F. Stranges</u>, A. Romano, F. Xu, A. Bonanno,
   CARBON NANOTUBES/ METAL NANOPARTICLE BASED NANOCOMPOSITES: IMPROVEMENTS
   IN VISIBLE PHOTOLUMINESCENCE EMISSION AND HYDROPHOBICITY
   Optics and Photonics Journal Vol.3 No.6A (2013), Article ID:38552, 7 pages
   DOI:10.4236/opj.2013.36A007

8. P. Barone, M. Barberio, F. Stranges, D. Renzelli, A. Bonanno and F. Xu,
STUDY OF BAND GAP OF SILVER NANOPARTICLES – TITANIUM DIOXIDE NANOCOMPOSITES,
Journal of Vacuum Science and Technology Volume 2014 (2014), Article ID 589707, 6 pages
http://dx.doi.org/10.1155/2014/589707

9. P. Barone, F. Stranges, M. Barberio, F. Xu, A. Bonanno,
APPLICATION OF LASER ABLATION TO CLEANING PROCESS OF THE CORROSION CHLORIDE
PATINA FORMED ON BRONZE SURFACES IN AIR AND MARINE WATER,
Physical Science and Application 3, 135-140 (2013)

10. Pasquale Barone, Marianna Barberio, Fabio Stranges, and Fang Xu,
STUDY OF COATING GEOMETRIES AND PHOTOLUMINESCENCE PROPERTIES OF METAL
NANOPARTICLES/GRAPHITE COMPOSITES,
Journal of Chemistry, 2014 (2014), Article ID 204028

11. D. Renzelli, S. Veltri, F. Stranges, P. Barone, M. Barberio, F. Xu, A. Bonanno,
LASER ABLATION CLEANING EFFECTS ON THERMOLUMINESCENCE DATING TECHNIQUE,
Archeological Discovery 2, 58 (2014)

12. M. Barberio, F. Stranges, F. Xu,
COATING GEOMETRY OF Ag, Ti, Co, Ni, AND Al NANOPARTICLES ON CARBON NANOTUBES,
Applied Surface Science,
DOI: 10.1016/j.apsusc.2014.09.045 (in press)

13. M. Barberio, S. Veltri, A. Imbrogno, F. Stranges, F. Xu and P.Antici,
TiO_2 AND SiO_2 NANOPARTICLES FILM FOR CULTURAL HERITAGE: CONSERVATION AND
CONSOLIDATION OF CERAMIC ARTIFACTS,
Surface and Coatings Technology (accepted)

14. M. Barberio, F. Stranges, A. Imbrogno and F. Xu, GROWTH OF CORE-SHELL QUANTUM
DOTS/TITANIUM DIOXIDE HYBRID FILMS AS PHOTOANODE FOR GRAETZEL CELLS,
Surface and Coatings Technology (accepted)

Contribution on International Conference

1) D. Renzelli, P. Barone, <u>F. Stranges</u>, V. Pingitore and A. Oliva, SAR AND MAAD TL DATING OF STRUCTURAL ELEMENTS FROM THREE SITE IN CALABRIA, SOUTH ITALY «2nd Luminescence in Archaeology International Symposium L.A.I.S. 2012 LISBON», 5th - 7th of September 2012 - GeoLuC, UCQR, Instituto Tecnologico e Nuclear, EN10, 2686-953 Sacavem, Portugal L.A.I.S. 2012, LISBON

2) P. Barone, <u>F. Stranges</u>, M. Barberio, D. Renzelli, A. Bonanno, F. Xu, Study of band gap of silver nanoparticles - titanium dioxide nanocomposites, Nanosmat 2013 (Granada 2013)

3) <u>F. Stranges</u>, P. Barone, M. Barberio, A. Romano, F. Xu, A. Bonanno, Surface Properties of Metal - Metal Oxide Nanoparticles /Carbon Nanotubes Composites, Nanosmat 2013 (Granada 2013)

4) M. Barberio, S. Veltri, <u>F. Stranges</u>, F. Xu, P. Antici, TiO_2 and SiO_2 nanoparticles film for cultural heritage: conservation and consolidation of ceramic and stone artifacts, Nanosmat 2014 (Dublin, September 2014)

References

[1] W. L. W. Z. W. Z. A.C. Tam, "Laser-cleaning techniques for removal of surface," *J. Appl. Phys.,* pp. 71 - 3515, 1992.

[2] A. J. C. I. C. D. M. M. O. I. Siano S., "Laser cleaning in conservation of stone, metal, and painted artifacts: State of the art and new insights on the use of the Nd:YAG lasers," *Appl. Phys. ,* p. A 106 419, 2012.

[3] F. S. M. B. a. A. B. Pasquale Barone, "Application of Laser Ablation to Cleaning Process of the Corrosion Chloride Patina Formed on Bronze Surfaces in Air and Marine Water," *Journal of Physical Science and Application,* vol. 3 (3), pp. 135-140, 2013.

[4] S. E. Black, Laser Ablation, Effects and applications, New York: Nova Science Publishers, Inc., 2011.

[5] P. B. F. S. D. R. F. X. a. A. B. Marianna Barberio, "Effect of Laser Ablation Cleaning Process on Ceramic Artifacts," *Journal of Physical Science and Application,* vol. 3, no. 4, pp. 224-228, 2013.

[6] P. B. F. S. A. R. F. X. A. B. M. Barberio, "Carbon Nanotubes/Metal Nanoparticle Based Nanocomposites: Improvements in Visible Photoluminescence Emission and Hydrophobicity," *Optics and Photonics Journal,* vol. 3, pp. 34-40, 2013.

[7] F. D. S. M. A. O. J. M. K. a. I. A. E. Fortunati, "Carbon Nanotubes and Silver Nanoparticles for Multifunctional Conductive Biopoly- mer Composites," *Carbon,* vol. Vol. 49, no. No 7, pp. 2370-2379, 2011.

[8] D. W. Luhs, "Diodelaser Pumped Nd : YAG Laser," *Didactic Counsellor MEOS GmbH 79427 Eschbach,* Jan. 1999/July 2003.

[9] R. Boyd, Nonlinear optics, San Diego: Academic Press, 1995.

[10] D. v. d. L. a. K. Sokolowski-Tinten, "Physical mechanisms of short pulse laser ablation," Institut fŸr Laser- und Plasmaphysik, UniversitŠt Essen, D-45117 Essen, Germany.

[11] A. V. R. V. T. T. a. B. L.-D. E. G. Gamaly, "Ablation of solids by femtosecond lasers: ablation mechanism and ablation thresholds for metals and dielectrics," *Phys. Rev. A,* 23 January 2001.

[12] A. V. R. V. T. T. a. B. L.-D. E. G. Gamaly, "Ablation of solids by femtosecond lasers: ablation mechanism and ablation thresholds for metals and dielectrics," *Phys. Rev. A,* 23 January 2001.

[13] V. A. a. M. Meneghetti, "Laser ablation synthesis in solution and size manipulation of noble," *Physical Chemistry Chemical Physics,* vol. 11, p. 3805–3821, 2009.

[14] R. K. A. Miotello, "Critical assessment of thermal models for laser sputtering at high fluences," *Appl. Phys. Lett.,* no. 67 3535, 1995.

[15] V. A. a. M. Meneghetti, "What controls the composition and the structure of nanomaterials generated by laser ablation in liquid solution?," *Physical Chemistry Chemical Physics,* Vols. 15, 2037, no. Issue 9, 07 March 2013.

[16] K. S.-T. D. von der Linde, "The physical mechanisms of short-pulse laser ablation," *Applied Surface Science,* no. 1–10, p. 154–155, 2000.

[17] L. J. L. a. M. M. P. Lorazo, *Phys. Rev. B:Condens. Matter Mater. Phys,* no. 134108, p. 73, 2006,.

[18] J. S. G. N. a. C. G. L. Kiss, *Nanotechnology,* vol. 10, no. 25, 1999.

[19] L. K. G. N. a. C. G. J. Soderlund, *Phys. Rev. Lett.,* vol. 80, no. 2386, 1998.

[20] K. I. Y. N. a. M. T. T. Tsuji, *J. Photochem. Photobiol,* vol. 145, p. 201–207, 2001.

[21] R. B. Y. H. A. C. S. B. Q. C. Z. D. a. D. B. C. Z. Yan, *J. Phys. Chem. C,* vol. 114, p. 3869–3873, 2010.

[22] A. V. K. a. M. Meunier, *J. Appl. Phys,* vol. 94, no. 7941–7943, 2003.

[23] J. K. Y. T. T. K. a. H. S. F. Mafune´, *J. Phys. Chem. B,* vol. 104, p. 9111–9117, 2000.

[24] D. C. N. D. F. a. F. V. Otto Muskens, "Optical response of a single noble metal nanoparticle," *JOURNAL OF OPTICS A: PURE AND APPLIED OPTICS,* p. S264–S272, January 2006.

[25] E. Meyer, "ATOMIC FORCE MICROSCOPY," *Progress in Surface Science,* vol. Vol. 41, pp. 3-49, 1992.

[26] P. E. West, Introduction to Atomic Force Microscope: Theory, Practice, and Applications, 2006.

[27] B. C. C. ©, "Bruker Dimension icon. Instruction Manual," 2008, 2009, 2010, 2011.

[28] F. COMPANY, User Manual FEI Quanta 200 FEG, 2006.

[29] C. Ronda, Luminescence: From theory to applications, Weinheim: Wiley - VCH, 2008.

[30] J. Andrade, "X Ray Photoelectron Spectroscopy (XPS). New York , NY," *Surface and Interfacial Aspect of Biomedical Polymers,* pp. 105-195, 1985.

[31] G. PK., Introduction to Photoelectron Spectroscopy, New York, NY: John Wiley and Sons, Inc., 1983.

[32] I. G. J. Vickerman, Surface Analysis – The Principal techniques 2nd edition, John Wiley & Sons, 2009.

[33] M. B. P. B. V. P. F. X. a. A. B. Fabio Stranges, "Laser Ablation of Silver Artifacts in Vacuum: Solution to Silver Tarnishing Problem," *Journal of Earth Science and Engineering,* vol. 2, pp. 697-703, 2012.

[34] R. S. S. Siano, "The gate of paradise: Physical optimization of the laser cleaning approach," *Studies in Conservation,* no. 46, pp. 269-281, (2001).

[35] J. A. I. C. D. C. M. M. I. O. e. a. S. Siano, "Laser cleaning in conservation of stone, metal, and painted artifacts: State of the art and new insights on the use of the Nd: YAG lasers," *Physics A,* no. 106, pp. 419-446, (2012).

[36] N. X. d. [Online]:, "http://srdata.nist.gov/xps/".

[37] A. C. Reardon, Metallurgy for the Non-Metallurgist, Second Edition, USA: ASM International, 2011.

[38] F. Stranges, "Caratterizzazione di bronzi provenienti dal sito archeologico di Villa dei Quintili.," *Tesi di Laurea Magistrale , Facoltà di S.M.F.N. Università della Calabria,* 2011.

[39] R. P. Luc Robbiola, "A global approach to the authentication of ancient bronzes based on the characterization of the alloy–patina–environment system," *Journal of Cultural Heritage,* no. 7, pp. 1-12, 2006.

[40] F. S. M. B. a. A. B. Pasquale Barone, "Application of Laser Ablation to Cleaning Process of the Corrosion Chloride Patina Formed on Bronze Surfaces in Air and Marine Water," *Journal of Physical Science and Application,* vol. 3, no. 3, pp. 135-140, 2013.

[41] M. L. R. A. O. a. G. G. Fabio Stranges, "Analysis of the Quintilii's Villa Bronzes by Spectroscopy Techniques," *Journal of Archaeology,* p. 7, 2014.

[42] P. W. Palmberg, "Handbook of Auger Electron Spectroscopy: A Reference Book of Standard Data for Identification and Interpretation of Auger Spectroscopy Data," *Phisical Electronics, Eden Praire,* Minn, USA, 1972.

[43] "ONLINE FTIR database spectra, INFRARED SPECTRA," *http://www.infrared-spectra.com/.*

[44] "(online) Database of Raman spectroscopy , X Ray diffraction and chemistry of minerals," *RRUFF (online) http://rruff.info/.*

[45] 2. P. B. F. S. D. R. F. X. a. A. B. Marianna Barberio1, "Effect of Laser Ablation Cleaning Process on Ceramic Artifacts," *Journal of Physical Science and Application,* vol. 3, no. 4, pp. 224-228, 2013 .

[46] D. R. P. B. V. P. A. O. C. Gattuso, "Sar and Maad Tl Dating of "Caroselli" from three sites in calabria, South Italy," *Mediterranean Archeology and Archeometry,* vol. 12, no. 43, 2012 .

[47] L. o.-l. d. base, "Luminescence on-line data base, http://www.csiro.au/," *http://www.csiro.au/.*

[48] S. V. F. S. P. B. M. B. F. X. A. B. Diana Renzelli, "Laser Ablation Cleaning Effects on Thermoluminescence Dating Technique," *Archaeological Discovery,* vol. 2, pp. 58-64, 2014.

[49] D. C. R. G. a. G. P. Piero Baglioni, "Colloid and Materials Science for the Conservation of Cultural Heritage: Cleaning, Consolidation, and Deacidification," *pubs.acs.org/Langmuir.*

[50] S. V. A. I. F. S. F. X. a. P. M. Barberio, "TiO_2 and SiO_2 nanoparticles film for cultural heritage: conservation and consolidation of ceramic artifacts," *Surface and Coatings Technology ,* vol. (accepted), 2014.

[51] A. M. M. F. L. R. L. M. C. U. F. D. L. M. B. G. M. C. S. A. Ruffolo, "Marine Antifouling for Underwater Archaeological Sites: TiO2 and Ag-Doped TiO2," *International Journal of Photoenergy http://dx.doi.org/10.1155/2013/251647,* p. 6, 2013.

[52] Palick handbook.

[53] HB extinction.

[54] D. R. C. F. L. W. F. G. J.M. Hill, "Properties of oxidized silicon as determined by angular-dependent X-ray photoelectron spectroscopy," *Chemical Physics Letters,* vol. 44, pp. 225-231, (1976).

[55] Free path Ti 2p in silicon.

[56] M. B. P. B. A. A. A. L. P. S. F. X. A. B. Fabio Stranges, "Deposition of Transparent, Hydrophobic TiO2 Film for the Protection of Outdoor and Marine Cultural Heritage Assets," *Archaeological Discovery Published Online October 2013 in SciRes http://dx.doi.org/10.4236/ad.2013.12002,* vol. 1, no. 2, pp. 32-36, 2013.

[57] X. Z. a. Y. X. Gan, "Nanocomposites for Photovoltaic Energy Conversion," *Intechopen,* no. 8, pp. 211-266, April 2011.

[58] E. C. L. L. Z. a. G. C. S. K. L. Kelly, "The Optical Properties of Metal Nanoparticles: The Influence of Size, Shape, and Dielectric Environment," *The Journal of Physical Chemistry B http://dx.doi.org/10.1021/jp026731y,* vol. 107, no. 3, pp. 668-677, 2003.

[59] M. B. F. S. a. F. X. Pasquale Barone, "Study of Coating Geometries and Photoluminescence Properties of Metal Nanoparticles/Graphite Composites," *Journal of Chemistry http://dx.doi.org/10.1155/2014/204028,* p. 6 pages, 2014.

[60] J. Z. Y. W. a. Z. Y. Y. He, "Coating geometries of metals on single-walled carbon nanotubes," *Applied Physics Letters Article ID 063108,* vol. 96, 2010.

[61] P. N. K. I. T. A. Z. I. K. B. &. P. C. Manoudis, "Superhydrophobic films for the protection of outdoor cultural heritage assets http://dx.doi.org/10.1007/s00339-009-5233-z," *Applied Phisics A,* vol. 97, pp. 351-360, 2009.

[62] D.-.. T. Y. O. M. N. Y. T. T. Tsuji, *Appl. Surf. Sci.,,* no. 5224, p. 254, 2008.